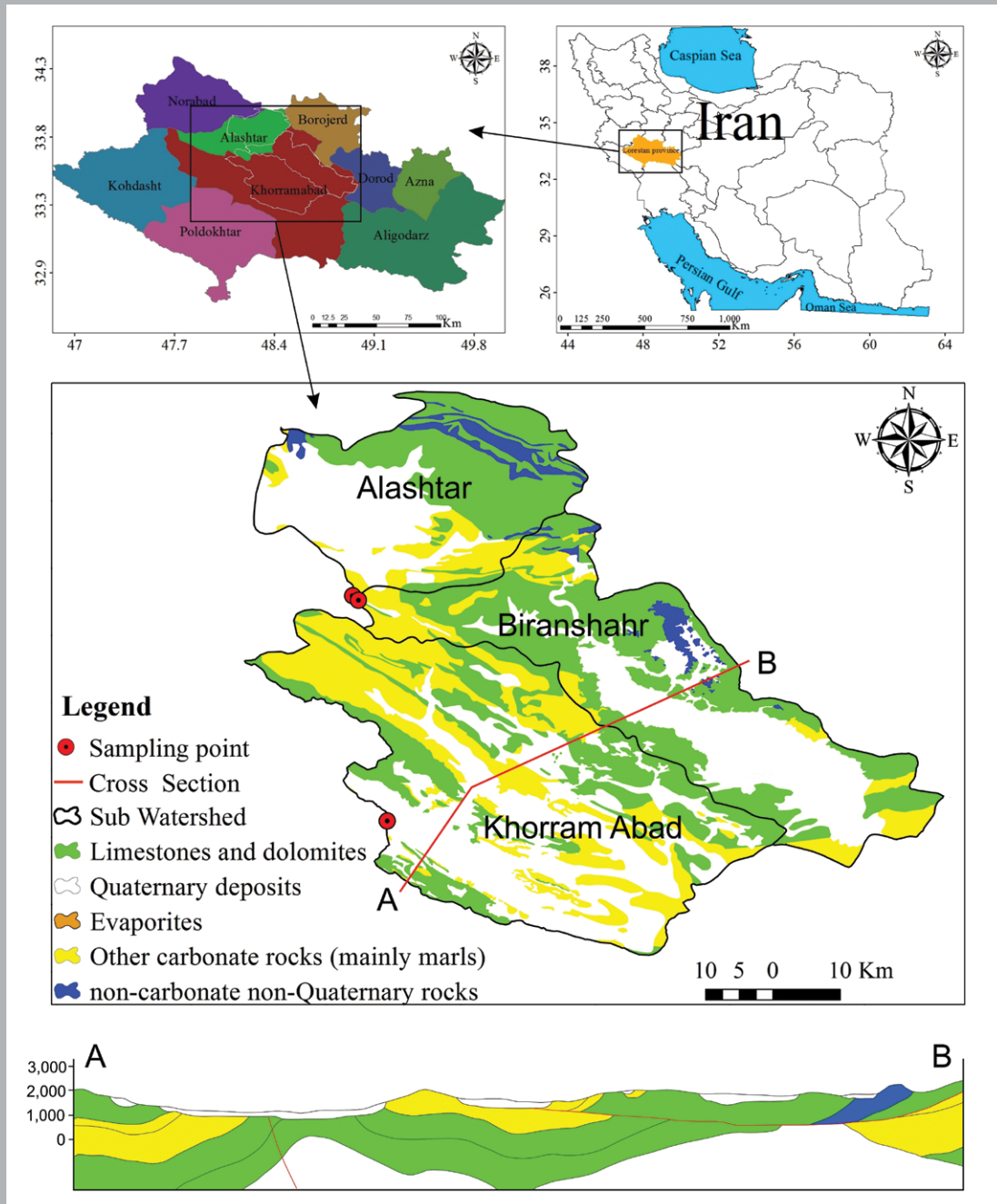


JOURNAL OF CAVE AND KARST STUDIES

September 2021
Volume 83, Number 3
ISSN 1090-6924
A Publication of the National
Speleological Society



DEDICATED TO THE ADVANCEMENT OF SCIENCE,
EDUCATION, EXPLORATION, AND CONSERVATION

**Published By
The National Speleological Society**

<http://caves.org/pub/journal>

Office

6001 Pulaski Pike NW
Huntsville, AL 35810 USA
Tel:256-852-1300
nss@caves.org

**Editor-in-Chief
Malcolm S. Field**

Washington, DC
703-347-8601
field.malcolm1@gmail.com

**Production Editor
Scott A. Engel**

Knoxville, TN
225-281-3914
saecaver@gmail.com

The *Journal of Cave and Karst Studies*, ISSN 1090-6924, CPM Number #40065056, is a multi-disciplinary, refereed journal published four times a year by the National Speleological Society. The *Journal* is available by open access on its website, or check the website for current print subscription rates. Back issues are available from the NSS office.

POSTMASTER: send address changes to the National Speleological Society Office listed above.

The *Journal of Cave and Karst Studies* is covered by the following ISI Thomson Services Science Citation Index Expanded, ISI Alerting Services, and Current Contents/Physical, Chemical, and Earth Sciences.

Copyright © 2021
by the National Speleological Society, Inc.

BOARD OF EDITORS

Anthropology

George Crothers
University of Kentucky
Lexington, KY
george.crothers@utk.edu

Conservation-Life Sciences

Julian J. Lewis & Salisa L. Lewis
Lewis & Associates, LLC.
Borden, IN
lewisbioconsult@aol.com

Earth Sciences

Benjamin Schwartz
Texas State University
San Marcos, TX
bs37@txstate.edu

Yongli Gao

University of Texas at San Antonio
yongli.gao@utsa.edu

Mario Parise

University Aldo Moro
Bari, Italy
mario.parise@uniba.it

Carol Wicks

Louisiana State University
Baton Rouge, LA
cwicks@lsu.edu

Exploration

Paul Burger

National Park Service
Eagle River, Alaska
paul_burger@nps.gov

Microbiology

Kathleen H. Lavoie

State University of New York
Plattsburgh, NY
lavoiekh@plattsburgh.edu

Paleontology

Greg McDonald

National Park Service
Fort Collins, CO
greg_mcdonald@nps.gov

Social Sciences

Joseph C. Douglas

Volunteer State Community College
Gallatin, TN
615-230-3241
joe.douglas@volstate.edu

Book Reviews

Arthur N. Palmer & Margaret V Palmer

State University of New York
Oneonta, NY
palmeran@oneonta.edu

Front cover: The presence of soluble rock in the Zagros region of Iran. See Sepahvand et al. in this issue.

SOLUTE TRANSPORT AND SOLUTIONAL DENUDATION RATE OF CARBONATE KARST IN THE SEMI-ARID ZAGROS REGION (SOUTHWESTERN IRAN)

Alireza Sepahvand¹, Mitja Prelovšek^{2,C}, Ali Akbar Nazari Samani³, Robert James Wasson⁴

Abstract

We conducted a one-year-long study of solute load measured three times per month in three neighboring subwatersheds (Alashtar, Khorram Abad, and Biranshahr) located in the Karkheh River basin in the Zagros region of southwestern Iran. Research was focused on the chemical composition of water (solute load), karst denudation rate, spatial and temporal variability, as well as comparison of solute load with suspended load. Results show that Ca-Mg-HCO₃ is the dominant water type that reflects the lithological characteristics of the catchment areas. Lack of seasonal fluctuation of solute load and absence of dilution during high water levels but evident seasonal course of discharge defines the highest solute flux during the annual maximum of discharge in spring months. The highest solute flux is related to flood events. High annual variation of Na⁺ concentration compared to conservative Cl⁻ as well as Chloro-Alkali indexes (CAI and CAI2) suggests that Na⁺ adsorption and desorption during ion-exchange reactions occur in the regolith. This Na⁺ variability, to some extent, explains weak Ca²⁺ and Mg²⁺ dilution effect during high water levels. During the measurement period (2014-2015), solute flux calculated per catchment area amounted to 49-69 t km⁻² a⁻¹ (tons per km per year). The chemical composition of water and discharge shows by far the highest chemical denudation of limestones and dolomites (87-89 %), while dissolution of gypsum is of minor importance (11-13 %). As a result, the carbonate karst solutional denudation rate is between 0.010 and 0.040 mm a⁻¹, where the higher values are more probable for longer periods due to the relatively low discharge during the spring of 2015. Comparison of dissolved and suspended loads indicates that the transport of suspended load is an order of magnitude less than transport of the dissolved load; the only exception is one flash flood event when suspended load exceeded the dissolved load. Besides a small decrease in solute flux as well as carbonate karst dissolution rates from NW to SE, no large hydrochemical differences between the three subwatersheds were detected.

INTRODUCTION

Rock weathering and denudation are important processes in landscape evolution (Phillips, 2005; Borelli et al., 2007; Viles, 2012; Krautblatter and Moore, 2014; Krklec et al., 2016). Denudation, the weathering away of Earth's surface, is the combined action of chemical and mechanical processes. The style and rate of denudation reflects complex relationships between tectonic activity, lithology, climate, and surface processes (Ryb et al., 2014). With time, these denudation processes change the thickness of bedrock and soil, as well as their physical, hydrological, and chemical properties (Kieffer et al., 1999; Chesworth, 2008; Minasny et al., 2008; Molina Ballesteros et al., 2013; Krklec et al., 2016) resulting in a feed-back loop between soil depth and denudation rate (Heimsath et al., 1997).

Chemical denudation plays a significant role in karst geomorphic systems. It has received significant quantification, especially from the second half of the 19th century. Such measurements, as well as their analysis and discussion, were strongly stimulated by Jeans Corbel's controversial conclusions in the 1950s. From analyses of thousands of field samples, he concluded that cold high mountains provide the most favorable environment for limestone dissolution, while hot regions have the lowest karst dissolution rates (Ford and Williams, 2007), which was in contrast with morphological evidence and conventional wisdom at the time.

Karst is a special style of landscape typically including leveled karst plains, enclosed depressions (dolines, cockpit, poljes) with conical hills, caves, and extensive underground water systems that are strongly influenced by chemical denudation of soluble rocks such as limestone, dolomite, marble, halite, and gypsum (Ford and Williams, 2007; Stokes et al., 2010). The unique features of karst landscapes are the effect of complex interactions between geology, climate, topography, hydrology, and biological factors over long time scales (Stokes et al., 2010). Carbonate karst landscapes occur worldwide, where carbonate rocks interact with fresh water, and cover 15.2 % of the ice-free continental area (Goldscheider, 2020) and 11 % (Raeisi, 2004) of Iran. Globally, 1.18 billion people (16.5 % of the global population) live on karst (Goldscheider, 2020) and nearly 20-25 % of the world population relies mostly or completely on karst aquifers

¹ Department of Range and Watershed Management Engineering, Faculty of Natural Resources and Agriculture, Lorestan University, Khorramabad, Iran

² Karst Research Institute ZRC SAZU, Postojna, Slovenia, <https://orcid.org/0000-0002-5415-0309>;

³ Department of Arid and Mountainous Regions Reclamation, Faculty of Natural Resources, University of Tehran, Iran

⁴ College of Science and Engineering, James Cook University, Cairns, Australia.

^C corresponding author mitja.prelovsek@zrc-sazu.si

(Ford and Williams, 2007); karst springs are important source of drinking and irrigation water in many subwatersheds of Iran (Ahmadipour, 1999).

Solution rates of carbonate minerals are several orders of magnitude higher than silicate minerals (Matsushi et al., 2010). Carbonate karst denudation rates can be measured using 5 main techniques (White, 2020): MEM, limestone tablets, hydrochemical, cosmogenic nuclides, and dated geomorphologic features. The MEM technique measures wall retreat using a portable rigid plate with a dial indicator seated on three steel studs imbedded into the rock. This technique is site-specific and can be used on bare rock only where subsoil dissolution is excluded. To get an insight into the overall dissolution rate in a catchment area, the hydrochemical method was used in this study. Since the bulk of dissolution takes place at the soil-bedrock contact, including epikarst (White, 2000), it is assumed that dissolved load measured by the hydrochemical approach mostly reflects surface lowering and relatively little is contributed by dissolution in vadose and phreatic zones. Some difficulties, constraints, and uncertainties of chemical denudation measurements in karst areas (e.g., surface of catchment area, extent of carbonate outcrop within catchment area, contribution of dissolved load by allogenic tributaries, dissolution of karst rocks overlain by protective caprock) have been presented in numerous papers internationally (White, 2000; Abu-Jaber et al., 2001; Krawczyk et al., 2003; Dixon and Thorn, 2005; Lauritzen, 2005; Gabrovšek, 2007, 2009; Kaufmann and Dreybrodt, 2007; Rzonca and Buczyński, 2013); in general, dissolution rates indicates a prevailing role of climate (runoff and soil CO₂ concentration). Based on the empirical work of Smith and Atkinson (1976) on carbonate dissolution rates in the 1970's, comparison of denudation rates measured in the field and empirical calculations with a numerical model has been synthesized and analyzed by White (2000).

To improve global models of karst denudation, additional quantitative data from representative karst areas are needed and processes related to dissolution should be further studied. Therefore, the purpose of this paper is to estimate the current solute load, flux, and intensity of the chemical denudation process of carbonate rocks, as well as interpret the variability of controlling hydrochemical parameters in three subwatersheds in Lorestan province, Iran.

STUDY AREA

The study area (Khorram Abad, Biranshahr and Alashtar subwatersheds) covers a part of the Lorestan province located in the southwestern Iran (Fig. 1). They are part of the Karkheh River basin (Persian Gulf drainage basin) with general characteristics (area, extent of carbonate outcrops, total runoff) summarized in Table 1.

The study area is located between 33°11' 47" N and 34°03' 27" N, and between 48°03' 10" E and 48°59' 07" E. The subwatersheds are defined according to the positions of sampling sites, and cover an area of 3,576 km². Elevation of the subwatersheds varies from 1,158 to 3,646 m a.s.l. (Fig. 2). Limestone and dolomite covers 1,262 km² (35 %), other carbonate rocks (mainly marls) 709 km² (20 %), Quaternary deposits (granular material of all grain sizes from pebbles to clay) 1,496 km² (42 %), evaporites (gypsum, halite, marl) 14 km² (0.4 %), and non-carbonate non-Quaternary rocks (sandstone, siltstone, conglomerate with red chert, andesite, rhyodacite, and radiolarites) 95 km² (3 %; Fig. 1). The upper part of the study area is mountainous, built mainly of Cretaceous and Miocene limestone, and the lower part is a plain with an old terrace formed on 25–150 m deep alluvial deposits (Ahmadipour, 2003; Fig. 2). The thickest carbonate sequences are in the Jurassic, Cretaceous, Miocene, and Oligocene rocks (Fig. 1). Dolomite can be found as beds in the Asmari Formation (Cucchi and Zini, 2003; Barmaki et al., 2019) and in thick carbonate deposits in the Triassic and Jurassic sequence. In the Zagros Mountains, the most extensive gypsum deposits are found in the Gachsaran Formation (Early Miocene), where gypsum makes up to two thirds of the stratigraphic sequence (Cucchi and Zini, 2003). Gypsum also occurs in the Aghajari Formation (stratigraphically located above the Gachsaran Formation), but due to uplift of the research area (Pusht-e-Kuh non-salt basin), the Gachsaran, as well as the Aghajari and Bakhtyari Formations, are either absent or are very poorly preserved (Bahroudi and Koyi 2004), and crop out only in a small area (14 km²) around the monitoring points of Alashtar and Khorram Abad subwatersheds. The most extensive halite deposits are found in the Hormoz Complex that was deposited during the Upper Precambrian to Middle Cambrian (Bosak et al., 1998); halite protrudes to the surface through the youngest formations as diapirs and, according to Mortazavi et al. (2017) and Nabavi and Agha Nabati (Aghanabati, 2004; Nabavi, 1976), extends at least several hundreds of kilometers SE of the research area (Bahroudi and Koyi, 2014). In the study area, the extent of the salt deposits of the Gachsaran Formation is of minor importance, covering only 0.01 km² of the Khorram Abad subwatershed. From a structural point of view, the research area is located at the NE part of the Zagros Fold and Thrust Belt (Mohammadi and Field, 2009); the NE part of the Alashtar subwatershed is located on the Crushed Zone bordering the Sanandaj-Sirjan Metamorphic Zone.

Climate data for Khorram Abad, Kakasherf, Biranshahr, Chamangir, Doab Visian, Alashtar, Sif Abad, Dorod, Kakareza, Kahman, Nor Abad, Rimeleh, Borojerd, Sepid Dasht and Kohdasht meteorological stations for 1997–2015 (Alashtar), 1990–2015 (Khorram Abad) and 2006–2015 (Biranshahr) were used to produce a climatic summary. The climate of the study area ranges from semi-arid to slightly humid with an annual temperature oscillation from –3.4 °C during the wet season to 31.7 °C during the dry season. The means of absolute minimum and maximum temperatures are –15.1 °C (January) and 42.9 °C (July), respectively. The average annual amount of precipitation is 478 mm with a peak in winter that

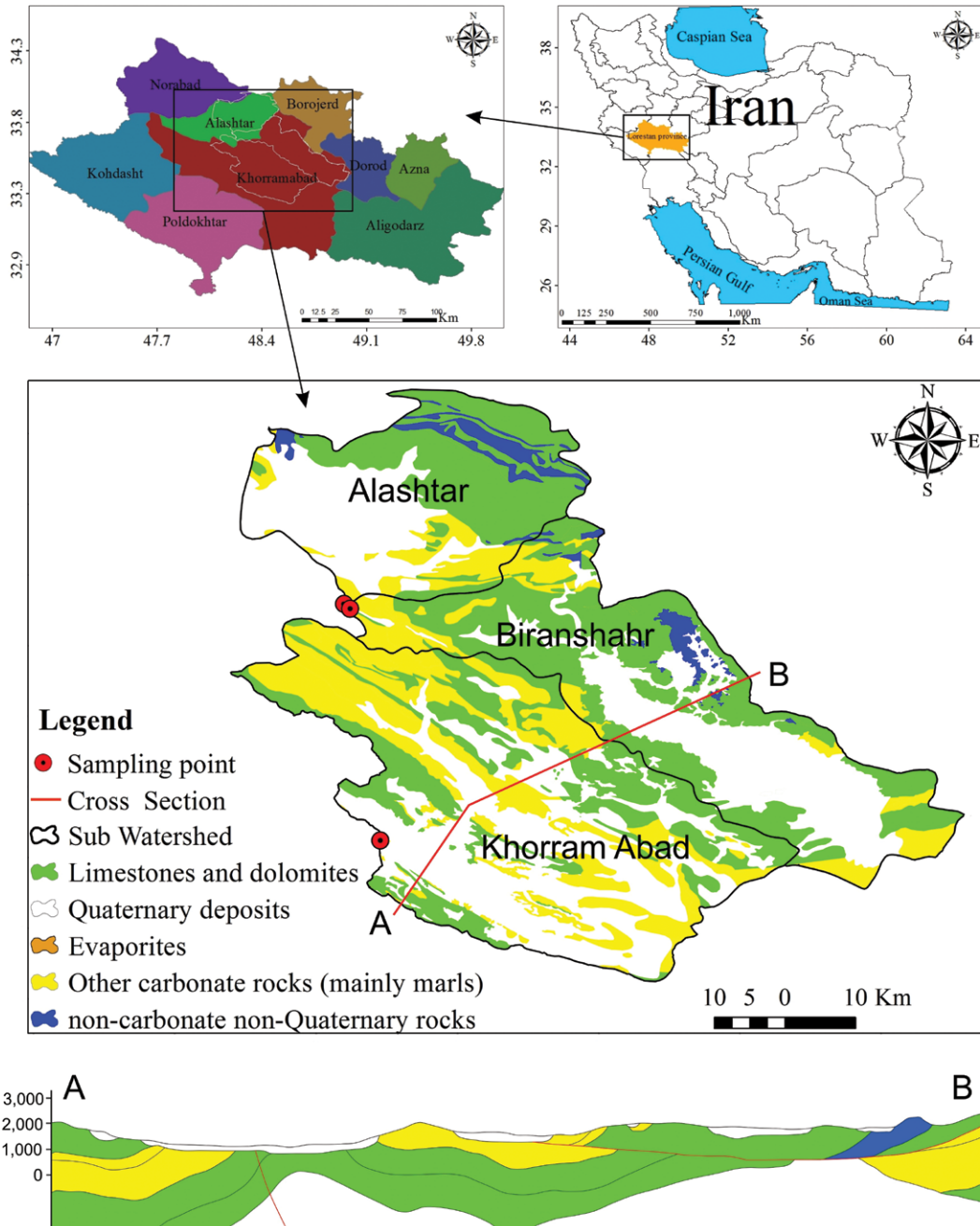


Figure 1. Map of the study area showing geological characteristics and location of sampling sites.

METHODS AND MATERIALS

Stream water was collected for one year from September 2014 to September 2015 (Appendix 1–3). Water samples were collected at depths of 30–100 cm approximately in the middle of the channel. The samples were collected in pre-washed 1 L polyethylene bottles three times a month. Electrical conductivity (EC), temperature and pH were measured using a portable multipara function (Lutron WA-2017SD) precalibrated before fieldwork with standard 4.01, 7.00, and 10.01 buffer solutions.

The samples were refrigerated and transported to the laboratory where chemical analyses were carried out within 1 day of collection. Chemical analysis of water samples (Cl^- , SO_4^{2-} , Ca^{2+} , Mg^{2+} , Na^+ , and K^+) was performed at the laboratory at the Natural Resources Faculty of Tehran University using a DIONEX ICS-2000 ion chromatograph, an AS18 (4 mm) analytical column and a CS16 (5 mm) analytical column. Alkalinity (HCO_3^- and CO_3^{2-}) was determined by automatic titration using a digital titrator. The error of the analysis was calculated using the ion charge balance control

is characteristic of the Mediterranean climate. Also, due to high altitude and continental influences, snow cover lasts 109, 49 and 56 days per year in Alashtar, Khorram Abad, and Biranshahr, respectively. During the measurement period, the river regimes, with primary spring and secondary autumn peaks, corresponded to 30-years-long average (1986-2016). However, due to the relatively low discharge in spring months, average annual discharge during the measurement period was lower by 27 %, 37 %, and 36 % compared to the 30-year-long average at Alashtar, Khorram Abad, and Biranshahr, respectively. While precipitation was on average 14 % higher than the 30-year-long average and all mean discharges of the bigger springs in the watersheds (Honam, Mota-heri, Golestan, and Bid Hal) were 36-66 % lower than average, the main reason for the smaller discharges in the studied watersheds is thought to be higher evapotranspiration.

Table 1. Basic lithological, hydrological, and hydrochemical characteristics of the subwatersheds. The extent (A) of carbonate outcrops of the individual catchment is further divided into limestones (L) with dolomites (D), marls (M), Quaternary deposits (Q), and evaporates (E).

Lithological, Hydrological, and Hydrochemical Characteristics	Alashtar	Khorram Abad	Biranshahr
Surface Land Area			
Subwatershed area (km ²)	804	1611	1160
A _{L+D} (km ² %)	350.9 (43.6 %)	402.3 (25.0 %)	508.4 (43.8 %)
A _{L+D+M} (km ² %)	446.4 (55.5 %)	857.3 (53.2 %)	667.1 (57.5 %)
A _{L+D+M+Q} (km ² %)	737.6 (91.7 %)	1601.8 (99.4 %)	1127.5 (97.2 %)
A _{L+D+M+Q+E} (km ² %)	742.6 (92.3 %)	1611.1 (100.0 %)	1127.5 (97.2 %)
non-carbonate (km ² %)	61.8 (7.7 %)	0.0 (0 %)	32.8 (2.8 %)
Surface Hydrology			
Precipitation during measurement period (mm a ⁻¹)	491	539	754
Total runoff (Mm ³ a ⁻¹)	170.8	168.8	198.1
Specific discharge (L s ⁻¹ km ⁻²)	6.4	6.4	7.5
Average Discharge (m ³ s ⁻¹)	5.42 ± 2.73	5.35 ± 3.45	6.28 ± 4.87
TDS _{AVG} (mg L ⁻¹)	277 ± 69	405 ± 81	266 ± 52
EC _{AVG} (μS cm ⁻¹)	431 ± 110	641 ± 133	414 ± 81
pH _{AVG} ^a	7.29	7.08	7.79
Surface Hydrochemistry			
Alkalinity (mmol L ⁻¹)	3.65 ± 0.81	4.66 ± 0.95	3.35 ± 0.48
Cl ⁻ (mmol L ⁻¹)	0.45 ± 0.14	1.43 ± 0.36	0.45 ± 0.39
SO ₄ ²⁻ (mmol L ⁻¹)	0.15 ± 0.11	0.21 ± 0.24	0.18 ± 0.11
Ca ²⁺ (mmol L ⁻¹)	1.33 ± 0.47	1.77 ± 0.40	1.35 ± 0.25
Mg ²⁺ (mmol L ⁻¹)	0.68 ± 0.37	1.14 ± 0.44	0.59 ± 0.26
Na ⁺ (mmol L ⁻¹)	0.22 ± 0.21	0.56 ± 0.45	0.26 ± 0.32
K ⁺ (mmol L ⁻¹)	0.06 ± 0.06	0.15 ± 0.18	0.03 ± 0.02

^a pH values were converted to hydrogen-ion concentrations before calculation of the means and standard deviations.

($|(C) - (A)| / |(C) + (A)|$); an error of >5 % was found in 13 of 36 samples, in 1 of 36 samples, and none in the 36 samples at Alashtar, Khorram Abad, and Biranshahr subwatersheds, respectively. The average of an absolute value of the error indicates the quality of data as being the best in Biranshahr (-0.3; 0.8) and the worst in Alashtar subwatershed (-2.7; 4.9). The predominantly negative charge balance error suggests that mainly cations were underestimated. Due to the acceptable average annual error, all data have been used in the calculation. Some caution should be adopted when results from the Alashtar subwatershed are considered where the reason for the high predominantly negative charge balance error is unknown: Pearson's correlation matrix in Table 2 suggests low impact of urban or agricultural pollutants like Cl⁻ and K⁺ and excess of Ca²⁺.

To analyze suspended load, the samples were collected in prewashed 1 L polyethylene bottles and analyzed at the same institution as the chemical analyses. The samples were unmoved for 48 h to allow the suspended sediment to settle and the upper sediment-free part of the water column decanted. The remaining suspension was filtered through pre-weighed Whatman filter papers (Chow et al., 2007), dried at 105 °C in an oven for 24 h (Sadeghi et al., 2009; Sadeghi and Saeidi, 2010), weighed again, and the weight difference calculated.

The stream discharge was measured by combining velocity measurements, using a propeller-type current meter, corrected for 0.85 (to get representative average river flow velocity), and the wetted cross-section area to give the instantaneous discharge at the moment of sampling. Discharge measurements are consistent with the procedure of The Regional Water Company of Lorestan that performs regular discharge measurements at various sampling locations. The speciation, the degree of saturation with respect to calcite (SI_{cal}), and equilibrium pCO₂ of the waters were calculated using the PHREEQC Interactive geochemical code, version 3.1.7.9213 (Parkhurst and Appello, 2013).

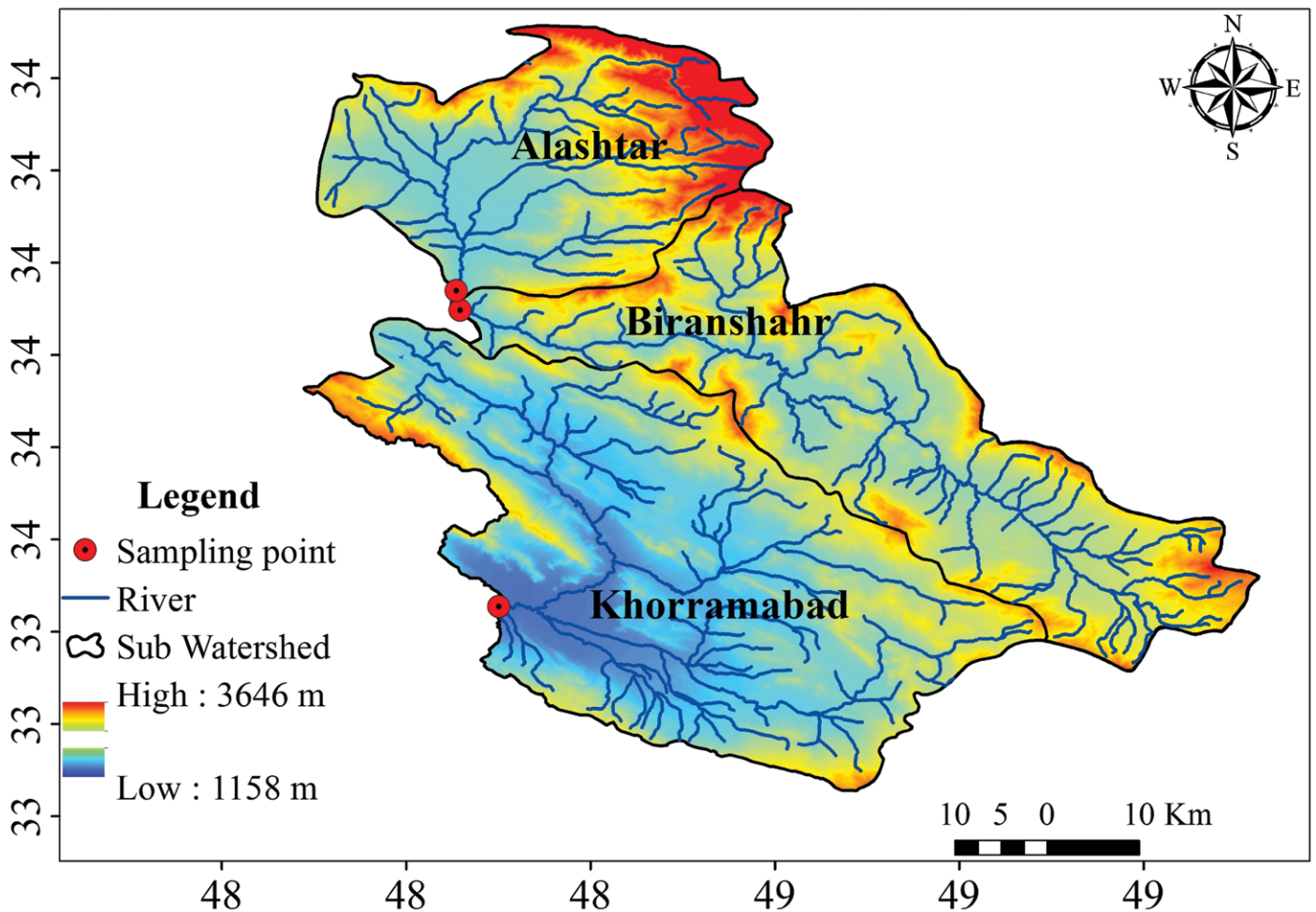


Figure 2. Terrain, hydrological network and subwatersheds of the study area.

Calculation of the net solutional denudation rate of carbonates

Three equations were used for calculation of the net solutional denudation rate of carbonates. An annual quantity of dissolved carbonates (limestone and dolomite) was calculated as a running total of all Ca^{2+} and Mg^{2+} fluxes at the sampling times by Equation (1)

$$S_c = \sum_{i=1}^{36} [C_i Q_i \left(\frac{365}{36} \times 24 \times 60 \times 60 \right)], \quad (1)$$

where S_c ($\text{kg as CaCO}_3 \text{ a}^{-1}$) refers to the sum of Ca^{2+} and Mg^{2+} load per year expressed as calcite (CaCO_3), i refers to equal time intervals, C_i ($\text{kg as CaCO}_3 \text{ m}^{-3}$) is the sum of the Ca^{2+} and Mg^{2+} concentration expressed as calcite during sampling campaigns, Q_i ($\text{m}^3 \text{ s}^{-1}$) is discharge during sampling campaigns, and 36 refers to the annual number of samples. The last bracketed part of the equation was used for time conversion. Since the extent of evaporite outcrops in each subwatershed is not significantly reflected in measured SO_4^{2-} concentration, Ca^{2+} concentration was not reduced for molar concentration of SO_4^{2-} that could, to some extent, derive from gypsiferous evaporates.

The volume of dissolved carbonates (V_c in m^3) was obtained by Equation (2)

$$V_c = \frac{S_c}{\rho_c}, \quad (2)$$

where ρ_c is the weighted average of the specific gravities (kg m^{-3}) which is $2,634 \text{ kg m}^{-3}$ (average of 6 sampled limestones in all subwatersheds).

The carbonate karst denudation rate was calculated by Equation (3)

$$D = \frac{V_c}{A} 10^9, \quad (3)$$

where D is the solutional denudation rate of carbonates (mm a^{-1}) and A (km^2) is the area of carbonate outcrop. Since the latter is not related to limestone and dolomite outcrops only, carbonate dissolution rate was separately calculated

for area of limestones and dolomites only (A_{L+D}), extended for outcrops containing substantial amounts of carbonates (mainly marls; A_{L+D+M}), extended for Quaternary carbonate-bearing deposits ($A_{L+D+M+Q}$), and extended for evaporites ($A_{L+D+M+Q+E}$), the differences between which are marked, especially due to the vast extent of Quaternary deposits in all subwatersheds and marls in Khorram Abad (Table 1). The subdivision of the studied subwatersheds into homogeneous sub-basins to avoid the impact of allogenic streams on solutational denudation rates of carbonate karst, proposed by Lauritzen (1990), was not possible due to the spatial complexity of the subwatersheds. Therefore, the results can be considered as an outcome of a mixed denudation system (Ford and Williams, 2007).

RESULTS

In all three subwatersheds, the increasing order of the average solute molar concentrations (Table 1), as well as the solute molar flux, is $Ca^{2+} > Mg^{2+} > Na^+ - K^+$ for cations and $(HCO_3^- + CO_3^{2-}) \gg Cl^- > SO_4^{2-}$ for anions. On average, the sum of bicarbonate and carbonate ions represents from 74 to 84 mol% of all analyzed anions. Among major cations, Ca^{2+} (51–62 mol%) is most closely followed by Mg^{2+} (27–33 mol%).

Ternary plots (Fig. 3) indicate the prevalence of Ca-Mg- HCO_3 water for all three subwatersheds. Khorram Abad is notably characterized by a relatively higher share of Cl^- as well as Na^+ indicating dissolution of Na^+ and Cl^- bearing rocks (e.g. halite). A sample from Biranshahr taken in the middle of May 2015 has an exceptionally high concentration of Cl^- and Na^+ and is most probably an outlier related to contamination with salt in the field or laboratory as the concentration is far higher than expected from the discharge (Fig. 4A) or runoff (Fig. 4B), and small charge-balance error

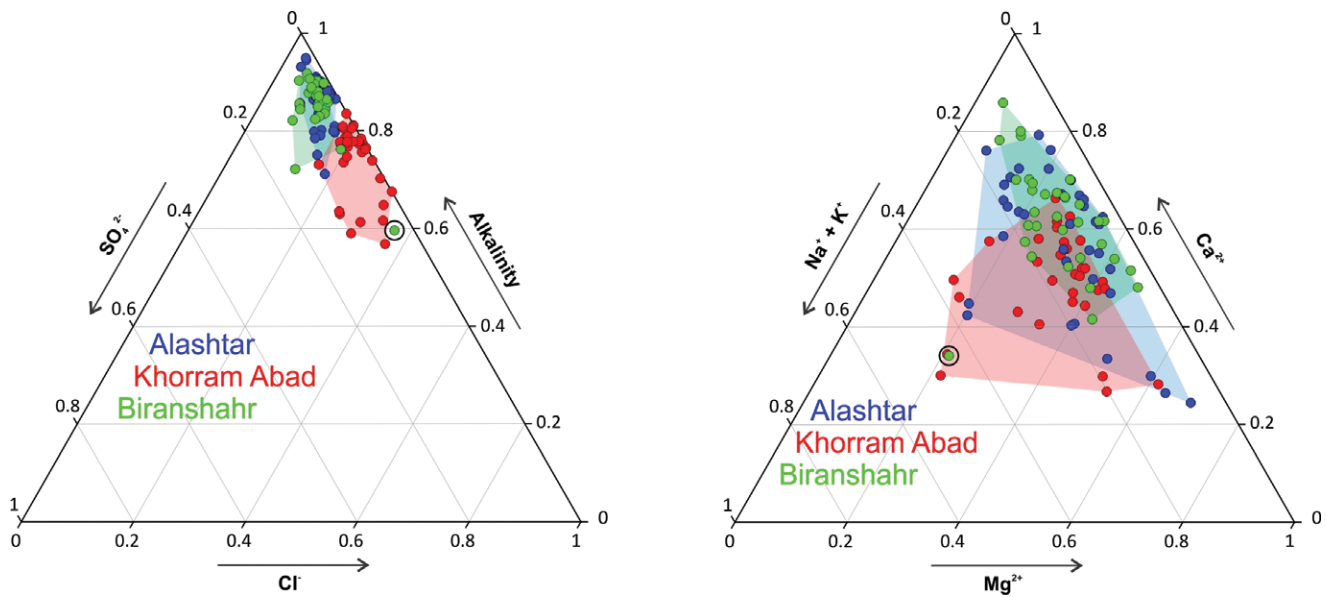


Figure 3. Ternary plot of the major anions and cations (in mol%) for the three studied subwatersheds. The encircled sample is recognized to be an outlier and was excluded from further evaluation.

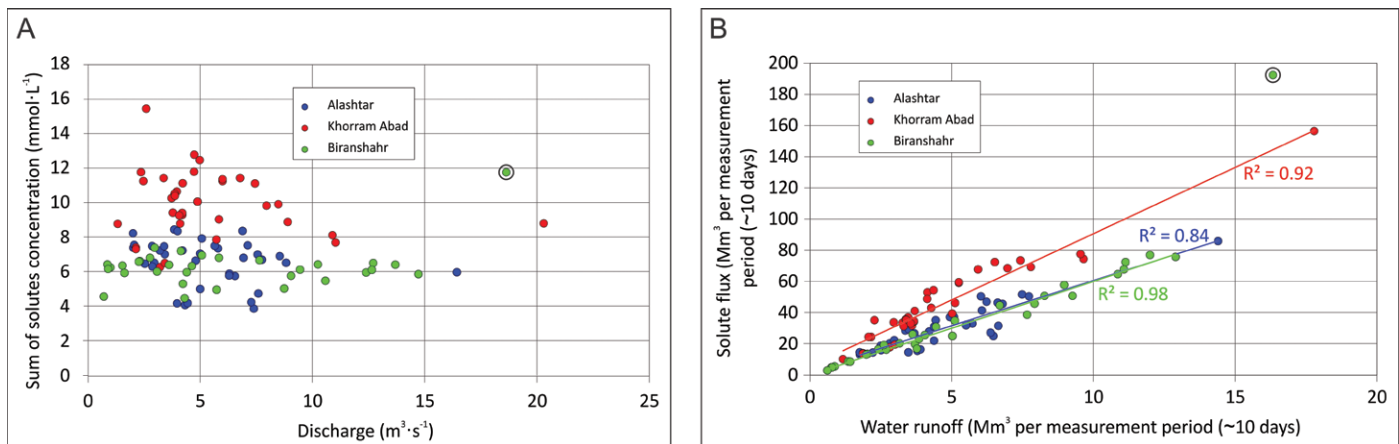


Figure 4. Relations between (A) solute concentration and discharge and (B) solute runoff and water runoff. An outstanding value (outlier) detected in Biranshahr subwatershed is circled and was excluded from calculation of the r^2 .

(+0.1), while the concentrations of other ions are within expectations. The dominant concentrations of Ca^{2+} and Mg^{2+} among other cations (usually >80 mol%) and (bi)carbonate (usually >70 mol%) indicates dissolution of limestone as well as dolomite. The share of SO_4^{2-} is low in all three subwatersheds (usually >10 mol%) indicating a relatively small amount of dissolution of gypsum compared to limestones and dolomites.

All solute concentrations (Table 1), as well as annual solute flux, are highest in Khorram Abad subwatershed. The other two are similar in solute concentrations but Biranshahr shows a higher solute flux due to higher total runoff. If subwatershed areas are taken into account, solute flux per area is the highest in Alashtar ($1.356 \text{ Mmol km}^{-2} \text{ a}^{-1}$ or $68.55 \text{ t km}^{-2} \text{ a}^{-1}$) followed by Biranshahr ($1.049 \text{ Mmol km}^{-2} \text{ a}^{-1}$ or $53.61 \text{ t km}^{-2} \text{ a}^{-1}$) and Khorram Abad ($1.02 \text{ Mmol km}^{-2} \text{ a}^{-1}$ or $48.54 \text{ t km}^{-2} \text{ a}^{-1}$).

The connection between discharge and the sums of solutes is weak and not statistically significant in all three studied cases (Table 2, Fig. 4A). The lowest sums of solute concentrations were not recorded during flood events showing

Table 2. Pearson's correlation matrix between measured parameters and dissolved species for all three studied subwatersheds (top: Alashtar; middle: Khorram Abad; bottom: Biranshahr; Σ_{sol} = sum of solutes; C-B_e = charge-balance error).

	ρCO_2	SI_{Cal}	C-B_e	Σ_{sol}	K^+	Na^+	Mg^{2+}	Ca^{2+}	SO_4^{2-}	Cl^-	HCO_3^-	CO_3^{2-}	pH	EC	TDS
Q	-0.08	0.02	-0.13	-0.24	-0.24	-0.01	-0.25	-0.03	0.19	0.14	-0.28	-0.02	0.07	-0.26	-0.28
	0.02	-0.06	-0.35	-0.15	-0.18	-0.03	-0.12	-0.09	-0.09	0.04	-0.15	0.07	-0.04	-0.13	-0.06
	0.03	0.05	0.07	0.09	0.33	-0.22	0.17	0.06	0.04	0.05	0.14	-0.13	0.03	0.30	0.30
TDS	0.02	0.15	0.22	0.87	0.52	-0.04	0.58	0.37	0.25	0.47	0.79	-0.01	-0.09	0.96	
	0.35	0.01	0.14	0.75	-0.08	0.20	0.51	0.61	0.49	0.52	0.60	-0.06	-0.19	0.82	
	-0.02	0.32	0.06	0.79	0.52	-0.09	0.53	0.46	0.38	0.35	0.73	-0.02	0.13	1.00	
EC	0.02	0.16	0.14	0.89	0.52	-0.03	0.60	0.33	0.25	0.47	0.82	0.00	-0.07		
	0.23	0.24	0.13	0.98	0.49	0.44	0.49	0.67	0.58	0.61	0.76	0.09	0.03		
	-0.02	0.32	0.04	0.81	0.52	-0.11	0.54	0.46	0.38	0.32	0.75	0.00	0.13		
pH	-0.87	0.90	0.04	-0.09	-0.13	0.28	-0.21	0.05	0.31	0.02	-0.19	0.03			
	-0.88	0.95	-0.17	0.05	0.26	0.24	-0.09	-0.09	0.01	-0.05	0.03	0.20			
	-0.93	0.94	0.04	-0.02	-0.08	0.31	-0.31	0.22	-0.32	0.21	-0.02	0.21			
CO_3^{2-}	-0.07	0.01	-0.14	0.08	-0.20	0.73	-0.14	-0.02	0.42	0.33	-0.14				
	-0.04	0.21	-0.48	0.13	0.18	0.32	-0.13	0.04	0.08	0.10	0.01				
	-0.12	0.24	-0.52	0.15	0.02	-0.05	0.04	0.06	-0.22	-0.30	0.21				
HCO_3^-	0.15	0.16	-0.02	0.92	0.41	-0.12	0.28	0.57	-0.05	0.26					
	0.18	0.28	0.20	0.83	0.41	-0.02	0.57	0.59	0.01	0.13					
	0.17	0.27	-0.18	0.93	0.39	0.01	0.38	0.58	0.03	0.00					
Cl^-	0.08	0.13	-0.05	0.50	0.12	0.35	0.20	0.20	0.49						
	0.17	0.01	0.15	0.57	0.35	0.33	0.22	0.41	0.45						
	0.08	0.15	0.00	0.26	-0.18	0.09	0.02	0.09	0.10						
SO_4^{2-}	-0.21	0.32	-0.01	0.24	0.03	0.34	0.10	0.10							
	0.12	0.03	-0.09	0.48	0.19	0.62	0.15	0.27							
	0.25	-0.28	0.19	0.28	0.19	-0.42	0.45	0.10							
Ca^{2+}	-0.04	0.46	0.39	0.64	0.13	0.07	-0.40								
	0.27	0.20	0.01	0.66	0.23	0.14	-0.06								
	-0.02	0.52	0.08	0.59	0.23	-0.03	-0.36								
Mg^{2+}	0.13	-0.29	0.13	0.30	0.35	-0.33									
	0.12	-0.04	0.39	0.52	0.13	-0.25									
	0.24	-0.31	-0.09	0.47	0.31	-0.32									
Na^+	-0.28	0.27	-0.08	0.10	-0.19										
	0.02	0.23	-0.14	0.38	0.36										
	-0.22	0.09	0.02	-0.03	-0.42										
K^+	0.10	-0.03	0.14	0.43											
	-0.08	0.32	0.12	0.56											
	0.19	0.03	0.23	0.33											
Σ_{sol}	0.06	0.26	0.15												
	0.22	0.27	0.18												
	0.15	0.26	0.06												
C-B_e	-0.13	0.16													
	0.15	-0.16													
	0.00	0.02													
SI_{Cal}	-0.79														
	-0.78														
	-0.80														

Note: Significant correlation ($p < 0.05$) is in bold. To calculate coefficients, molar concentrations of ionic species were used; the outlier from mid-May 2015 (Biranshahr) was excluded from calculated correlations with Na^+ and Cl^- .

a minor effect of dilution during high discharge. As a result, in the available data, seasonal fluctuations of solute runoff mostly depend on seasonally (or event-driven) discharge indicated also by very high r^2 values (Fig. 4B). In all three cases, the solute runoff seasonal maxima are observed in spring months and minima in autumn reflecting the river flow regimes (Fig. 5). The impact of single flood events on solute runoff is very high with more than a two-fold increase of solute runoff above usual as can be observed in February 2015 in Khorram Abad and in May 2015 in the Biranshahr subwatershed. Even on the scale of individual parameters (Table 2), Pearson correlation coefficients between discharge and anions or cations are usually negative to very low with high variation between subwatersheds.

Pearson's correlation matrix (Table 2) shows expectedly high positive and significant correlations between TDS (or EC) and the sums of solutes, as well as with all major ions (HCO_3^- , Mg^{2+} , Ca^{2+} as well as Cl^- , K^+ , and SO_4^{2-} but to a lesser extent). Besides Mg^{2+} – Ca^{2+} and Mg^{2+} – Na^+ pairs, generally positive correlation can be found between major ionic species. Relatively high and significant positive correlation is evident for HCO_3^- with Ca^{2+} , K^+ and Mg^{2+} . Except in the Biranshahr subwatershed, Cl^- is positively correlated with SO_4^{2-} and Na^+ . Significant correlation of TDS or EC with Na^+ is mostly absent indicating different mechanisms of Na^+ transport compared to other major ions. Additionally, correlation between Ca^{2+} and SO_4^{2-} as well as Na^+ and Cl^- , which could indicate dissolution of gypsum ($\text{CaSO}_4 \cdot 2\text{H}_2\text{O}$) and halite (NaCl), respectively, is weak and it is significant for Na^+ – Cl^- ionic pair only in the case of the Alashtar and Khorram Abad subwatersheds. The seasonal course of the Na^+/Cl^- ratio shows extremely high annual variation being 0.06–1.48, 0.12–1.10, and 0.10–2.26 for the Alashtar, Khorram Abad, and Biranshahr subwatersheds, respectively. In the Alashtar and Khorram Abad, oscillation during measurement period occurs in the form of waves with 3–4 peaks. Much better Pearson's correlations exist between groups of common ion-pairs (e.g. between $(\text{Ca}^{2+} + \text{Mg}^{2+})$ and $(\text{HCO}_3^- + \text{CO}_3^{2-})$) being +0.79, +0.84 and +0.83 for Alashtar, Khorram Abad, and Biranshahr, respectively. As expected, the highest significant correlations (TDS-EC, pH- Si_{Cal} , pH- $p\text{CO}_2$, $\text{Si}_{\text{Cal}}-p\text{CO}_2$) are characteristic for dependent parameters in karst waters.

Based on the geological map (Fig. 1), the concentration of Ca^{2+} can be mainly attributed to limestone and gypsum dissolution while Mg^{2+} can be mainly attributed to dissolution of dolomite. In the case of solely and moderate to intensive limestone or dolomite dissolution, if concentrations of less abundant species, such as, H^+ and OH^- are neglected, $(\text{Ca}^{2+} + \text{Mg}^{2+})/(\text{HCO}_3^- + \text{CO}_3^{2-})$ molar ratios should be close to 0.5; in all researched subwatersheds it is higher (0.55–0.63) indicating CO_2 outgassing and/or additional sources of Ca^{2+} , such as gypsum. The addition of SO_4^{2-} to $(\text{HCO}_3^- + \text{CO}_3^{2-})$ slightly reduces the molar ratio (0.53–0.61) and to some extent, explains the additional source of Ca^{2+} by dissolution

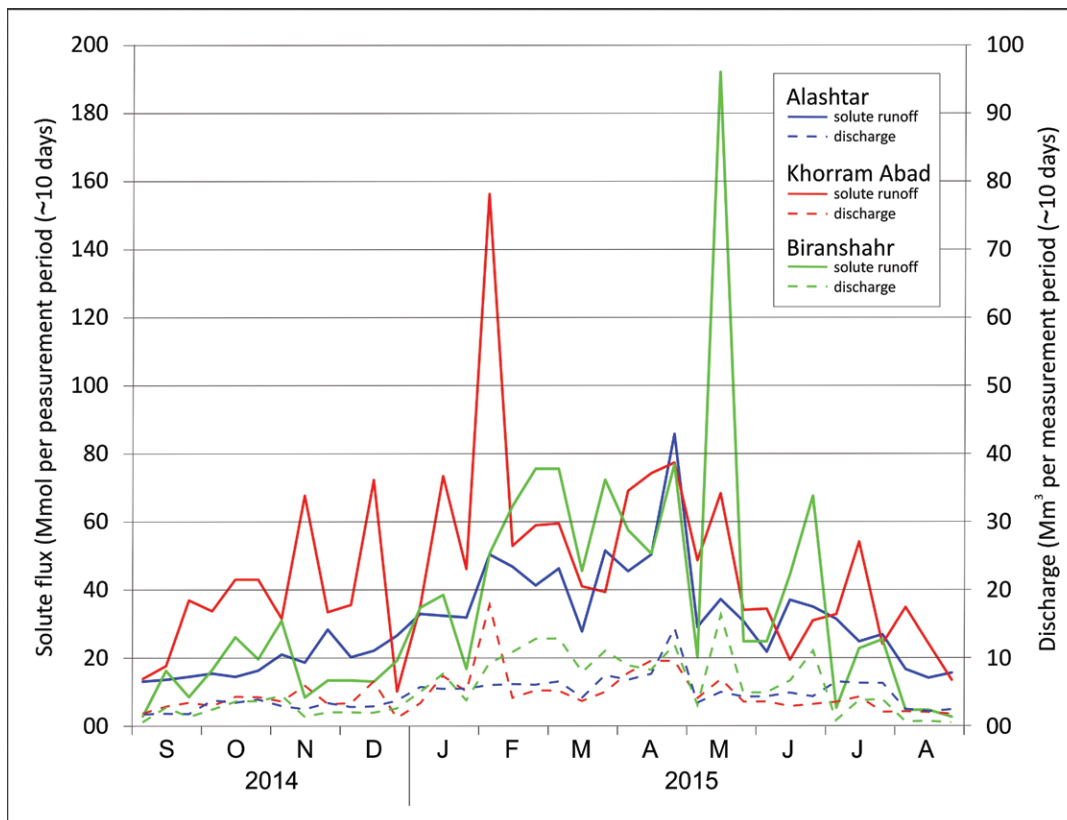


Figure 5. The seasonal course of solute runoff (full line) compared to discharge (dashed line).

of gypsum. Based on the annual solute flux, the molar $\text{SO}_4^{2-}/\text{Ca}^{2+}$ ratios are 0.12, 0.11, and 0.13 for Alashtar, Khorram Abad, and Biranshahr, respectively, indicating the dominant (87–89 %) effect of carbonate dissolution, while dissolution of gypsum ($\text{CaSO}_4 \cdot 2\text{H}_2\text{O}$) plays a minor role (11–13 %). Presence of SO_4^{2-} and slightly positive Pearson's correlation between Ca^{2+} and SO_4^{2-} , which is not significant (Table 2) could indicate dissolution of gypsum. Therefore, to calculate the carbonate karst solutional denudation rate, the annual flux of Ca^{2+} and Mg^{2+} (as CaCO_3) was related only to the area of carbonate-bearing depos-

its (Table 1). Results show that the carbonate karst solutional denudation rate is between 0.011 and 0.045 mm a⁻¹ (or between 0.010 and 0.040 mm a⁻¹ if dissolution of gypsum is taken into account) (Table 3). Large variations are mostly a result of differences in the uncertain areas of carbonate-bearing deposits (2.1 times difference in Alashtar to up to 4 times difference in Khorram Abad) and, to a lesser extent, the differences between studied watersheds (1.3–1.5 times difference) indicating closer similarity of dissolution rates when based on the same rock type. Generally, the highest carbonate solutional denudation rates are at Alashtar and the lowest in the Biranshahr subwatershed.

The seasonal course of carbonate karst solutional denudation rate basically reflects seasonal fluctuations of discharge that is highest in late winter and during spring and is lowest during the late summer months and autumn in all subwatersheds (Fig. 6). The values of r^2 for linear Pearson's correlations of carbonate solutional denudation rate with discharge are high in

Table 3. Fluxes of Ca²⁺ and Mg²⁺ and solutional denudation rate from carbonate outcrops taking into account the areas of different carbonate-bearing deposits (L: limestones; D: dolomites; M: marls; Q: Quaternary deposits (see Table 1)) and the impact of gypsum dissolution (12 %, 11 % and 13 % for Alashtar, Khorram Abad and Biranshahr, respectively).

Fluxes and Denudation Rates	Alashtar	Khorram Abad	Biranshahr
Flux of Ca ²⁺ + Mg ²⁺			
Mmol a ⁻¹	333.3	480.6	393.1
t as CaCO ₃ a ⁻¹	33,359	48,104	39,347
m ³ as CaCO ₃ a ⁻¹	12,665	18,263	14,938
Solutional denudation rate (mm as CaCO ₃ a ⁻¹)			
A _{L+D}	0.032	0.040	0.025
A _{L+D+M}	0.025	0.019	0.019
A _{L+D+M+Q}	0.015	0.010	0.011

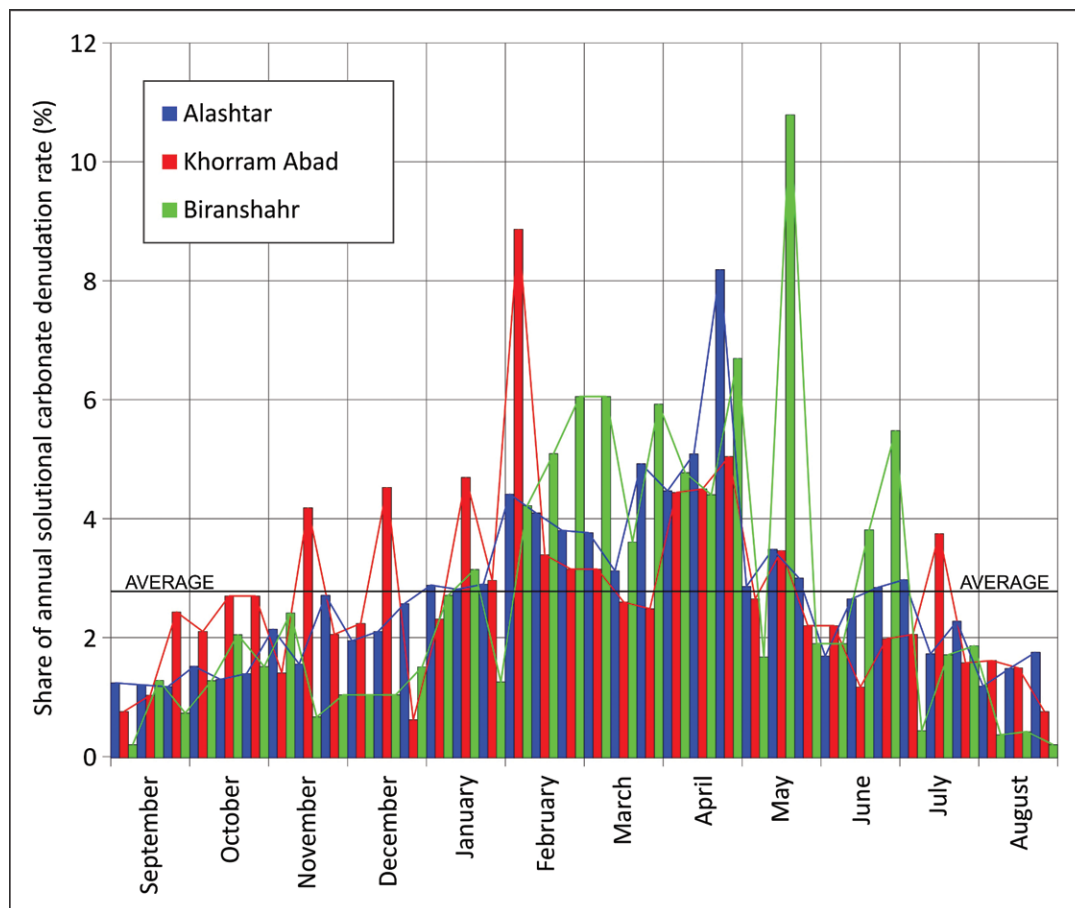


Figure 6. The annual course of solutional denudation rates.

all three subwatersheds (i.e. 0.80, 0.91, and 0.95 for Alashtar, Khorram Abad, and Biranshahr, respectively). Especially during summer, fluctuations of solutional carbonate karst denudation rates depend strongly on floods; one event can be responsible for 8–11 % of the annual solutional carbonate karst denudation rate (over 3-times the average). During low discharge, solutional carbonate karst denudation rates can be 10-times lower than for the average of all discharges. The highest annual fluctuations, as observed from standard the deviations, are 2.37 % for the Biranshahr subwatershed and only 1.44 % for Alashtar and 1.58 % for Khorram Abad.

DISCUSSION

Solute load and geological structure

The dominant Ca-Mg-HCO₃ type of water is consistent with the geology (Fig. 1), with the previous hydrochemical studies in Zagros region (Barmaki et al., 2019) and indicates substantial dissolution of carbonate outcrops (Table 1). Concentrations of Mg²⁺ suggest a considerable extent of dolomite-bearing rocks (up to 51 %, 64 %, and 44 % of all carbonates in the case of Alashtar, Khorram Abad, and Biranshahr, respectively, if all Mg²⁺ derives from dolomite dissolution), as well as possibly other Mg-bearing rocks since Pearson's correlation coefficient, *r*, between Mg²⁺ and HCO₃⁻ is low for all subwatersheds and not significant for the Alashtar subwatershed (Table 2). The presence of SO₄²⁻, Cl⁻, and Na⁺ indicates the importance of evaporite rocks, especially in the Khorram Abad subwatershed. Higher concentration of Cl⁻ and Na⁺ (Fig. 3) in the case of Khorram Abad is expected due to 9.3 km² (0.6 % of subwatershed) of halite outcrops. Despite the share of halite outcrops in the Alashtar subwatershed being nearly the same (0.6 %; 5 km²), the concentrations of Cl⁻ and Na⁺ are low, which could be explained to some extent by slightly higher specific discharge in Alashtar resulting in higher dilution. However, the annual solute flux, which indicates the quantity of Na⁺ or Cl⁻ leaving a subwatershed in one year, does not support this. Since Biranshahr subwatershed shows very similar averages of Cl⁻ and Na⁺ concentration as Alashtar but higher annual solute flux than Alashtar (due to higher specific discharge and catchment area) despite an absence of mapped halite outcrops, halite deposits are probably more widespread than shown on the geological map of Biranshahr and Alashtar subwatersheds or halite is widely available as aeolian dust within the weathering zone. Average SO₄²⁻/Cl⁻ molar ratios (0.36, 0.14, and 0.5 for Alashtar, Khorram Abad, and Biranshahr, respectively) suggest more intensive dissolution of halite than gypsum. Despite the fact that at least dissolution of carbonates could depend on seasonal CO₂ production (Ford and Williams, 2007), none of the analyzed ions (except Na⁺ to some extent) indicates strong seasonality.

The presence of SO₄²⁻ could indicate dissolution of gypsum and/or the presence of natural or anthropogenic sources of H₂SO₄. While not significant but slightly positive Pearson's correlation between Ca²⁺ and SO₄²⁻ (Table 2) could point to dissolution of gypsum, moderate to strong but always significant correlation between (Ca²⁺ + Mg²⁺)/(HCO₃⁻ + CO₃²⁻) and SO₄²⁻ (*r* = 0.358 and *p* < 0.05, *r* = 0.481 and *p* < 0.05, *r* = 0.84 and *p* < 0.05 for Alashtar, Khorram Abad, and Biranshahr, respectively) rather indicates the presence of H₂SO₄ as the source of SO₄²⁻.

IMPACT ON SOLUTE LOAD OF PRECIPITATION, BIOCHEMICAL ALTERATION AND INTERACTION WITH THE ATMOSPHERE

Measured solute load is a result of precipitation input, biochemical dissolution, biochemical alteration (solute uptake/precipitation and release, ion-exchange processes) in weathering zones and water bodies, interaction with the atmosphere especially in surface flows (e.g., CO₂ outgassing), and anthropogenic impacts such as contamination of air and water (from agriculture, industrial activity and domestic wastewater). To estimate the contribution of precipitation to solute load, the chemical composition of precipitation from the cities of Arak (Markazi Province, Iran; Ghadimi et al., 2013) and Shiraz (Fars province, Iran; Moore and Attar, 2011) was taken into account. Ion concentrations in rainwater summarized in Table 4 show high variability and very high averages, in the case of Ghadimi et al. (2013) exceeding the average annual concentration of SO₄²⁻ and Na⁺ in all three studied watersheds. Even average concentrations by Moore and Attar (2011) are unreliable since the share of the precipitation input exceeds solute concentrations in 53–94 % of samples for SO₄²⁻, 24–93 % of samples for Na⁺ and 37–45 % of samples for K⁺ in the studied subwatersheds. In contrast, the minimum ion concentration in rainwater from the data of Moore and Attar (2011) are at least 1.5-times lower than that of Ghadimi et al. (2013) and seems to be the most reliable for use in the study area. These data suggest that the highest contributions by rainwater can be expected for SO₄²⁻ (16 %), Na⁺ (23 %), Cl⁻ (7 %), K⁺ (3 %), and Ca²⁺ (2 %) (all other ions <1 %) indicating seawater (SO₄²⁻, K⁺, Na⁺, Cl⁻) and aeolian dust (calcite, gypsum, halite) as the most plausible sources. Awadh (2012) found that the western Sahara wind (locally known as *simoom*) that also affects West Asia mostly comprises quartz (49.0 %), calcite (35.6 %), feldspar (5.0 %) and gypsum (4.9 %) while it is poor in dolomite (2.42 %), indicating this area as a possible dust source. Differences in precipitation input shares between watersheds show slightly higher share of Na⁺

Table 4. Range of ion concentrations in rainwater (min-max) with averages in parentheses as measured in Shiraz (Moore and Attar, 2011) and Arak (Ghadimi et al., 2013).

Location	HCO ₃ ⁻ + CO ₃ ²⁻ (mmol L ⁻¹)	Cl ⁻ (mmol L ⁻¹)	SO ₄ ²⁻ (mmol L ⁻¹)	Ca ²⁺ (mmol L ⁻¹)	Mg ²⁺ (mmol L ⁻¹)	Na ⁺ (mmol L ⁻¹)	K ⁺ (mmol L ⁻¹)
Shiraz	0.00–0.13 (0.01)	0.04–0.30 (0.14)	0.01–0.71 (0.15)	0.03–1.63 (0.31)	0.01–0.23 (0.04)	0.04–0.69 (0.13)	0.00–0.34 (0.04)
Arak	0.28–1.52 (1.02)	0.06–0.40 (0.12)	0.03–1.56 (0.45)	0.01–1.58 (0.63)	0.01–1.83 (0.40)	0.05–4.35 (0.82)	0.01–0.03 (0.03)

and Cl^- in precipitation in Alashtar and Biranshahr indicating higher halite aeolian sources and higher share of SO_4^{2-} in Khorram Abad. The highest non-precipitation contribution to solute load is calculated to be for $(\text{HCO}_3^- + \text{CO}_3^{2-})$ that is primarily related to dissolution of carbonates (carbonate karst denudation).

During all samplings, equilibrium water $p\text{CO}_2$ was constantly above atmospheric concentration (~ 400 ppm) with an average of 10,890 ppm indicating CO_2 outgassing from the water into the atmosphere. Positive SI_{cal} (76 % of samples) indicates even higher original $p\text{CO}_2$ before CO_2 outgassing started; since $p\text{CO}_2$ shows no seasonality, high initial CO_2 concentration is most likely related to the underground karst system and less to biogenic production in surface streams. Only one sample was found to have SI_{cal} higher than 1 (rough threshold for calcite precipitation, based on Dreybrodt, 1988) indicating a low likelihood of calcite precipitation (downstream decline of Ca^{2+} as well as HCO_3^- and CO_3^{2-}).

Anthropogenic inputs to solute load are unknown due to an absence of reliable data; one could expect an anthropogenically-induced increase of K^+ , especially in Alashtar subwatershed due to intensive agriculture in the WS-central part of the basin. While the highest original $p\text{CO}_2$ concentration (15,136 ppm) indicates natural processes in the Biranshahr subwatershed, anthropogenic CO_2 sources (agriculture, waste water) are plausible in the Khorram Abad (equilibrium $p\text{CO}_2$ max 69,183 ppm, 5 samples above 50,000 ppm) and the Alashtar subwatershed (equilibrium $p\text{CO}_2$ max 69,183 ppm, 2 samples above 50,000 ppm). However, anthropogenic inputs are expected to be relatively low due to the weak or absent negative correlation between contaminant concentrations and discharge (Table 2) that would be expected due to a dilution effect.

Solute load and ion-exchange process

While the highest values of Pearson's correlation coefficients (from +0.57 to +0.59) are found between Ca^{2+} and HCO_3^- for all subwatersheds (Table 2), other correlation coefficients between ionic species are surprisingly low, sometimes negative, and often lack significance even between common ion-pairs (e.g. Na^+-Cl^- , $\text{Mg}^{2+}-\text{HCO}_3^-$, $\text{Ca}^{2+}-\text{Mg}^{2+}$), indicating the importance of lithologies other than limestone, as well as complex and heterogeneous interactions in the weathering zone.

The average Na^+/Cl^- molar ratios are low but similar: 0.53, 0.60 and 0.61 for Alashtar, Khorram Abad, and Biranshahr subwatershed, respectively. Low Na^+/Cl^- molar ratios seem to be typical for the Alashtar and Khorram Abad subwatershed (Ahmadipour, 1999) as well as for SW Iran (Adinehvand and Raeisi, 2018). The much lower annual solute flux of Na^+ compared to Cl^- (0.49:1, 0.39:1, 0.49:1 for Alashtar, Khorram Abad, and Biranshahr watershed, respectively) indicates a relatively weak effect of the weathering of Na-bearing minerals, strong Na^+ -prevailing modification of evaporated seawater from east Mediterranean seawater in precipitation (Na^+/Cl^- molar ratio of 0.86), low impact of solutes in precipitation (average Na^+/Cl^- molar ratio above 0.88; Moore and Attar, 2011; Ghadimi et al., 2013), and/or possible, but less likely, anthropogenic Cl^- sources such as coal combustion, waste incineration, or sea-salt dechlorination (Thimonier et al., 2008). The Na^+/Cl^- molar ratio is also very different from that in Lake Urmia, the biggest nearby salt lake located 550 km northwest (0.86; Alipour, 2006), with a tendency toward the low values found in some other lakes, such as the Dead Sea (0.28). The very high standard deviations of average Na^+/Cl^- molar ratios (± 0.41 , ± 0.29 , ± 0.44) with a relatively high annual coefficient of variation of Na^+ concentrations compared to Cl^- concentrations indicates Na^+ adsorption and desorption during ion-exchange reactions in the weathering zone. This idea is supported by a negative correlation between the Na^+/Cl^- molar ratio and Cl^- concentration as has been found to be indicative for soil adsorption by Neal and Kircher (2000). The Chloro-Alkali Index (CAI; $[\text{Cl}^- - (\text{Na}^+ + \text{K}^+)] / [\text{Cl}^-]$; in meq L^{-1}) and Chloro-Alkali Index 2 (CAI2; $[\text{Cl}^- - (\text{Na}^+ + \text{K}^+)] / [\text{SO}_4^{2-} + \text{HCO}_3^-]$; in meq L^{-1}), which are often used as indicators of ion-exchange processes (Schoeller, 1977; Hussien and Faiyad, 2016), are positive on average at the subwatershed scale ($0.32 < \text{CAI} < 0.5$; $0.04 < \text{CAI2} < 0.15$) suggesting higher Na^+ and K^+ release into the groundwater compared to Ca^{2+} and Mg^{2+} during ion-exchange processes. Pearson's correlation of CAI and CAI2 with discharge is weakly positive (+0.19, +0.13, and +0.17 for Alashtar, Khorram Abad, and Biranshahr, respectively) but negative when restricted to low discharges (Fig. 7A) indicating Na^+ and K^+ desorption during low discharge, when Mg^{2+} as well as Ca^{2+} should be absorbed, and reverse exchange during high discharge that could partly explain the absence of Ca^{2+} and Mg^{2+} decrease due to dilution during high discharge (Fig. 4A where Ca^{2+} and Mg^{2+} are considered as the main constituents of total solute load). Among the studied watersheds, especially CAI indicates several-months-long high values with short intervals of low (slightly negative) values (Fig. 7B). Beside the conservative ion Cl^- , the main factor especially for CAI is Na^+ (and not K^+) suggesting that Na^+ is the most susceptible monovalent cation during ion exchange, which is consistent with Mg^{2+} when compared with K^+ or Na^+ . While the relationship between of Mg^{2+} and K^+ shows a positive correlation, the relation of Mg^{2+} with Na^+ is negative indicating cation exchange between Mg^{2+} and K^+ with Na^+ . Similar negative correlation between Na^+ and Mg^{2+} in all three watersheds (Table 2) suggests that the main cation exchange occurs between these two species due to a similar tendency for adsorption. Adsorption is indicated by the coefficient of variation that increases from strongly absorbed Ca^{2+} (0.19–0.35) over moderately absorbed Mg^{2+} (0.39–0.54) to weakly absorbed Na^+ (0.54–0.94) and K^+ (0.82–1.18); as a rule, the $\text{Mg}^{2+}/\text{Na}^+$ molar ratio also increases with discharge. Due to

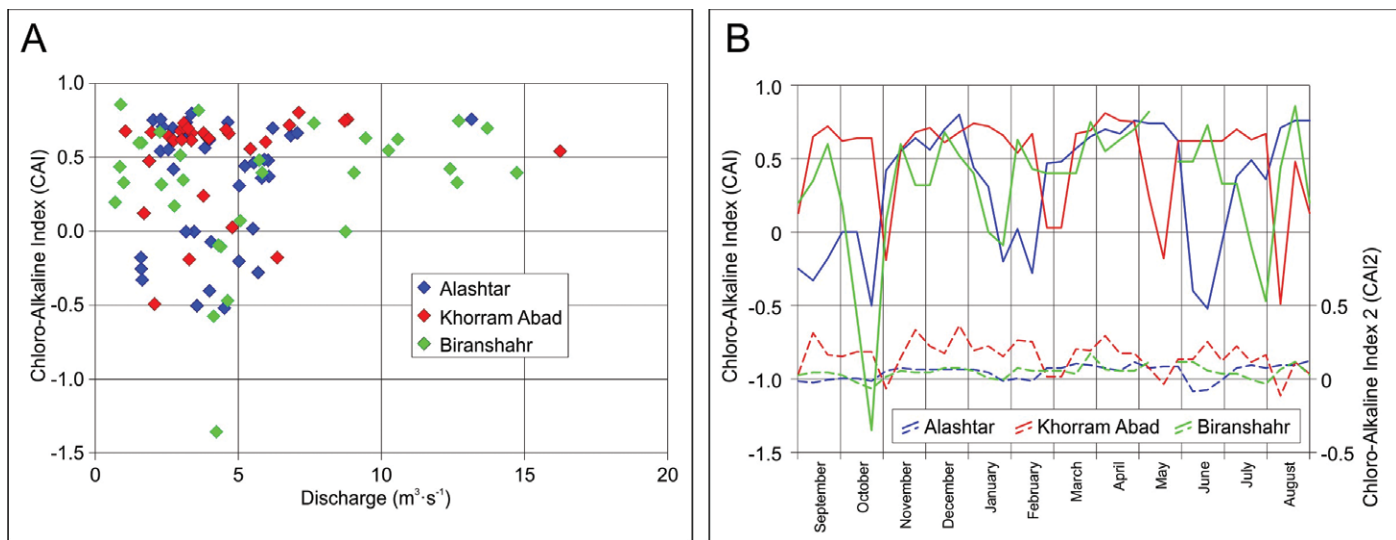


Figure 7. Correlation of (A) Chloro-Alkaline Index (CAI) with discharge and (B) seasonal pattern of both indexes (CAI – full line; CAI2 – dashed line).

Na^+ sorption and desorption, Pearson's correlation between Na^+ and Cl^- is much lower (Table 2) than expected solely from halite dissolution.

Solutal and carbonate karst denudation rate

The solutal load is the quantity of bedrock leaving the catchment area in solution due to chemical weathering and precipitation input, assuming that ion-exchange sorption and desorption are balanced during a year of observation. The solute flux, expressed as average annual material loss per area, was found to be the highest in Alashtar ($69 \text{ t km}^{-2} \text{ a}^{-1}$), followed by Biranshahr ($54 \text{ t km}^{-2} \text{ a}^{-1}$) and Khorram Abad ($49 \text{ t km}^{-2} \text{ a}^{-1}$). The highest impact on differences is from the alkalinity and concentration of Ca^{2+} . A decrease of solutal load trends from NW to SE that might indicate a climatic effect as a result of different altitudes (Fig. 2). The same decrease was found for carbonate karst dissolution rates calculated for all possible carbonate outcrops (L+D+M+Q; $r^2 = 0.81$, $p = 0.13$; Table 3) but is not significant ($p < 0.05$) without an additional subwatershed.

As already described, by far the highest solute flux of Ca^{2+} , Mg^{2+} and HCO_3^- is from limestone and dolomite, and is much less for gypsum (12–14 %), while the precipitation input of Ca^{2+} (2 %) and Mg^{2+} (<1 %) can be neglected. Carbonate karst dissolution rates calculated per area strongly depend on the area of carbonate outcrops in each subwatershed (Table 3); since carbonate dissolution certainly takes place on limestones and dolomites, the presence of areas of marls and Quaternary deposits can have an opposite role and dilute the solute flux from the carbonate rocks. While thin and not substantially eluviated regolith on marls can provide even higher water hardness than limestone or dolomite massifs, especially during low water levels (Gams, 1966), accumulation of thick regolith and leaching on a geological timescale can stimulate surface runoff and substantially reduce chemical interaction with marls. Dissolution rates of Quaternary deposits mostly depend on carbonate content, prior leaching, as well as thickness of regolith. On the contrary, weathering of extensive outcrops of allogenic rocks can provide Ca^{2+} and Mg^{2+} ions at the contact with carbonates due to highly aggressive allogenic water (Lauritzen, 1990; Gabrovšek, 2009); the latter situation can increase denudation rates up to $203 \text{ m}^3 \text{ km}^{-2} \text{ a}^{-1}$ as shown by a study of an area of 0.0362 km^2 of marble-striped karst affected by sulfate waters in the Polish Sudetes Mountains (Rzonca and Buczyński, 2013) or more than $50 \text{ m}^3 \text{ km}^{-2} \text{ a}^{-1}$ in SW Spitsbergen (Pulina et al., 1984). To ensure reliable comparison, despite year-to-year fluctuations, our results have been compared only with results derived using a similar hydrochemical approach (Table 5) since at least part of endokarst dissolution is absent using MEM or limestone tablets, and fluctuation of dissolution rates on geological time scales should be taken into account when results of a measured thickness of dissolved carbonate divided by age (e.g., post-glacial formation of limestone pedestals) are used (Gams, 1985; Plan, 2005; Häuselmann, 2008; Gabrovšek, 2009). Despite a 3-fold difference in the areas over which dissolution has been calculated ($0.010\text{--}0.040 \text{ mm CaCO}_3 \text{ a}^{-1}$ or $10\text{--}40 \text{ m}^3 \text{ as CaCO}_3 \text{ km}^{-2} \text{ a}^{-1}$ including the dissolution of gypsum), carbonate karst dissolution rates at Alashtar, Khorram Abad, and Biranshahr subwatersheds are similar to those found on slightly elevated karst plateaus in Central Europe with warm and humid summer continental climate (e.g., SW Poland according to Pulina, 1974, 1977) and on the bare karst of northern Norway, but less than in the mountainous areas of the Alps, Pyrenees, Tatras, and Dinaric mountains.

Table 5. Comparison of carbonate karst dissolution rates calculated by a hydrochemical approach.

Carbonate Denudation Rate ($\text{m}^3 \text{ km}^{-2} \text{ a}^{-1}$)	Region (comment)	Source
10–40	Alashtar, Khorram Abad, Biranshahr subwatershed, Iran (491–754 mm a^{-1})	This study
4–35	Svalbard, Norway (bare karst)	Krawczyk, 2008
20.5–33	Sudetes karst, Poland	Pulina, 1977
32.5 ± 10.2	Northern Norway (bare karst; 2,600 mm precipitation a^{-1})	Lauritzen, 1990
48–89	Baget karst system, Pyrenees, France (5-years-long study)	Bakalowicz, 1979
60–70	Classical Karst, Slovenia	Gams, 1966
90–100	Alpine Karst, Slovenia	Gams, 1966
61–88	Waitomo, New Zealand	Gunn, 1981
82	Kościełiski Creek, Western Tatra Mountains, Poland	Barzyk, 1998

The excellent connection between water and solute runoff (Fig. 4B), where Ca^{2+} and Mg^{2+} are responsible for 80–90 % of solute runoff, indicates a primary role of water runoff on solute runoff, as well as on carbonate karst dissolution rate in all studied subwatersheds. The relation is linear and is consistent with previous observations where solute runoff was compared with discharge (Julian et al., 1978; Pulina et al., 1984) or where yearly dissolution rate was compared with yearly runoff (Gabrovšek, 2009) in selected catchments despite the fact that other climatic (temperature, CO_2 concentration) and lithologic factors could affect the seasonality of carbonate karst denudation rate. Pulina et al. (1984) observed a (quasi)logarithmic relationship between stream discharge and solute load in the calcite undersaturated waters of Spitsbergen. Residuals between measured and runoff-based calculated karst dissolution rates (according to trend lines in Fig. 4B) do not show seasonal patterns that are often thought to be a result of dissolution-related factors (temperature, CO_2 production). An absence of lower solute concentration during high discharge (Fig. 4B) shows a negligible effect of dilution during flood events, as was found at some karst springs in the Zagros Mts. (Mohammadi and Field, 2009) and interpreted to be a result of a large underground aquifer and/or small non-rapid recharge component.

Solute load vs. suspended load

Determination of suspended load based on occasional sampling makes possible a comparison of solute load with suspended load. While solute load varies between 195 and 429 mg L^{-1} (avg. = 330 mg L^{-1}), 276 and 727 mg L^{-1} (avg. = 472 mg L^{-1}), and 222 and 510 mg L^{-1} (avg. = 313 mg L^{-1}) in Alashtar, Khorram Abad, and Biranshahr subwatershed, respectively, suspended load is approximately one magnitude lower at 10–119 mg L^{-1} (avg. = 46 mg L^{-1}), 6–1,217 mg L^{-1} (avg. = 127 mg L^{-1}), and 7–155 mg L^{-1} (avg. = 41 mg L^{-1}). The only case where the suspended load was higher than the solute load was at the beginning of February 2015 (Khorram Abad; 3-times higher than the solute load), when the highest discharge was recorded during sampling (4-times the average discharge). As a result, the ratio between solute and suspended load is high; on average 1:0.14, 1:0.30, and 1:0.13 in Alashtar, Khorram Abad, and Biranshahr subwatershed, respectively. The correlation between discharge and suspended load is negligible and not significant ($r = -0.02$; $p = 0.97$) as between discharge and solute load in Alashtar, moderate and significant in Biranshahr ($r = +0.52$; $p < 0.05$), and much higher and significant in the case of Khorram Abad ($r = +0.80$; $p < 0.05$) where the aforementioned flood event, with exceptionally high suspended load of 1,217 mg L^{-1} had a large effect. During this flood event, the concentration of suspended sediment was higher than the sum of all concentrations in 28 other samples, showing an important role of flash floods for the mobilization of fine-grained sediment. According to the ratios between the annual solute and the suspended loads calculated as tonnes per sampling period, the solute load comprises 88 %, 66 %, and 85 % of solute+suspended load in Alashtar, Khorram Abad, and Biranshahr, respectively. If we assume that bed load represents 0.2–0.6 % in the case of Karkheh River (Hassanzadeh et al., 2011), the solution load is responsible for the majority of measured overall (mechanical+chemical) denudation. Except during very high discharge, when more intensive mobilization of suspended and bed load is expected, while solute load is expected to be more stable, dissolution is recognized as the crucial process of surface denudation.

CONCLUSIONS

The main process affecting the composition of surface water in the study area is carbonate dissolution, contributing three abundant species: HCO_3^- , Ca^{2+} and Mg^{2+} . The fourth most abundant ion (Cl^-) could indicate dissolution of halite that should influence the concentration of Na^+ too. However, the concentration of Na^+ is much less than Cl^- , and is annually highly variable and controlled by ion-exchange processes probably in the regolith. As a result, correlations between Cl^- and Na^+ concentrations is low in all three subwatersheds. Very low average concentration of Na^+ compared to Cl^- as well as annual flux of the Na^+/Cl^- ratio indicates very weak weathering of Na-bearing minerals, a strong

modification of evaporated seawater from the east Mediterranean Sea in precipitation, or low impact of solutes in precipitation, and/or possible, but less likely, anthropogenic Cl^- sources.

No obvious seasonal pattern (except for Na^+) and extremely weak correlation of analyzed species with discharge show multiple and complex processes within the heterogeneous lithology of the studied catchment areas. Due to fairly good average negative Pearson's correlations, that is significant in the case of Alashtar subwatershed, it seems that during ion exchange Na^+ substitutes mainly for Mg^{2+} . This can to some extent explain the lack of Mg^{2+} variation during flood events when Mg^{2+} can be substituted in the ion-exchange process with Na^+ while the process is opposite during low discharges.

Despite the fact that carbonate karst denudation rates calculated from hydrochemical data are faced with several problems (e.g., delineation of carbonate outcrops, the possibility that sulfate rocks contribute to Ca^{2+} and Mg^{2+} fluxes, and a role for carbonate dissolution by allogenic waters with $\text{SI}_{\text{Cal/DoI}} \ll 0$), it is still an appropriate method for obtaining a first-order estimate of solutional denudation (Ford and Williams, 2007). Since there is negligible input of Ca^{2+} and Mg^{2+} (from 2 to <1 %) from precipitation as well as Ca^{2+} due to dissolution of gypsum (11–13 %), the calculation of carbonate karst dissolution rates was possible and found to be from 10 to $40 \text{ m}^3 \text{ km}^{-2} \text{ a}^{-1}$. Since solute flux is strongly determined by discharge, which was 27–37 % lower than the 30-year-long average during the measurement period due to relatively small runoff probably caused by higher evapotranspiration rates, higher dissolution rates are expected over long periods. Due to 11.9–28.2 % share of subwatersheds being underlain by marl, that can enhance or hinder carbonate dissolution, the calculated differences between subwatersheds are not reliable. Since solute and carbonate fluxes mainly depend on discharge, solutional carbonate karst denudation rates strongly depend on floods: one event detected over ~ 10 days of sampling contributed up to 8–11 % of the annual denudation rate while during low discharge the denudation was 10-times below the average.

Comparison between suspended and solute loads shows generally much higher solute load indicating that dissolution is the controlling process for surface denudation. However, the solute load is 3-times lower during flash flood events due to the mobilization of large amounts of fine-grained sediment that reverses this relationship.

No major hydrochemical differences were detected between the three subwatersheds. However, a small decrease in both the solute flux from NW to SE and carbonate karst dissolution rates calculated for all possible carbonate outcrops (L+D+M+Q) might indicate a climatic effect as a result of different altitudes of the subwatersheds.

ACKNOWLEDGEMENTS

We thank the laboratory at the Natural Resources Faculty of Tehran University and the Iran National Science Foundation (INSF) for supporting this study (Project Code: 93038031) and the Slovenian Research Agency (P6-0119 Karst Research Programme) for the possibility to evaluate gathered data. Authors appreciate comments by Augusto Auler and another anonymous reviewer that improved the quality of this paper.

REFERENCES

- Abu-Jaber, N., Hess, J.W., and Howcroft, W., 2001, Chemical erosion of the Lilburn Cave system, Kings Canyon National Park, California: *Ground Water*, v. 39, no. 2, p. 223–229. <https://doi.org/10.1111/j.1745-6584.2001.tb02303.x>.
- Adinehvand, R., and Raeisi E., 2018, Characterization of a karst aquifer in a complex tectonic region, Southwestern Iran: *Journal of Cave and Karst Studies*, v. 80, no. 4, p. 190–205. <https://doi.org/10.1111/j.1745-6584.2001.tb02303.x>.
- Aghanabati, A., 2004, *Geology of Iran: Geological Survey & Mineral Explorations of Iran (GSI)*, v. 1, 640 p.
- Ahmadipour, M.R., 1999, Karst terraines in Iran – Examples from Lorestan: *Acta Carsologica*, v. 28, no. 2, p. 213–224. <https://doi.org/10.3986/ac.v28i2.494>.
- Ahmadipour, M.R. 2003, Karst Springs of Alashtar, Iran: *Acta Carsologica*, v. 32, no. 2, p. 244–254. <https://doi.org/10.3986/ac.v32i2.352>.
- Alipour, S., 2006, Hydrogeochemistry of seasonal variation of Urmia Salt Lake, Iran: *Saline Systems*, v. 2, no. 9. <https://doi.org/10.1186/1746-1448-2-9>.
- Awadh, S.M., 2012, Geochemistry and mineralogical composition of the airborne particles of sand dunes and dust storms settled in Iraq and their environmental impacts. *Environmental Earth Sciences*, v. 66 no. 8, p. 2247–2256. <https://doi.org/10.1007/s12665-011-1445-6>.
- Bahroudi, A., and Koyi, H., 2004, Tectono-sedimentary framework of the Gachsaran Formation in the Zagros foreland basin: *Marine and Petroleum Geology*, v. 21, p. 1295–1310. <https://doi.org/10.1016/j.marpetgeo.2004.09.001>.
- Bakalowicz, M., 1979, Contribution de la géochimie des eaux à la connaissance de l'aquifère karstique et de la karstification, [Ph.D. Dissertation]: Univ. Paris-6, 269 p.
- Barczyk, G., 1998, Denudacja chemiczna krasu węglanowego w świetle badań stacjonarnych zlewni potoków Chochołowski i Kościeliskiego (Tatry Zachodnie) [Chemical denudation of carbonate karst in the catchments of Chochołowski and Kościeliski Creeks based on research using stationary measurement stations (the western Tatra Mountains)]: *Kras i speleologia*, v. 18, no. 9, p. 223–233.
- Barmaki, M.D., Rezaei, M., Raeisi, E., and Ashjari, J., 2019, Comparison of surface and interior karst development in Zagros Karst Aquifers, Southwest Iran: *Journal of Cave and Karst Studies*, v. 81, no. 2, p. 84–97. <https://doi.org/10.4311/2017ES0120>.
- Borelli, L., Greco, R., and Gulia, G., 2007, Weathering grade of rock masses as a predisposing factor to slope instabilities: reconnaissance and control procedures: *Geomorphology*, v. 87, no. 3, p. 158–175. <https://doi.org/10.1016/j.geomorph.2006.03.031>.
- Bosak, P., Jaroš, J., Spudil, J., Sulovsky, P., Václavek, V., 1998, Salt Plugs in the Eastern Zagros, Iran: *Results of Regional Geological Reconnaissance: GeoLines*, v. 7, p. 3–174.
- Chesworth, W., 2008, *Encyclopedia of Soil Science*: Springer, Dordecht, 902 p. <https://doi.org/10.1007/978-1-4020-3995-9>.

- Chow, V.T., Maidment, D.R., Mays, L.W., 2007, *Applied hydrology*: McGraw-Hill, New York, 588 p.
- Cucchi, F., and Zini L., 2003, Gypsum karst of Zagros Mountains (I.R. Iran): *Acta Carsologica*, v. 32, no. 1, p. 69–82. <https://doi.org/10.3986/ac.v32i1.365>.
- Dixon, J., Thorn, C., 2005, Chemical weathering and landscape development in midlatitude alpine environments: *Geomorphology*, v. 67, no. 1-2, p. 127–145. <https://doi.org/10.1016/j.geomorph.2004.07.009>.
- Dreybrodt, W., 1988, *Processes in Karst Systems (Physics, Chemistry, and Geology)*: Springer-Verlag, Berlin-Heidelberg-New York-London-Paris-Tokyo, 288 p.
- Ford, D.C., and Williams, P.W., 2007, *Karst Geomorphology and Hydrology*: John Wiley & Sons, Chichester, 562 p.
- Gabrovšek, F., 2007, On denudation rates in karst: *Acta Carsologica*, v. 36, no. 1, p. 7–13. <https://doi.org/10.3986/ac.v36i1.203>.
- Gabrovšek, F., 2009, On concepts and methods for the estimation of dissolutional denudation rates in karst areas: *Geomorphology*, v. 106, no. 1-2, p. 9–14. [10.1016/j.geomorph.2008.09.008](https://doi.org/10.1016/j.geomorph.2008.09.008)
- Gams, I., 1966, Faktorji in dinamika korozije na karbonatnih kameninah slovenskega dinarskega in alpskega krasa. [Factors and dynamics of corrosion of the carbonatic Rocks in the Dinaric and Alpine Karst of Slovenia (Yugoslavia)]: *Geografski vestnik*, v. 38, p. 11–68.
- Gams, I., 1985, Mednarodne primerjalne meritve površinske korozije s pomočjo standardnih apneniških tablet [International comparative measurements of surface solution by means of standard limestone tablets], *Razprave IV: Razreda*, v. 26, p. 361–388.
- Ghadimi, F., Ghomi, M., Ranjbar, M., and Hajati, A., 2013, Sources of contamination in rainwater by major and heavy elements in Arak, Iran: *Journal of Water Sciences Research*, v. 5, no. 2, p. 67–82.
- Goldscheider, N., Chen, Z., Auler, A.S., Bakalowicz, M., Broda, S., Drew, D., Hartmann, J., Jiang, G., Moosdorf, N., Stevanovic, Z., Veni, G., 2020, Global distribution of carbonate rocks and karst water resources: *Hydrogeology Journal*. <https://doi.org/10.1007/s10040-020-02139-5>.
- Gunn, J., 1981, Limestone solution rates and processes in the Waitomo district, New Zealand: *Earth Surface Processes and Landforms*, no. 6, v. 5, p. 427–445. <https://doi.org/10.1002/esp.3290060504>.
- Hassanzadeh, H., Faiznia, S., Shafai Bajestan, M., and Motamed, A., 2011, Estimate of Sediment Transport Rate at Karkheh River in Iran Using Selected Transport Formulas: *World Applied Sciences Journal*, v. 13, no. 2, p. 376–384.
- Häuselmann, P., 2008, Surface corrosion of an Alpine karren field: recent measures at Innerbergli (Siebenhengste, Switzerland): *International Journal of Speleology*, v. 37, no. 2, p. 107–111. <https://doi.org/10.1002/esp.3290060504>.
- Heimsath, A.M., Dietrich, W.E., Nishiizumi, K., and Finkel, R.C., 1997, The soil production function and landscape equilibrium: *Nature*, v. 388, p. 358–361. <https://doi.org/10.1038/41056>.
- Hussien, B.M., and Faiyad, A.S., 2016, Modeling the Hydrogeochemical Processes and Source of Ions in the Groundwater of Aquifers within KasraNukhaib Region (West Iraq): *International Journal of Geosciences*, v. 7, no. 10, p. 1156–1181. <http://doi.org/10.4236/ijg.2016.710087>.
- Julian, M., Martin, J., and Nicod, J., 1978, Les karsts Méditerranéens: *Mediterranean*, v. 32, no. 1-2, p. 115–131. <https://doi.org/10.3406/med-it.1978.1775>.
- Kaufmann, G., and Dreybrodt, W., 2007, Calcite dissolution kinetics in the system $\text{CaCO}_3\text{-H}_2\text{O-CaCO}_3$ at high undersaturation: *Geochimica et Cosmochimica Acta*, v. 71, no. 6, p. 1398–1410. <https://doi.org/10.1016/j.gca.2006.10.024>.
- Kieffer, B., Jové, C.F., Oelkers, E.H., and Schott, J., 1999, An experimental study of the reactive surface area of the Fontainebleau sandstone as a function of porosity, permeability, and fluid flow: *Geochimica et Cosmochimica Acta*, v. 63, no. 21, p. 3525–3534. [https://doi.org/10.1016/S0016-7037\(99\)00191-X](https://doi.org/10.1016/S0016-7037(99)00191-X).
- Krautblatter, M., and Moore J.R., 2014, Rock slope instability and erosion: toward improved process understanding: *Earth Surface Processes and Landforms*, v. 39, no. 9, p. 1273–1278. <https://doi.org/10.1002/esp.3578>.
- Krawczyk, W.E., 2008, The range of chemical denudation rates on Svalbard, in *Geophysical Research Abstracts 10*, EGU General Assembly 2008.
- Krawczyk, W.E., Lefauconnier, B., and Pettersson, L.-E., 2003, Chemical denudation rates in the Bayelva Catchment, Svalbard, in the Fall of 2000: *Physics and Chemistry of the Earth Parts A/B/C*, v. 28, no. 28-32 p. 1257–1271. <https://doi.org/10.1016/j.pce.2003.08.054>.
- Krklec, K., Villar, D., Carrasco, R.M., and Pedraza, J., 2016, Current denudation rates in dolostone karst from central Spain: Implications for the formation of unroofed caves: *Geomorphology*, v. 264, p. 1–11. <https://doi.org/10.1016/j.geomorph.2016.04.007>.
- Lauritzen, S.-E., 1990, Autogenic and allogenic denudation in carbonate karst by the multiple basin method—an example from Svartisen, north Norway: *Earth Surface Processes and Landforms*, v. 15, no. 2, p. 157–167.
- Lauritzen, S.-E., 2005, A simple growth model for allogenic Karrentische, in *Final Programme & Abstract Book, Proceedings of the 14th International Congress of Speleology, 21st–28th August 2005, Athens–Kalamos, Greece*.
- Maire, R., 1981, Karst and hydrogeology synthesis: *Spelunca*, no. 3, p. 23–30.
- Matsushi, Y., Sasa, K., Takahashi, T., Sueki, K., Nagashima, Y., and Matsukura, Y., 2010, Denudation rates of carbonate pinnacles in Japanese karst areas: Estimates from cosmogenic ^{36}Cl in calcite: *Nuclear Instruments and Methods*, v. 268, no. 7-8, p. 1205–1208. <https://doi.org/10.1016/j.nimb.2009.10.134>.
- Minasny, B., McBratney, A.B., and Salvador-Blanes, S., 2008, Quantitative models for pedogenesis - a review: *Geoderma*, v. 144, no. 1, p. 140–157. <https://doi.org/10.1016/j.geoderma.2007.12.013>.
- Mohammadi, Z., and Field, M.S., 2009, On the Temporal Behavior of Karst Aquifers, zagros Region, Iran: A Geostatistical Approach: *Journal of Cave and Karst Studies*, v. 71, no. 3, p. 210–226. <https://doi.org/10.4311/jcks2009es0079>.
- Molina Ballesteros, E., Garcia-Talegon, J., Herrero Fernandez, H., and Inigo, A.C., 2013, Changes of porosity due to weathering in quartzites and slates of a Rana profile (Montes de Toledo, Central Spain): *Estudios Geológicos*, v. 69, no. 2, p. 179–191. <https://doi.org/10.3989/egol.41185.252>.
- Moore, F., and Attar, A., 2011, Rainwater and the resulting runoff chemistry in Shiraz city, southwest Iran: *International Journal of Environmental Studies*, v. 68, no. 5, p. 703–717. <https://doi.org/10.1080/00207233.2011.591898>.
- Mortazavi, M., Heuss-Assbichler, S., and Shahri, M., 2017, Hydrothermal systems in the salt domes of south Iran: *Procedia Earth and Planetary Science*, v. 17, p. 913–916. <https://doi.org/10.1016/j.proeps.2017.01.016>.
- Nabavi, M.H., 1976, An introduction to geology of Iran: *Geological Survey & Mineral Explorations of Iran (GSI)*, 109 p.
- Neal, C., and Kirchner, J.W., 2000, Sodium and chloride levels in rainfall, mist, streamwater and groundwater at the Plynlimon catchments, mid-Wales: interferences on hydrological and chemical controls: *Hydrology and Earth System Sciences*, v. 4, no. 2, p. 295–310. <https://doi.org/10.5194/hess-4-295-2000>
- Parkhurst, D.L., and Appelo, C.A.J., 2013, Description of Input and Examples for PHREEQC (Version 3) – A Computer Program for Speciation, Batch-Reaction, One-Dimensional Transport, and Inverse Geochemical Calculations, U.S. Geological Survey Techniques and Methods, Book 6, Chapter A43, 497 p. <https://doi.org/10.3133/tm6A43>.

- Phillips, J.D., 2005, Weathering instability and landscape evolution: *Geomorphology*, v. 67, no. 1-2, p. 255–272. <https://doi.org/10.1016/j.geomorph.2004.06.012>.
- Plan, L., 2005, Factors controlling carbonate dissolution rates quantified in a field test in the Austrian Alps: *Geomorphology*, v. 68, no. 3-4, p. 201–212. <https://doi.org/10.1016/j.geomorph.2004.11.014>.
- Pulina, M., 1974, Denudacja chemiczna na obszarach krasu węglanowego [Chemical denudation in areas of carbonate karst]: *Prace geograficzne IG PAN NR 105*, p. 1–159.
- Pulina, M., 1977, Zjawiska krasowe w Sudetach Polskich [Karst phenomena in the Polish Sudety Mountains]: *Dokumentacja Geograficzna PAN*, fasc. 2-3, p. 1–118.
- Pulina, M., Krawczyk, W., and Pereyma, J., 1984, Water balance and chemical denudation in the unglaciated Fuglebert basin (SW Spitspergen): *Polish Polar Research*, v. 5, no. 3-4, p. 183–205.
- Raeisi, E., 2004, Iran, *in* Gunn, J., ed., *Encyclopedia of Cave and Karst Science*, Fitzroy Dearborn, New York, p. 992–995.
- Ryb, U., Matmon, A., Erel, Y., Haviv, I., Benedetti, L., and Hidy, A.J., 2014, Styles and rates of long-term denudation in carbonate terrains under a Mediterranean to hyper-arid climatic gradient: *Earth and Planetary Science Letters*, v. 406, p. 142–152. <https://doi.org/10.1016/j.epsl.2014.09.008>.
- Rzonca, B., and Buczynski, S., 2013, Intense karst denudation in a crystalline basin with a small share of carbonate rocks (Sudety Mountains, SW Poland): *Catena*, v. 107, p. 154–164. <https://doi.org/10.1016/j.catena.2013.03.003>.
- Sadeghi, S.H.R., Mizuyama, T., Singh, J.K., and Tofighi, B., 2009, Applicability of Instantaneous Unit Sediment Graph Model in an Iranian Large Watershed: *International Journal of Ecological Economics and Statistics*, v. 13, no. 9, 30–45.
- Sadeghi, S.H.R., and Saeidi, P., 2010, Reliability of Sediment Rating Curves for a Deciduous Forest Watershed in Iran: *Hydrological Sciences Journal*, v. 55, no. 5, 821–831. <https://doi.org/10.1080/02626667.2010.489797>.
- Schoeller, H., 1977, *Geochemistry of Groundwater*, *in* Brown, R.H. et al., eds., *Groundwater Studies—An International Guide for Research and Practice*, UNESCO, Paris, p. 1–18.
- Smith, D.I., and Atkinson, T.C., 1976, Processes, landforms and climate in limestone regions, *in* Derbyshire, E., ed., *Geomorphology and Climate*, John Wiley, London, p. 367–409.
- Stokes, T., Griffiths, P., and Ramsey, C., 2010, Karst Geomorphology, Hydrology and Management, *in* Pike, R.G. et al., eds., *Compendium of Forest Hydrology and Geomorphology in British Columbia*, Land Management Handbook 66, BC Government and FORREX, Government Publications Services, Victoria, p. 373–400.
- Thimonier, A., Schmitt, M., Waldner, P., and Schleppe, P., 2008, Seasonality of the Na/Cl ratio in precipitation and implications of canopy leaching in validating chemical analyses of throughfall samples: *Atmospheric Environment*, v. 42, no. 40, p. 9106–9117. <https://doi.org/10.1016/j.atmosenv.2008.09.007>.
- Viles, H.A., 2012, Linking weathering and rock slope instability: nonlinear perspectives: *Earth Surface Processes and Landforms*, v. 38, no. 1, p. 62–70. <https://doi.org/10.1002/esp.3294>.
- White, W.B., 2000, Dissolution of limestone from field observations, *in* Klimchouk, A.B. et al., eds. *Speleogenesis and Evolution of Karst Aquifers*, National Speleological Society, Huntsville, p. 149–155.

PHYSICAL AND ANALYTICAL MODELING OF RHYTHMIC KARST SPRINGS

Xianxuan Xiao^{1,c} and Qiang Zhang¹

Abstract

Rhythmic Karst Springs (RKSs) are rare geologic features that rhythmically outflow water. A mechanical model for the rhythmic flow with rhythmic spill-over configuration was constructed in this work. The evolution of the RKS was revealed by using geological process analysis. The analytical model can directly explain the existence of RKSs in soluble rock regions and their formation mechanism in nature. Visual observations and flow measurements were performed using a laboratory physical model of RKS. The physical model components included a soluble rock simulation area, karst pipes, cave-reservoir, karst depression terrain, water tank, rhythmic spring, and the outflow measurement system. Groups of tests were carried out to recreate the process of RKS functioning and to confirm the rhythmic cycle duration and the threshold of replenishment intensity. This research helped to interpret the behavior of rhythmic springs using the recharge and evacuation of the subsurface cave-reservoir by means of fluid mechanics and groundwater hydraulics theories.

INTRODUCTION

Rhythmic Karst Springs (RKSs) have intrigued scientists for centuries (Cvijić, 1896; Marković, 1963; Gavrilović, 1967; Petrović, 1981; Bonacci and Bojanić 1991; Mirković and Miljković, 2006; Kolda et al., 2019), and they are named in different ways in the previous works, such as ebb and flow springs, potajnice, and rhythmic springs (Bonacci and Bojanić, 1991). They are regarded as an extremely special kind of spring, which are rare but are distributed all over the world. According to past studies, rhythmic springs (RSs) appear exclusively in areas consisting of soluble rocks. Soluble rocks are those that dissolve in water, leaving almost no residue. Atkinson (1986) described the formation of rhythmic springs. The dissolution of rocks tends to widen the fissures by weathering without blocking them at the same time, allowing groundwater to penetrate and expanding them further.

The RKSs represent an interesting phenomenon that occurs relatively rarely (Bonacci and Bojanić, 1991). The flow of most RKSs is normally not plenty, and it possibly has no critical influence on water source evaluation or regional hydrogeological calculation. An ebb and flow spring, Laywell Spring, is located in a famous landmark of Brixham, Devon, UK (Oliver, 1693). A scheme of interacting reservoirs and syphons was proposed to explain the workings of Laywell Spring (Atwell, 1732). The Laywell occurs at the junction of Middle Devonian limestones and mudstones about 36 meters above mean sea level. It works at 9 to 20 cycles per hour and it is interrupted by periods of varying length or at irregular times. Laywell was once used for public water supply but its use ceased around 1840 by the local load works or through mining and quarrying of limestones (Mather, 2013). RKSs play an important role in nature tourism by developing the tourism industry and enhancing the local economic effect in karst regions. There are about ten rhythmic springs in the USA and six rhythmic springs in France (Bögli, 1960). Gavrilović and Gavrilović (1985) refer to the appearance of about 20 rhythmic karst springs in the karst region of former Yugoslavia. These authors indicated that it is impossible to judge whether the outflows of these springs are real rhythmic springs or not. They also stated that there are more than 33 rhythmic springs in the world, apart from those in the former Yugoslavia: three in Hungary, seven in France, at least eight in China, two each in Bulgaria, Romania, Switzerland, England, and Belgium, and only one each in the former Czechoslovakia, Germany, USA, the Soviet Union, and Israel (Bonacci and Bojanić, 1991).

One-third of the national land area is covered by soluble rocks in China, about 0.91 million square kilometers. Especially in south China, there are various kinds of soluble rocks such as limestone, dolomites, salt rock, and gypsum that are distributed in the Middle Triassic system (mainly dolomites), Lower Permian system (limestone), Ordovician system (mainly limestone), and Lower Sinian system (mainly dolomites). The high karstification terrains typically have strong tectonic movement, deep-cutting valleys, relatively pure soluble rocks, and abundant rains, which generate karstification phenomenon with dissolution cracks, karst caves, stalactites and stalagmites, karst dissolution pipeline, and even subsurface hidden rivers. Therefore, some rhythmic springs must undoubtedly exist. So far, eight rhythmic springs have been revealed in China. Other ones are only reported by mass media or newspapers in the tourism industry.

An interpretation for rhythmic springs functioning by siphon systems was proposed (Katzer 1909; Lazarević, 1990; 2000). Bonacci (1987) presented the schematics of the functioning mode of RKS. His work stated that all the water in the cave-reservoir will outflow suddenly once the water level reaches a siphon water level. When the water level is much higher than the siphon water level, the total flow of the water recharge from underground channel (karst pipes) or

¹ State Key Laboratory of Geohazard Prevention and Geoenvironment Protection, Chengdu University of Technology, Chengdu 610059, Sichuan, China.

^c Corresponding author: xiaoxianxuan2012@cdut.edu.cn; ORCID: 0000-0003-1366-620X

cracks exceeds the maximum capacity of the siphon. Then, the outflows of the spring will maintain the stream all the time. Bögli (1980) explained the possibility of the RKS functioning in four situations, which includes the length of the rhythmic period, the air action, water recharge capacity from the surrounding crack and karst pipe of the basin reservoir. These aspects result in variation of water level in the basin for rhythmic action.

Researchers prefer the term rhythmic springs to the term intermittent springs for emphasizing the siphon action that induces the effect of rhythmic phenomenon in the outflow hydrographs. A classification of rhythmic springs was proposed as follows (Gavrilović, 1967): (1) permanent rhythmic springs; (2) seasonal rhythmic springs; (3) rhythmic springs occurring during the rainy season or the dry season; (4) sudden rhythmic springs. This last kind of spring probably has a great number of groundwater reservoirs either connected in series or in parallel, which was found in the former Yugoslavia. Such a shape was defined as the Kojin Spring hydrograph (Bonacci and Bojanić, 1991).

Previous studies on rhythmic springs mostly focus on the qualitative analyses, siphon process description (Katzner, 1909; Casteleyn, 1977; Bonacci, 1987), and classification of the rhythmic springs (Gavrilović, 1967). However, some aspects involving quantitative evaluation such as mathematical models and physical simulation models of rhythmic springs remain extremely scarce. It is important to indicate the whole-formation geological process and to reveal the genetic mechanism and its evolution characteristics. In this work, a physical model was proposed for the simulation of a rhythmic spring. The main objectives of this study were to evaluate how these cavities, dissolution pipeline geometries, and several chambers work together and function as a rhythmic spring, and to interpret the hydraulic and morphological aspects of the rhythmic springs, as well as how they evolve over time by groups of tests and analysis.

MATERIALS AND METHODS

The goal of this research is to reveal the main variables/factors involved in the RKS system and their effects on the RKS. Based on field work of previous studies, it is worthwhile to investigate and reveal the characteristics of RKS, which can help to better understand its mechanism. The approaches include analytical modeling, physical model construction, and tests for the quantitative analysis of RKS.

RHYTHMIC SPRINGS MEASUREMENT IN THE FIELD

Until now, real-time monitoring and measurements of rhythmic springs are rare. Table 1 gives the details for six rhythmic springs in China and one in Serbia, including the discharge of the rhythmic springs and the periods. The testing time of the rhythmic springs in China was around the 1970s. The Homoljska Potajnica spring in Serbia was measured in July 2012.

Homoljska Potajnica is one of the three known rhythmic springs in Serbia. It is located in eastern Serbia, on the southern slopes of Mt. Homoljske Planine and in the Valja Mori river valley which belongs to the Mlava river basin (Igračev, 2014). Igračev (2014) took two precise measurements of the Homoljska Potajnica spring showed similar shape, durations, and water discharges (Fig. 1). The analysis of the water hydrograph shows that it increased linearly after the discharge occurred and reached its maximum value ($2.8 \text{ dm}^3 \text{ s}^{-1}$), and decreased irregularly after the peak in an instant. Two consecutive discharges are almost the same. The difference between them can be a result of limitations of the measurement process itself by the continuous monitoring under relatively dark conditions due to the weather (Igračev, 2014). This example confirms the periodic eruption and the siphon effect which impacted on the discharge of Homoljska Potajnica. It would be interesting to perform further quantitative research by physical model experiments and analytical modeling.

EXPERIMENTAL SET UP

Geological Conceptual Model for Physical Modeling

The generation process and geological evolution of RKS in karst terrains are illustrated in Fig. 2. Under the influence of tectonic action, shear joints are commonly developed and exist in the soluble rocks in these regions. A hole was

Table 1. Some of the measured rhythmic springs in karst regions. For the rhythmic springs in China, the testing time of discharge and periods was around the 1970s.

Name of RKS	Country / Region	Discharge (dm^3/s)	Period (min)	Testing time
No. 1 Hongbanqiao (HBQ-1)	Guizhou, China	88.55~0.45	33~41	Before 1979
No. 2 Hongbanqiao (HBQ-2)	Guizhou, China	28.5~0.24	33~41	Before 1979
Baihua (BH)	Guizhou, China	3.5~1.5	10~15	Before 1979
Cichong (CC)	Guizhou, China	108.86~43.75	480	Before 1979
Xianglongdong (XLD)	Guizhou, China	139~1.0	29	Before 1979
Huangnidong (HND)	Chongqing, China	500~50	20	1969~1970
Homoljska Potajnica (HP)	Serbia	2.8~0.016	81	July 2012

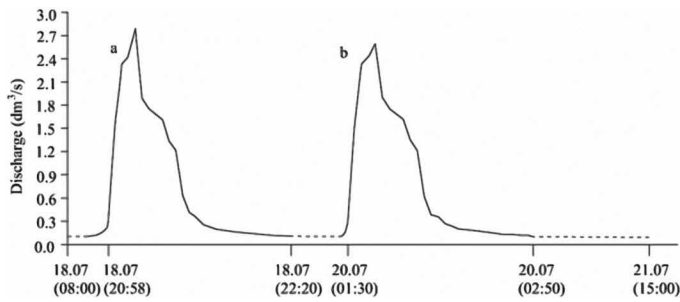


Figure. 1 Discharge hydrography of Homoljska Potajnica on July 18th (a) and 20th (b) in 2012 by field measurement. Two precise measurements showed similar results. Although the final model of Homoljska Potajnica activity cannot be determined, it can be assumed that in extremely arid period, as was the summer 2012, Potajnica was probably in a relatively stable status. The main features (duration of water eruptions, discharged water amount) are almost equal for the two cycles, while the stopping time is related to the time delay from the arid climate (Igračev, 2014).

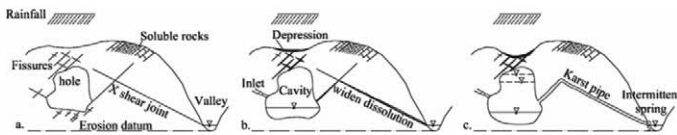


Figure. 2 The geological background of a rhythmic karst spring conformation. (a) cave prototype formation stage, fissures around a dissolved hole in the soluble rocks; (b) the hole receives replenishment and expands as the cavity fills with water. The surface evolves into a depression by rainfall, the karst pipe and fissures offer channels for the streams; (c) the major fissure evolves into a karst pipe by continuous widening dissolution, and the rhythmic spring is formed.

formed by the broken blocks and the long-term weathering and dissolution of many fissures around the hole that formed the channels for the infiltration of precipitation. A valley was generated by abundant rainfall that created geological defect and crustal uplift movement simultaneously. Such a valley is considered as the erosion datum (Fig. 2a). Subsequently, with the long-term dissolution, the hole evolved into a cavity, fissures on the upside of cavity dissolved and provided a dominant way for the rainfall water infiltration, and the karst depression was formed. A karst pipeline appeared on one side of the cavity, the X-shaped shear fissure was dissolved by running water and widened in the downward direction and the main pipe prototype was generated (Fig. 2b). The persistent dissolution induced enlargement of the cavity. Thus, the karst pipe formed and the outlet was placed on the left side of the valley (Fig. 2c). The karst depression on the top of the cavity evolved into a wider and deeper one, and it was covered with the alluvium which gathered the mud and sand gravel to the center of the depression by washing out water on the surface. It is now possible to understand the functioning of the rhythmic karst spring. First, the water table in the cavity can rise because of the vertical and lateral recharge. When the water level reaches the bottom of the pipe inflection point, water can overflow from the cavity and the spring is no longer dry, but presents a bit of flow at the outlet location. With the consistent rise in water level, the water level reached the top of the pipe inflection point. Consequently, siphon action developed, and air in the karst pipe was washed away and it was fully filled with

water. The total flow of the spring reached the maximum value and decreased instantaneously. The decreased water level supplied a lower water head pressure with siphon effect, resulting in the attenuation of total flow of the spring. After the water level decreased to the connection point of the cavity and the karst pipe, air passed through the karst pipe and the siphon disappeared. Thus, the flow at the outlet was equal to zero. The continuous flow into the cavity without discharge caused the water level to increase again, and RKS to run periodically (Fig. 2c).

The Laboratory Physical Model

The goal of using a laboratory model of rhythmic karst spring is to simulate the evolution of the processes, to represent the rhythmic spring function, and to define the cycle duration. The laboratory model of rhythmic karst spring contains three primary components: 1) a physical subsurface karst stratum that contains a single large cavity and a small diameter, inverted U-shaped pipe that is open to the atmosphere at the lower end and an air layer at the bend of the U; 2) a water supply system consisting of a constant head tank, a low power water pump, and a water tank at the bottom; 3) a flow measurement system, which includes a water table ruler and triangular weir plate. The laboratory model is made of acrylic plastic and the water tank is made of 15 mm thick PVC tubing. A square metal rod was used to stiffen the physical model and increase its strength. The conduit was a cylinder and the diameter was selected to be large enough so that the effects of surface tension of fluid can be neglected. The diameter of the reservoir was chosen to be large relative to the diameter of the U-shaped conduit and the physical model, as is likely the case in the natural outlet of an RKS (Fig. 3).

Flow flux is the main parameter that was measured in all the tests. The triangular weir was used to monitor the real time flux of water, by measuring the water relative elevation with the water table ruler. The initial elevation relative to the weir is H_0 , $H_0 = 9.0$ cm. Whenever the water flows through the triangular weir, the elevation of the water table can be measured at each moment and is noted as H_1 . Thus, the flow of water can be calculated as $Q = 5mh^{5/2}$, where $h = H_1 - H_0$; m is the flow coefficient, Q is the flow;

$$m = 1354 + \frac{4}{h} + (140 + \frac{200}{\sqrt{D}}) (\frac{h}{B} - 0.09)^2$$

where D is the distance from the underside of the weir box to the lowest point of the weir opening, $D = 0.1 \sim 0.75$ meters; B is the width of weir box, $B = 0.1 \sim 0.5$ meters.

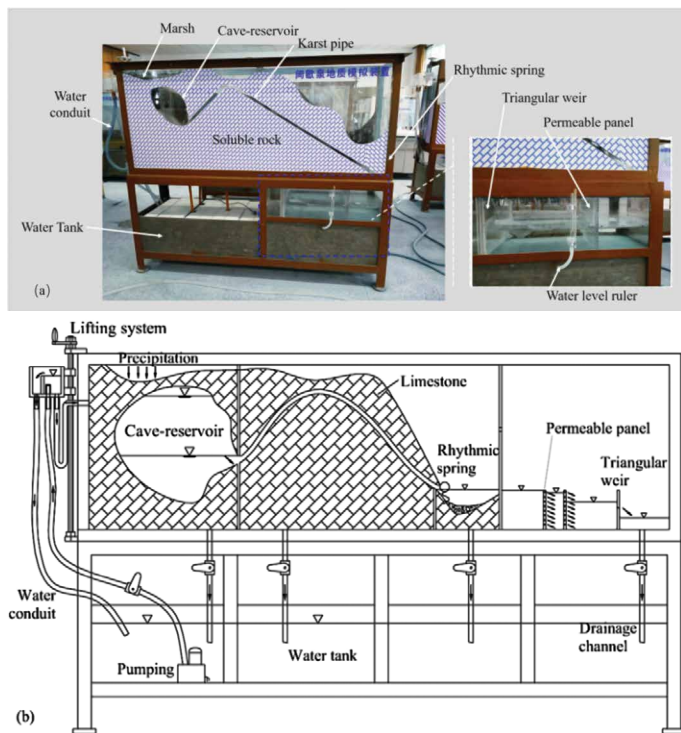


Figure 3. The physical laboratory model of the RS: (a) photo of the physical model of the RS, which includes a cavity reservoir in the soluble rocks; a karst pipe in the soluble rock that developed from a group of shear joints superficial transformation, RS; soil was on the top of the cave-reservoir, the water supply system and the triangle weir flow measurement system and (b) the schematic of the physical laboratory model and water circulation of the simulated specific karst system.

For each experimental run, water was first filled up to two-thirds volume in the tank ensure enough water in the process of each test. The water pump introduces the water from the tank to one side of the stable water flow box through the plastic water hose. The remaining water flows to another side of the stable water flow box and downwards to the water tank by another plastic hose as the water in the stable water flow box is fully filled. Then, most of the water in the stable flow box flows to the gaping depression that is set on the top of the physical model. Subsequently, the water infiltrates into the cavity through the simulated vertical fissures and the water table in the cavity rises up. The water level in the karst pipe remains the same as the cavity because of their connectivity. Water in the cavity cannot flow out from the karst pipe until the water level is higher than the lower critical point of the karst pipe turning. Once water flows out, the water level in the cave-reservoir is recorded as H_1 . The Siphon effect appears when the water level in the cavity exceeds the upper critical point. Once the siphon effect is generated, the water level in the cave-reservoir is recorded as H_2 . Then, the water level declines and a stream of water flows from the outlet of the spring; the flow attenuates gradually and is equal to zero instantaneously; the cavity receives recharge from the top and the water level increases again; and the siphon re-plays again. The triangular weir system allows perfect flow measurement for the entire test process.

Testing Approach and the Tests Setup

The replenishment and the volume of the cave-reservoir have an important effect on the rate of water level

rise in the cave-reservoir as well as the cycle duration. However, the relationship between the replenishment of the cave-reservoir and the cycle duration is still unknown, such as the hydraulic boundaries of the RKS within which the hydrograph appears different and the maximum and minimum flow of the RKS. In this regard, it would be useful to reveal the influencing factors of the flow and the cycle duration for water management, sustainable development and utilization in karst terrain.

Eight tests were carried out by using the physical model, including different water replenishment values of the cave-reservoir and different volumes of the cave-reservoir. The device structure and the initial experimental conditions are given in Table 2.

Table 2 There are two types of cave-reservoirs which are distinguished by size (A represents one-third of the maximum size of the cave-reservoir, A + B represents the maximum size of the cave-reservoir). The elevation of the outlet of the RS equals 0. Scheduled number of cycles in A + B is less than A, enough for the cycle duration comparison.

Test Number	Cave-Reservoir Type	Scheduled Number of Cycles
1	A	10
2	A	10
3	A	12
4	A	11
5	A	10
6	A + B	2
7	A	12
8	A + B	2

Notes:
 Elevation of the key points in the analog karst system: $h_1 = 77$ cm, $h_2 = 71$ cm, $h_3 = 37.6$ cm, and $h_4 = 0$ cm.
 Cross-sectional area of the pipe = 3.142 cm².
 Maximum height of reservoir = 35 cm. Maximum width of reservoir = 42 cm.

Each of these tests was conducted as follows. (1) Check the instrument, make sure the water valves are normal and the analog karst pipe is unobstructed; (2) the water in the tank can be introduced by the pump after power on; the water replenishment is controlled by the water table controller on the left side of the model by rotating the lifting system in clockwise or counterclockwise direction, and the elevation of the water table controller represents the intensity of water replenishment; (3) measure the initial weir elevation at the downward side of the model, once the outlet of the RS is flowing; measure the water head on weir one time per second until the water head equals the initial weir elevation. In the process of testing, observation, photographs, and recorded data are needed.

From Test 1 to Test 4, the volume of the cave-reservoir was constant and the water replenishment increased step by step to obtain the changes in maximum flow, minimum flow, and the cycle duration. Test 5 and Test 6, and Test 7 and Test 8 were considered as two groups. The water replenishment was constant but the volume of the cave-reservoir was different in each group.

Analyses of Hydrological Condition

The siphon effect is the main factor that induces RKS. The fluid movement from the cave reservoir to the outlet follows the law of Newton inner friction, momentum and energy conservation law. The Bernoulli energy conservation equation was used to describe the fluid movement

$$z_1 + \frac{P_1}{\gamma} + \frac{\alpha V_1^2}{2g} = z_2 + \frac{P_2}{\gamma} + \frac{\alpha V_2^2}{2g} + h_w, \quad (1)$$

where z_1 is the elevation head; $\frac{P}{\gamma}$ is the pressure head; $\frac{\alpha V^2}{2g}$ is the velocity head; V is the water flow velocity in the karst pipe of the physical model; h_w is the head loss, which represents the energy lost during the water stream; α is the kinetic energy correction factor, for running water, $\alpha \approx 1$; $z + \frac{P}{\gamma}$ is the piezometric water level; $\gamma = \rho g$ is the test weight of water, ρ is the density of water, and g is the acceleration of gravity.

Applying the following assumptions: (1) the water in the experiments is considered as an ideal and incompressible fluid; (2) the flow is a steady flow; (3) gravity is the only mass force in the experiments and (4) particles flow along a specific streamline h_w is equal to zero to Equation (1) resulted in

$$z + \frac{P}{\gamma} + \frac{\alpha V^2}{2g} = C, \quad (2)$$

where C is a constant that represents the total mechanical energy of the fluid.

The water flow velocity in the karst pipe was calculated by

$$\begin{cases} Q = V_1 A_{21} = V_2 A_{22}, \\ A_2 = \frac{\pi d^2}{4}, \end{cases} \quad (3)$$

where Q is the flow in the karst pipe; A_{21} , A_{22} represent upstream and downstream arbitrary cross-sectional areas of the karst pipe, respectively; and d is the diameter of the karst pipe.

RESULTS

This work investigated the RKSs functioning and process by analytical modeling and a group of tests based on the physical model. The water flow velocity of the RKS, the flow of the RKS, the negative pressure at the siphon water level, and the cycle duration were derived. The results of the model tests include two main categories of rhythmic phenomena (rhythmic flow and cut-off, rhythmic flow and uncut) and the impact of variable volume of the cave-reservoir on the hydrographs.

Analytical Model

The karst pipe is smooth and even, and its diameter is constant. The water flow velocity at the RKS outlet and the negative pressure at the siphon level can be calculated.

It was postulated that the water level in the cave-reservoir h_1 is unchanged temporarily (Fig. 4), considering the outlet of rhythmic spring as the datum plane ($h_4 = 0$), from h_1 to h_1 . Then, the Bernoulli equation was established as:

$$z_1 + \frac{P_1}{\gamma} + \frac{V_1^2}{2g} = z_4 + \frac{P_4}{\gamma} + \frac{V_4^2}{2g}, \quad (4)$$

where $V_1 \approx 0$, compared to V_4 ; $p_1 = p_4 = p_a$, p_a is the atmosphere pressure. Equation (4) can be simplified to $z_1 = z_4 + \frac{V_4^2}{2g}$; $z_1 = h_1$, $z_4 = h_4 = 0$. Hence, the water flow velocity at the RKS outlet can be calculated as:

$$V_4 = \sqrt{2hg_1}. \quad (5)$$

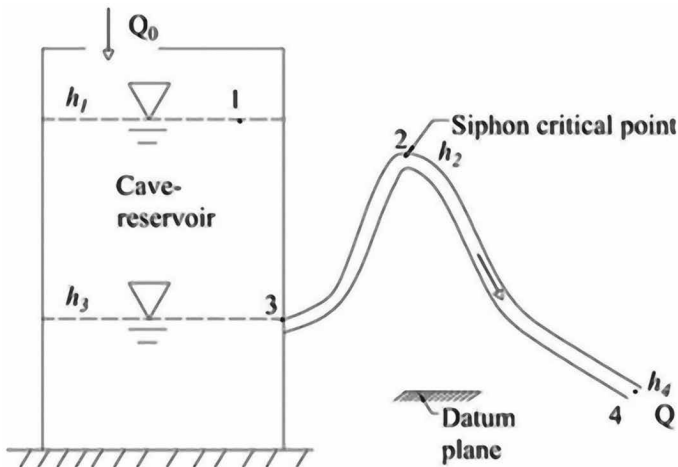


Figure 4 Simplified hydrograph of rhythmic spring action.

The flow of the RKS can be calculated using the following formula:

$$Q = \frac{\pi d^2}{4} \sqrt{2hg_1}, \quad (6)$$

Equation (5) indicates the relationship between the water flow velocity at the RKS outlet and the water level in the cave-reservoir. Before the siphon action, the water level in the cave-reservoir rises up due to the water infiltrating from the depression, which can accumulate water during precipitation or by the recharge from karst pipe streams. If the water level in the cave-reservoir reaches the crucial water level h_1 , the siphon effect yields and the water level in cave-reservoir declines below the crucial water level h_1 . A reduced water level in the cave-reservoir induces the decrease in water flow velocity at the RKS outlet.

The negative pressure at the siphon level is $p_r = p_2 - p_a$. From h_1 to h_2 , the Bernoulli equation can be expressed as:

$$z_1 + \frac{p_1}{\gamma} + \frac{V_1^2}{2g} = z_2 + \frac{p_2}{\gamma} + \frac{V_2^2}{2g}, \quad (7)$$

where $V_1 \approx 0$, compared to V_4 ; $p_1 = p_a$. According to Equation (3), $\bar{V}_2 A_{22} = \bar{V}_4 A_{24}$ can be obtained by using continuity fluid equation from h_2 to h_4 . Since $A_{22} A_{24}$, $\bar{V}_2 \bar{V}_4$. As the water flow velocity at the RKS outlet cross-section is evenly distributed, $\bar{V}_4 = \bar{V}_4$. Then, Equation (7) can be simplified to $\frac{p_2}{\gamma} = (z_1 - z_2) + \frac{p_1}{\gamma} - \frac{V_2^2}{2g}$ where $p_1 = p_a$. Hence, the negative pressure at the siphon level position is derived as follows:

$$P_r = \gamma \left[(h_1 - h_2 - \frac{(\sqrt{2hg_1})^2}{2g}) \right] = -\rho gh_2, \quad (8)$$

Equation (8) indicates that the negative pressure at the siphon level (siphon critical point) depends on the elevation from siphon crucial point to the outlet of RKS (h_2). Here, h_2 is a constant parameter which depends on the structure of the designed device or the natural formation karst system.

According to Equation (5), the water flow velocity at the RKS outlet V_4 depends on the water level of the cave-reservoir h_1 . In fact, the water level in the cave-reservoir changes all the time, which induces the change in water flow velocity at the RKS outlet V_4 . On the other hand, the change in V_4 has an influence on the water level in the cave-reservoir. The decrease in V_4 leads to reduction of the flow of RKS. It is interesting to understand how the water level changes with time in the cave-reservoir. Suppose that the replenishment Q_0 is a constant parameter (the recharge from precipitation or the karst pipe, soluble cracks), the cave-reservoir is a regular cylinder, and its bottom area is A_1 , the karst pipe is even and its cross-sectional area is A_2 , and both A_1 and A_2 are constant. The following points explain the boundary conditions of the water-level declining with time:

1. First, h_1 increased linearly due to the recharge of the stable infiltrate flow Q_0 , because the bottom area of the cylinder was fixed, and there was no flow at the outlet of RKS.

2. The siphon effect started as soon as the water level rose to the maximum value of h_1 (Fig. 6, point 1). Subsequently, both the water flow velocity at the RKS outlet V_4 and the flow of RKS Q reached the maximum value, and $Q > Q_0$.

3. $Q > Q_0$ induced the decrease in water level in the cave-reservoir. Subsequently, the lower water level in the cave-reservoir caused the reduction of both the water flow velocity at the outlet and the flow of RKS. The interaction of the water level and the flow of RKS caused the siphon effect to disappear and the break of water flow. With the

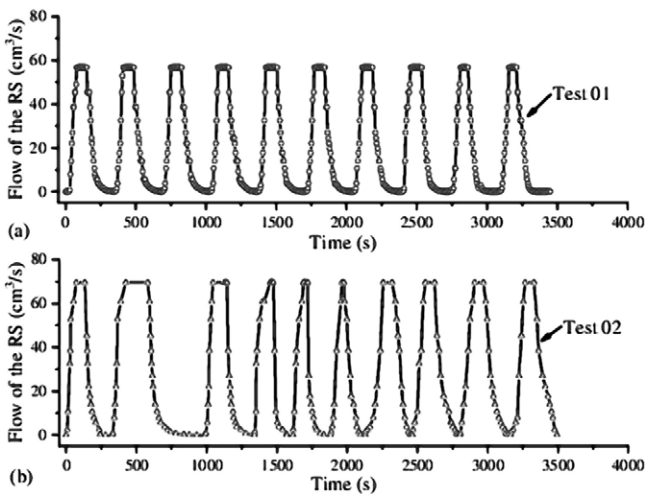


Figure 5. Relationship between flow of RKS and time in Tests 01~02: (a) the replenishment into the cave-reservoir had lower value and flow of the RKS changed regularly with time. There were 10 cycles in this test and the cycle duration was evenly distributed and (b) the replenishment into the cave-reservoir had lower value but the cycles were not evenly distributed.

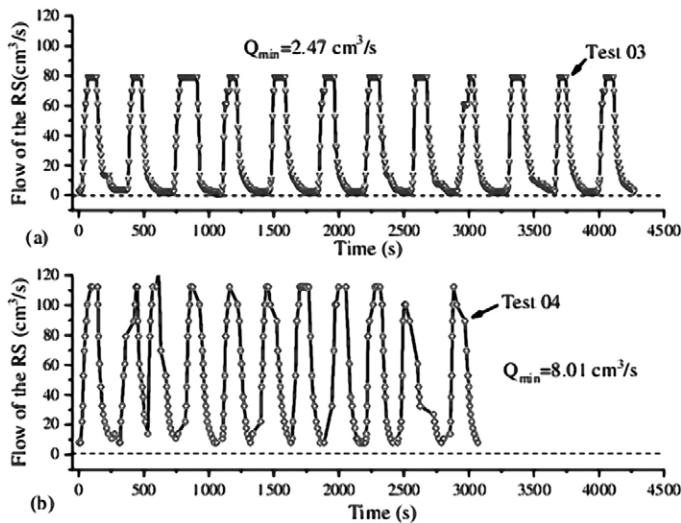


Figure 6 Relationship between flow of RKS and time in Tests 03–04: (a) flow of the RKS evolving regularly with time, the increase in replenishment induced a low limit flow of the RKS and (b) a large replenishment of the cave-reservoir caused irregular changes in flow of the RKS with time, and more cycles appeared in the same duration.

continuous infiltration and recharge from the top of the cave-reservoir, the second process of RKS functioning was formed and replayed.

The change in water level in the cave-reservoir with time can be expressed as:

$$h_1(t) = \begin{cases} \frac{Q_0 t}{A_1}, & 0 < t < t_{cr} \\ \Delta h_{max}, & t = t_{cr} \\ \frac{(Q - Q_0)^t}{A_1}, & t_{cr} < t < T \end{cases} \quad (9)$$

In Equation (9), t_{cr} is the moment when the water level reaches the siphon critical point; T is the cycle duration; Δh_{max} is the maximum value of the water level in the cave-reservoir, $\Delta h = h_1 - h_3$. According to Equation (6) and Equation (9), when $t_{cr} < t < T$, the function $h_1(t)$ can be expressed as $h_1(t)A_1 = A_2 t \sqrt{2gh_1(t)} - Q_0 t$. Then, it can be simplified to

$$t = \frac{A_1 h_1(t)}{A_2 \sqrt{2gh_1(t)} - Q_0}, \quad (10)$$

which forces $h_1(t)$ to change from Δh_{max} to 0 after the siphon effect starts. The cycle duration T is the sum of the time of water increasing and water decreasing.

$$T = \frac{A_1 \Delta h_{max}}{Q_0} + \int_{\Delta h_{max}}^0 \frac{A_1 h_1(t) dh_1(t)}{A_2 \sqrt{2gh_1(t)} - Q_0}. \quad (11)$$

Through the definite integral of Equation (11), the cycle duration was derived

$$T = A_1 \Delta h_{max} \left(\frac{1}{Q_0} - \frac{3Q_0}{2gA_2^2} \right) + \frac{A_1}{A_2} \left(\frac{\Delta h_{max}^{5/2}}{3\sqrt{g}} + \frac{6Q_0^2 \sqrt{2gh_{max}} - \ln \sqrt{2g\Delta h_{max}}}{2A_2^2 g} \right). \quad (12)$$

Equation (12) indicates that the cycle duration depends on A_1, A_2, Q_0 and Δh_{max} .

Dynamic Features of Rhythmic Karst Spring by Physical Model Tests

A total of eight tests were carried out in this study. The results of these tests are presented in Table 3. The tests can be grouped into two categories according to the flow of the RKSs: (1) rhythmic and flow uncut (in Test 3 and Test 4); (2) rhythmic but flow cut-off (the rest of the tests). The results of the tests also show that the evolving feature of the hydrograph changed with the variable volume of cave-reservoir and the replenishment into the cave-reservoir. These

Table 3. Values of variables from the data of the 8 tests. The volume of cave-reservoir is the same in Test 1~Test 5 and Test 7, while Test 6 and Test 8 have the same volume of cave-reservoir.

Test Number	Replenishment by Infiltrating Q_0 ($\text{cm}^3 \text{s}^{-1}$)	Volume of Cave-Reservoir V_R (cm^3)	Max. Flow of the RS Q_{max} ($\text{cm}^3 \text{s}^{-1}$)	Min. Flow of the RS Q_{min} ($\text{cm}^3 \text{s}^{-1}$)	Average Cycle Duration (s)
1	21.70	3973	56.72	0	340
2	28.45	3973	69.67	0	399
3	33.25	3973	79.2	2.47	361
4	57.24	3973	124.93	8.01	273
5	19.80	3973	52.75	0	325
6	19.80	11917	52.75	0	644
7	27.30	3973	65.49	0	339
8	27.30	11917	66.11	0	608

tests were conducted under different water replenishment volumes into the cave-reservoir from Test 01 ~ Test 04, and Test 05, and Test 07. Test 05 and Test 06, Test 07 and Test 08 were considered as two general groups with the same infiltrating flow but different volumes of the cave-reservoir in each group (Table 3). Due to the similar conditions in the two groups, it is not necessary to present all of the hydrographs herein.

Rhythmic and Flow Cut-Off

In Test 01, the replenishment into the cave-reservoir was $21.7 \text{ cm}^3 \text{ s}^{-1}$. Water level rose up linearly in the cave-reservoir and the flow of the RKS (Q) was equal to zero. The flow of the RKS was not equal to zero until the water overflowed to the bottom of the siphon position (Fig. 4, point 2), and then the flow of the RS increased with the continuous rise in water level. The siphon effect acted as soon as the water level in the cave-reservoir reached the highest point, with a maximum value of flow of the RKS. The maximum flow remained for some time and then decreased by the reducing siphon effect, because flow of the RKS was much higher than the recharging flow (Q_0). Water level in the cave-reservoir dropped rapidly first and then slowly. The flow of the RKS attenuated first and slowed later. Moreover, it had a much slower decreasing duration and was equal to zero when the water level dropped to h_3 (Fig. 5a). Subsequently, the flow was cut-off. According to the hydrograph, 10 peaks were generated over the entire test time of 3450 seconds. The average cycle duration was 340 s. The maximum and minimum flow values of the RKS were equal to $56.72 \text{ cm}^3 \text{ s}^{-1}$ and $0 \text{ cm}^3 \text{ s}^{-1}$, respectively. Moreover, the intermittent characteristic was obvious and the cycles were regular.

The replenishment of the cave-reservoir was $28.45 \text{ cm}^3 \text{ s}^{-1}$ in Test 02. It can be easily seen that the hydrograph shape was irregular, and each cycle had a variable duration; sometimes longer, sometimes shorter. The average cycle duration was equal to 399 s, and the maximum and minimum flow values of the RS were equal to $69.67 \text{ cm}^3 \text{ s}^{-1}$ and $0 \text{ cm}^3 \text{ s}^{-1}$, respectively. However, 10 peaks were generated during the entire testing time of 3492 s. Although the siphon effect was the same as in Test 01, the peak values could not maintain a certain period in some of the cycles. Rapid increase and decrease were observed (Fig. 5b) compared with Test 01 and Test 02. We found that the larger the replenishment volume, the greater the maximum flow value of the RKS. The minimum value of flow of the RKS was equal to zero due to the sufficient volume of replenishment received by the cave-reservoir, also because the flow of the RKS was greater and the replenishment was relatively smaller. When the water level in the cave-reservoir dropped to the connection of karst pipe and the cave-reservoir, air bubbles entered the pipe and attenuated the siphon effect from the water surface in the cave-reservoir. Flow of the RKS was eventually cut-off in a cycle duration when the flow rate is zero.

Rhythmic and Flow Uncut

The rhythmic phenomenon still existed in Test 03. The replenishment was equal to $33.25 \text{ cm}^3 \text{ s}^{-1}$. The maximum flow of the RKS was equal to $79.2 \text{ cm}^3 \text{ s}^{-1}$, while the minimum flow of the RKS was equal to $2.47 \text{ cm}^3 \text{ s}^{-1}$ for all the tests. The cycles were regular and the cycle duration was 361 s. There were 12 peaks generated during the entire test period. The peak flow of the RKS was maintained in some of the cycles. However, the minimum flow of the RS lasted a longer time than the maximum ones in each cycle (Fig. 6a). In contrast to Test 01 and Test 02, the minimum flow of the RS was greater than zero and was a constant value in every cycle in Test 03, which indicates that a rhythmic stream was always in the karst pipe throughout the test. Similar to the earlier tests, the greater the replenishment, the greater the peak flow of the RKS. The replenishment was large enough and the volume of the cave-reservoir was constant, so that the flow of RKS was never cut. Once the water level in the cave-reservoir dropped to the connector of joint position (Fig. 4, point 3), only a few air bubbles went into the karst pipe. The sufficient recharge induced the water level in cave-reservoir to rise again and generated the next siphon effect under the condition of a little stream in the karst pipe.

The replenishment into the cave-reservoir was equal to $57.24 \text{ cm}^3 \text{ s}^{-1}$. The maximum and minimum flow values of the RKS were $124.93 \text{ cm}^3 \text{ s}^{-1}$ and $8.01 \text{ cm}^3 \text{ s}^{-1}$, respectively, which clearly shows that the maximum flow of the RKS increased with the increase in replenishment. According to the hydrograph of Test 04 (Fig. 6b), flow of the RKS changed rapidly. It increased fast and reached the peak value in a short time, and then decreased soon, and then increased rapidly again for the next cycle. The cycles were not stable, some of them presented a short cycle while other cycles showed a regularly changing process. The average cycle duration was 273 s. There were 11 cycles in this test, and the total consumed time was equal to 3068 seconds. Similar to Test 03, there was limited volume of the cave-reservoir but abundant water recharge flowed into the cave-reservoir, which caused the flow of the RKS at the trough periods.

Variable Volume of Cave-Reservoir

Test 05 and Test 06 were carried out to ascertain the relationship between the cycle duration and the volume of the cave-reservoir. The volumes of Test 05 and Test 06 were 3973 cm^3 and 11917 cm^3 , respectively. The replenishment was a constant $19.8 \text{ cm}^3 \text{ s}^{-1}$ in the two tests.

In Test 05, the hydrograph shape was similar to the aforementioned tests such as Test 01 and Test 03. The maximum flow and the minimum flow of the RKS were equal to $52.75 \text{ cm}^3/\text{s}$ and $0 \text{ cm}^3 \text{ s}^{-1}$, respectively. Therefore, it can also be regarded as a rhythmic and flow cut-off case, where the regular cycles and the peaks showed the same appearance (Fig. 7a). Its average cycle duration was 325 seconds. In contrast to Test 05, the only difference in Test 06 was the volume of the cave-reservoir. The cycle duration was 644 seconds, which was quite different from the cycle duration in Test 05 (Fig. 7b). However, the maximum flow and the minimum flow of the RKS were the same. This result indicated that the scale of the reservoir formed by the dissolution of soluble rock in karst terrain has an important effect on the cycle duration.

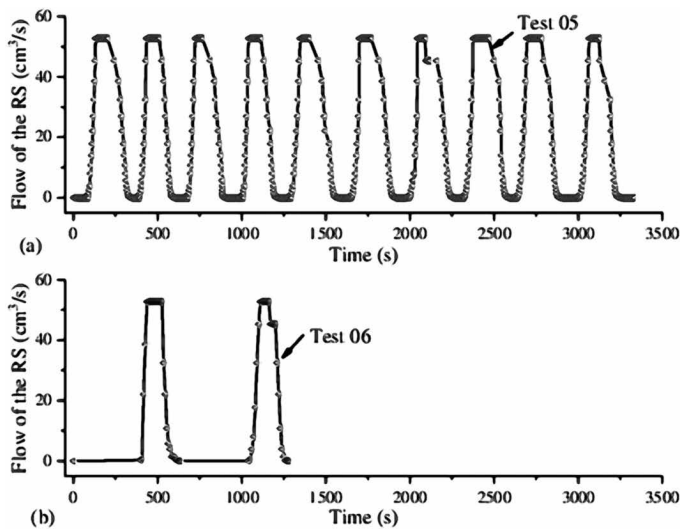


Figure 7 Relationship between flow of RKS and time in Test 05 and Test 06: (a) the volume of cave-reservoir was one-third of Test 06, flow of the RKS changed regularly with time, 10 cycles in the whole test and the average cycle duration was 325 seconds and (b) the volume of cave-reservoir was increased, three times larger than Test 05. The same replenishment and different volumes of cave-reservoir caused a variable cycle duration.

linear interpolation calculation. Additionally, the average cycle duration increased from Test 01 ~ 02, and presented an increasing trend. In contrast, the average cycle duration decreased from Test 02 ~ 04. It can be inferred that the large enough replenishment caused a peak flow of the RKS, and little time was needed to induce the next cycle. The reason for the increasing average cycle duration can be considered as the combined influence of the constant volume of the

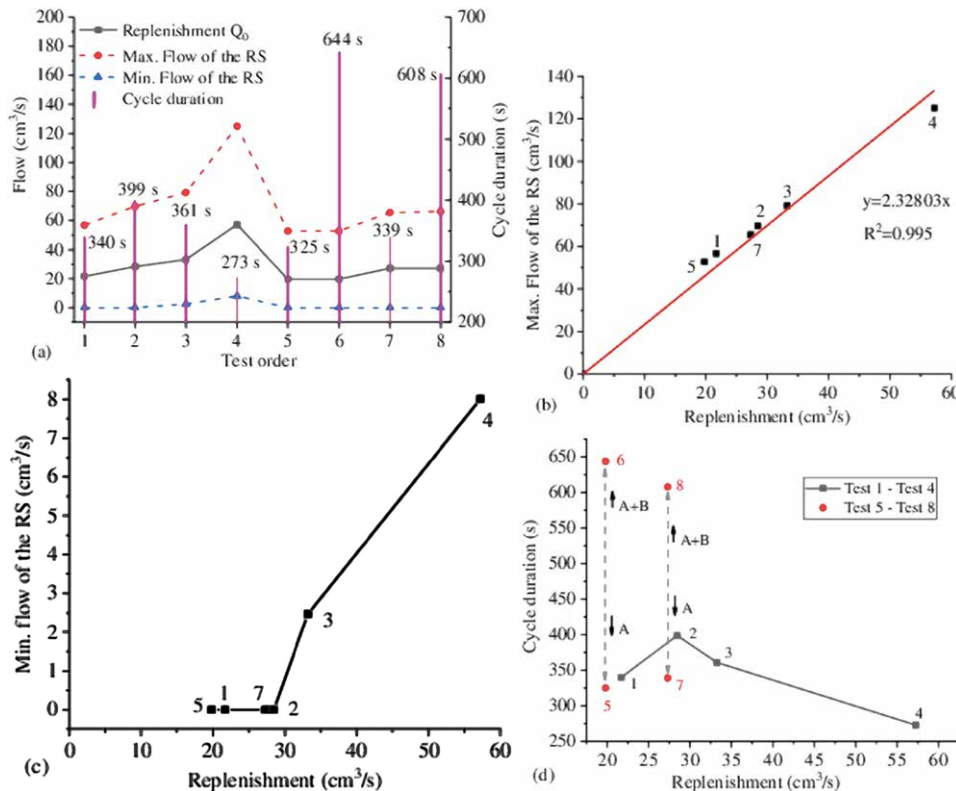


Figure 8 Relationship among the variables: (a) characterization points of the maximum flow of the RKS, minimum flow of the RKS, cycle duration and the replenishment in the experiments; (b) the linear increase between the maximum flow of the RKS and the replenishment; (c) relationship between the min. flow of the RKS and the replenishment, Tests 01 ~ 08; and (d) relationship between cycle duration and replenishment in Tests 01 ~ 08.

Replenishment from the top or the lateral karst pipe into the cave-reservoir depends on the hydrogeological and environmental conditions in the karst terrains. Stable replenishment provides a siphon effect for a unique karst system. The increased replenishment can provide an increase in flow of the RKS with variable cycle duration under different replenishment volumes. Compared with Test 05 and Test 06, the cycle duration of Test 07 and Test 08 increased with the increase in volume of the cave-reservoir under constant replenishment (Fig. 8a). According to the results of Tests 01 ~ 08 (Test 05 was the same as Test 06, Test 07 was the same as Test 08), the maximum flow of the RKS and the replenishment showed linear correlation with a quadratic value of 0.995 (Fig. 8b). However, the minimum flow of the RKS changed in a different way. The minor replenishment in cave-reservoir can induce a siphon effect but the minimum flow was equal to zero periodically. When the replenishment was large enough, the minimum flow was no longer equal to zero, but it was periodic and changed synergistically with the maximum flow (Fig. 8c), indicating that there must exist a critical replenishment value that can be used to distinguish the categories of RKS.

The critical replenishment was around 30.85 cm³/s by linear interpolation calculation. Additionally, the average cycle duration increased from Test 01 ~ 02, and presented an increasing trend. In contrast, the average cycle duration decreased from Test 02 ~ 04. It can be inferred that the large enough replenishment caused a peak flow of the RKS, and little time was needed to induce the next cycle. The reason for the increasing average cycle duration can be considered as the combined influence of the constant volume of the

cave-reservoir, the replenishment, and the maximum flow of the RKS.

The cycle duration increased first, reached a peak value and then decreased with the increase in water replenishment in a constant volume of cave-reservoir (from Tests 05, 01, 07, 02, 03, and 04 one by one, Fig. 8d). Furthermore, for the same replenishment but different volumes of the cave-reservoir, the larger the volume, the longer the obtained duration. The range of cycle duration followed the bulk of cave-reservoir size from A to A + B, and the cycle duration increased to the top or decreased to the bottom.

DISCUSSION

RKS in karst terrains are always related to the siphon effect. The geological process analysis methodology was used to understand the characteristic evolution of this kind of spring, because it is necessary to identify the geological and hydrogeological conditions in the area where rhythmic springs are found. Mathematical

equations were employed to provide solutions for the parameters (e.g., the velocity of the RKS at the outlet, negative pressure at the siphon water level, replenishment for the cave-reservoir, the max. flow and the min. flow of the RKS, etc.). Multiple tests carried out with the physical model that simulates the rhythmic spring functioning in a karst system of soluble rocks including the real-time monitoring of the replenishment of the cave-reservoir, the flow of the RKS, and the cyclic duration. These data illustrated that the change in water replenishment for the cave-reservoir has a crucial impact on the functioning of RKS, including the correlation of the parameters. The difference in fissures, pipes, cavities, and the hydrology also induced variable modes of RKS.

The Calculation of Characteristic Parameters

Water flow velocity at the outlet of the RKS, flow of the RKS, negative pressure at the siphon critical point, and the cycle duration are the main characteristic parameters for describing the process of RKS quantitatively. According to the hydraulic theories, the water flow velocity at the outlet depends on the vertical difference between the water level in cave-reservoir and the outlet. According to Equation (7), the velocity acceleration increased first and decreased later. The higher the water level in the cave-reservoir, the greater the flow velocity at the outlet. The energy loss was neglected in the derivation, which may have an impact on the velocity calculation. In fact, water flow from the cave-reservoir to the outlet passes through the karst pipe, with an inner surface that is irregular and coarse. Hence, the velocity decreased all the time from the connection joint to the outlet. Due to the constant cross-sectional area of the outlet, the water flow velocity at the outlet is proportional to the flow of the RKS.

Negative pressure at the siphon critical point is the main dynamic force for the functioning of RKS. The negative pressure is up to the vertical difference of the siphon critical point to the outlet. It is a fixed value which provides the power directly for the RKS. It can be affected by air bubbles going through the karst pipe and disconnect the stream.

The cycle duration of the RKS can be calculated by Equation (15). Its values depend on the area of the bottom surface A_1 , the cross-sectional area of the karst pipe A_2 , the replenishment of the cave-reservoir Q_0 , and the vertical difference between h_1 and h_2 (Δh_{\max}). The replenishment of the cave-reservoir source consists of infiltration from precipitation, the lateral inflow from the karst pipe, and from cracks and fissures. The replenishment is stable on some days, and the volume of the cave-reservoir and the structure of karst pipe system remain almost constant. The cycle duration always remains relatively invariable.

Replenishment and Flow of the RKS and Cycle Duration

Flow of the RKS changes with the replenishment of cave-reservoir. Maximum and minimum flow of the RKS can be identified in the curves of relationship between flow and time by physical laboratory experiments. The value of replenishment of the cave-reservoir should be within a certain range. For instance, when the value of replenishment is less than the lower limit, all the replenished water outflows to the outlet through the karst pipe, and the water table in the cave-reservoir is stable all the time. Once the replenishment exceeds the upper limit, the spring appears as a normal spring commonly found in nature. The range of replenishment is a necessary condition for the siphon effect of the RKS. Maximum flow of the RKS increases linearly with the replenishment, due to the fixed volume of the cave-reservoir and the uniform karst pipe system. In contrast, the minimum flow of the RKS equals zero. At lower replenishment of the cave-reservoir, the siphon effect occurs. The minimum flow of the RKS exists until there is a large enough replenishment of the cave-reservoir. The presentation of minimum flow of the RKS indicates the distinction between rhythmic flow cut-off and rhythmic flow uncut.

The cycle duration increases with the increase in replenishment at a lower value. The cycle duration decreases when the minimum flow of the RKS is not equal to zero. The limit volume of the cave-reservoir and the increasing discharge from the outlet of the spring are observed. The cycle duration is extended when the volume of the cave-reservoir is increased.

Different Shaped Cave-Reservoirs and Hydrographs

As discussed, the shapes of the cave-reservoirs are different. A kidney-shaped reservoir was assumed in the physical model and a vertical reservoir was assumed in the analytical model. The hydrographs of the RKS depend on changes in flow over time. Flow of the RKS is related to the capability of the siphon effect and the rate of decrease in water level in the reservoir. When the siphon effects of the kidney-shaped reservoir system and the vertical reservoir system are the same, assuming the replenishment are the same, the kidney-shaped reservoir is irregular from the higher water level to the lower position vertically, which induces a varying rate of decrease in water level all the time. Consequently, the hydrograph will have the following features: (1) less time is needed from the initial water level to the siphon water level, and less time is needed from zero to the peak value for the flow. There is shorter duration of the peak value, which decreases faster to the end of the cycle; (2) close to the end of the cycle, at the bottom of the hydrograph, the flow decreases step by step and a smoother curve can be obtained. For the vertical reservoir system, the hydrograph appears smoother both in the ascending phase and the descending phase of the flow, and the peak flow is maintained longer.

CONCLUSIONS

A physical laboratory model was constructed for the RKS that occurs in the karst terrains. Both the mathematical analysis and the physical laboratory tests provided useful quantitative information on the rhythmic springs process and the hydrology parameters. The mathematical analysis provided some crucial parameters including the water flow velocity at the outlet of the RKS, flow of the RKS, negative pressure at the siphon point, and the cycle duration by formula derivation. Tests were performed with a laboratory-scale physical model to simulate the intermittent phenomenon of springs in the karst terrains. The results of the experiments demonstrate that the existence of a siphon effect is key for the functioning of RKS. Moreover, the following relationships between the replenishment and flow of the RKS, and the cycle duration were revealed:

1. The replenishment should be a ranged value. The lower limit and the upper limit are the necessary conditions for a rhythmic spring. The maximum flow of the RKS was proportional to the replenishment of the cave-reservoir, while the minimum flow of the RKS required a large enough replenishment of the cave-reservoir. Less replenishment caused a rhythmic phenomenon without a minimum flow of the RKS. There must exist a critical value of replenishment for the categories of RKS.
2. Cycle duration changed with the change in the replenishment volume. It increased under lower replenishment but decreased with increased replenishment. The cycle duration attenuated once minimum flow of the RKS was no longer equal to zero. The cycle duration was extended when the volume of the cave-reservoir expanded. The hydrographs were different between a kidney-shaped reservoir system and a vertical reservoir system.

ACKNOWLEDGMENTS

We thank all of our colleagues with whom we have discussed rhythmic springs in the field and lab over the past several years and also the associate editor and two anonymous reviewers for their comments. This work was initiated with support from the National Natural Science Foundation of China NSFC Grant (No. 41502244) and was continued with support from Fundamental Research Fund of SKLGP (No. SKLGP2018Z023). These financial supporters are gratefully acknowledged.

REFERENCES

- Atkinson, T.C., 1986, Soluble rock terrains: *in* Fookes, P.G., and Vaughn, P.R eds., A Handbook of Engineering Geomorphology, Chapman & Hall, p. 241-257.
- Atwell, J., 1732, Conjectures upon the nature of intermitting and reciprocating springs: *Philosophical Transactions*, v. 37, p. 301-316.
- Bögli, A., 1980, *Karst Hydrology and Physical Speleology*. Springer Verlag, Berlin, v. xii, 284 p. <https://doi.org/10.1007/978-3-642-67669-7>.
- Bonacci, O., 1987, *Karst Hydrology*. Springer Verlag, Berlin. <https://doi.org/10.1007/978-3-642-83165-2>
- Bonacci, O., and Bojanic D., 1991, Rhythmic karst springs: *Hydrological Sciences Journal*, v. 36, no. 1, p. 35-47. <https://doi.org/10.1080/02626669109492483>.
- Casteleyn, J.A., Van Groen, P. and Kolkran, P.A., 1977, Air entrainment in siphons: Results of tests in two scale models and an attempt at extrapolation: *Delft Hydraulics Laboratory Publ.* no. 187.
- Cvijić, J., 1896, Izvori, tresave i vodopadi u istočnoj Srbiji. *Glasnik srpske kraljevske akademije*, sveska LI, Beograd.
- Gavrilović, D., 1967, Intermitentni izvori u Jugoslaviji (Rhythmic springs in Yugoslavia). *Glasnik Srpskog Geografskog Društva XLVII* (1), p. 13-36.
- Gavrilović, D., and Gavrilović, L. J., 1985, Intermitentni izvor Zaslavnica (Rhythmic spring Zaslavnica): *Glasnik Srpskog Geografskog Društva LXV* (2), p. 35-41.
- Igračev N., 2014, Comparative analysis of the flow activity of the Homoljska potajnica intermittent spring: *Journal of the Geographic Institute "Jovan Cvijic" SABA*, v. 64, no. 1, p. 1-12. DOI: 10.2298/IJG1401001Ikatzer, F., 1909, *Karst und Karsthydrographie: Zur Kde, Balkanhaldbinsel* 8, Sarajevo.
- Lazarević, R., 1990, *Kučevska potajnica, Zavod za novinsko – izdavačku i propagandnu delatnost, JŽ*, Beograd.
- Kolda, A., Petrić, I., Mucko, M., Gottstein, S., Žutinić, P., Goreta, G., Ternjen, I., Rubinić, J., Radišić, M., and Gligora Udovič, M., 2019, How environment selects: Resilience and survival of microbial mat community within intermittent karst spring Krčić (Croatia): *Ecology* 12: e2063. <https://doi.org/10.1002/eco.2063>
- Lazarević, R., 2000, *Geomorfologija, Prirodno – matematički fakultet, odsek za geografiju, Banja Luka*.
- Marković, J., 1963, Homoljska potajnica, *Glasnik srpskog geografskog društva*, sveska XLIII, broj 2, Beograd.
- Mather, J.D., 2013, The history and hydrogeology of Laywell, a celebrated ebb and flow spring at Brixham: *Devon: Rep. Transactions of the Devon. Association for the Advancement of Science*, v. 145, p. 133-154.
- Mirković, S., Miljković, L., 2006, Turistička valorizacija i zaštita Homoljske potajnice: *Kongres srpskih geografa, Zbornik radova, knjiga 1*, str. 801-806, Soko Banja Cvijić J. (1896). *Izvori, tresave i vodopadi u istočnoj Srbiji, Glasnik srpske kraljevske akademije*, sveska LI, Beograd.
- Oliver, W., 1693, An extract of a letter from Dr William Oliver, communicated by Walter Moyle, Esq: *Philosophical Transactions*, v. 17, p. 908-909.
- Oraseanu, I., 2010, Calugari ebb and flow spring: *in* Oraseanu, I., and Iurkiewicz, A. eds., *Karst Hydrogeology of Romania (Belvedere, Oradea, Romania)*, p. 262-274.
- Petrović, J., 1981, Udvojena potajnica Promuklica (Double karst rhythmic spring Promuklica): *Glasnik Srpskog Geografskog Društva*, v. LXI, no.1, p. 333-343.
- Stephens, G., 1964, Rhythmic springs: *Cave Research Group of Great Britain, Transactions: Ledbury (Herefordshire) Tomo*, v. 7, no. 1, p. 3-9.

GENETIC AND FUNCTIONAL DIVERSITY OF SOIL BACTERIA AND FUNGI FROM DIFFERENT MICROHABITATS IN A KARST REGION IN SOUTHERN CHINA

Xinru Li¹, Min Zhou^{1,2}, Yidong Mi^{1,2}, Haiyan Chen¹, Hailei Su¹, Yuan Wei^{1,C}, Fuhan Guo³, Fanfan Wang¹

Abstract

Little is known about the difference between bacterial and fungal genetic and functional diversity in karst regions of south China. In this study, the genetic and functional diversity of bacteria and fungi in nine types of soil microenvironments in the karst region in Maolan National Nature Reserve in Guizhou were investigated by PCR-DGGE (Denaturing Gradient Gel Electrophoresis) and BIOLOG EcoPlates. Maolan National Nature Reserve is a UNESCO Biosphere Reserve and plays an important role in protecting the karst forest ecosystem and rare and endangered wild animals and plants in central Asia. The results showed that the diversity of both bacteria and fungi was high and the main factors influencing the diversity of bacteria and fungi were different. The bacterial community structure from different microhabitats under the same vegetation type had higher similarity than similar microhabitats in different vegetation types, which could indicate that the bacterial community structure was mainly controlled by vegetation. For fungi, similar microhabitat species under different vegetation types had higher similarities than different microhabitats species under the same vegetation type, which could indicate that the fungal community structure is mainly controlled by microhabitats. In addition, the metabolic patterns of similar microhabitats in different vegetation were different, while the metabolic patterns of different microhabitats in the same vegetation were not obviously different. In conclusion, the effect of vegetation types on soil microbial functional diversity was greater than that of microhabitats, and this difference was reflected by the different degrees of influence on soil microbial genetic diversity and community structure.

INTRODUCTION

The karst in southern China represents the most typical tropical-subtropical karst in the world (Yan et al., 2020; Zhou et al., 2020). It is a unique environmental unit in the subtropical climate zone, with a large elevation gradient and carbonate rock area, complex topography, and ecological fragility (Bai et al., 2013; Tian et al., 2016; Deng et al., 2020). Because of the natural conditions and human influence, the karst regions in China now have some special features including uncertain hydrological conditions, soil degradation, and low environmental recoverability (Zeng et al., 2018; Bai and Zhou, 2020; Wang et al., 2020). Rocky desertification may be the most typical environmental problem in the karst region in Guizhou Province in southeast China. Karst rocky desertification means that under the background of the fragile karst environment in the subtropical climate zone, unreasonable human social and economic activities have already caused serious soil erosion, large-scale exposure of bedrock, serious decline in land productivity, and soil degradation that is similar to desert landscapes (Zhan et al., 2013; Wang, 2020). Rocky desertification is a biogeochemical process that could be influenced by bacteria and fungi, and the effect is interactive (Wei et al., 2011; Hui et al., 2019).

Microorganisms are widely distributed in soil and can affect many kinds of soil biochemical reactions (Chen et al., 2019; Gregorutti and Caviglia, 2019). Soil microbial diversity is the basis and guarantee of the soil microorganism ecological function and plays an important role in maintaining soil quality and ecosystem stability and health. Soil microbial diversity can provide lots of information on soil and human influence, so it can also be used as a sensitive indicator of evaluating ecosystem stability and monitoring the change of soil quality. Therefore, the study of microorganisms in karst regions has attracted lots of attention. By studying the soil microbial diversity in mountains and grasslands in karst regions in Guizhou, it indicated that soil fertility, microbial biomass, and diversity were closely-related to each other (Jin et al., 2019). Another study chose arbuscular mycorrhizal fungi (AMF) as the research subject and found that microhabitats in karst regions in Guangxi Province could influence the richness of AMF by changing physical and chemical properties of soil and the vegetation types (Zhao et al., 2019). Some studies have shown that in karst regions, the microbial diversity can be affected by the vegetation and microhabitats (Dassen et al., 2017; Xue et al., 2017; Yang et al., 2018). However, previous studies ignored the discussion of genetic and functional diversity, especially on the comparison between the fungi and bacteria in microhabitats of karst regions. The role of soil microorganisms became more obvious when rocky desertification control and ecological restoration became more and more urgent. Thus, the characteristics of soil microorganisms from different kinds of microhabitats in karst region needs to be discussed due to the key role of soil microorganisms in soil succession, properties, and fertility. The microhabitat is a different small unit that can be

¹ State Key Laboratory of Environmental Criteria and Risk Assessment, Chinese Research Academy of Environmental Science, Beijing 100012, P.R. China

² College of Environment, Hehai University, Nanjing 210098, P.R. China

³ Key Laboratory of Environmental Protection and Ecological Construction, Shenyang Agricultural University, Shenyang 110866 P.R. China

^C Corresponding Author: rbq-wy@163.com

clearly distinguished in external form. There are various types of microhabitats, including stone surfaces, stone pits, stone trenches, and soil surfaces, which make the distribution of exposed rocks and soil uneven (Du and Wang, 2010).

We studied the genetic diversity of soil bacteria and fungi in karst regions in Guizhou by PCR and denaturing gradient gel electrophoresis (DGGE). We analyzed the functional diversity of soil bacteria and fungi using average well color development (AWCD) using BIOLOG EcoPlates to show the main carbon sources of soil microorganisms by Principal Component Analysis (PCA). Few previous studies have investigated the genetic and functional diversity of bacteria and fungi from different microhabitats. The specific goals of this study were: (1) to understand the distribution and physiological features of soil microorganisms in karst soil more comprehensively; (2) to identify which factors were important in driving bacterial and fungal community distribution in karst; and (3) to identify the main factors influencing soil microbial communities.

MATERIALS AND METHODS

Site Description and Sampling

Maolan Biosphere Reserve (25° 09' to 25° 20'N 107° 52' to 108° 05'E) is situated in Libo County, Guizhou Province in southeast China. In April 1996, Maolan was included in the UNESCO International Man and Biosphere Reserve Network (MAB) and became a world biosphere reserve (<https://en.unesco.org/mab>). The main protection objects of the biosphere reserve are the mid-subtropical karst forest ecosystem and rare and endangered wildlife. The total area of the reserve is 21,330 ha, of which the core area covers 5,150 ha. The elevation here is 630–1075 m above sea level. According to the record of the weather station in Libo (altitude: 423.9 m), the average annual temperature and precipitation of the reserve is 18.6 °C and 1760 mm respectively. The annual precipitation from April to October is 1162 mm, accounting for 80 % of the annual precipitation, is the annual rainy season (Zhou, 1987). The rocks in Maolan karst forest are mainly limestone and dolomite, with quartz sandstone and a small amount of shale in some places (Han et al., 2008). The region is famous for its virgin forest that is well-preserved on the karst landscape. The ecosystem types in Maolan include subtropical and temperate rainforests and agroecosystems (with rice, rape, sweet potato and medicinal plants). Every year there are about 60,000 visitors coming here because of its karst landscapes, streams, ponds, and waterfalls. There are vegetation succession communities with different degrees of degradation in this area, and the vegetation communities are relatively complete under each degree of degradation, which are conducive to the comparative study of different vegetation types in the same area.

According to the main feature of karst vegetation succession, three representative vegetation types were selected (secondary forest, shrubbery, and primeval forest) (Table 1). In each forest succession vegetation type, four kinds of microhabitats were studied, namely, soil surface, stone ditch, stone seam, and stone surface. The stone ditch has a wider opening and U-shape cross section. There are well-developed tree and shrub layers in the stone ditch with some herbs, ferns, and litters. The stone seam has a narrow opening and V-shaped cross section. There are more ferns, litters, and semi-decomposed organic matter in the stone seam. All the microhabitats were natural rather than man-made. In fact, only the samples of stone seam, stone ditch, and soil surface were collected during the sampling process, because the vegetation and soil of the stone surface microhabitat rarely met our experimental needs (Fig 1). The sample of a microhabitat was composed of three parallel samples of the same microhabitats. In our sampling sites, the rock type is mainly limestone.

Our research was conducted in August 2018. When sampling, we determine appropriate sample sizes according to the area of each microhabitat. We mixed samples of the same microhabitats from each forest site. We used disinfected shovels to remove the topsoil when sampling. The sample was sieved through a 2 mm sieve to ensure thorough mixing, and the samples were stored at 4 °C and –20 °C for later use. The soil in the study area is dominated by rendzina, a humus-rich soil formed from parent limestone and dolomite that are almost pure carbonate rocks. Except for the rainy season, the soil is relatively dry. The soil here is rich in Ca²⁺, Mg²⁺, and HCO₃⁻, with a pH of 7.5 to 8.0, an organic matter content of 75.5 g kg⁻¹ to 380 g kg⁻¹, and a total nitrogen content of 6.06 g kg⁻¹.

PCR-DGGE Analysis of Bacterial Diversity

DGGE can distinguish the sequence differences of target fragments with the same or similar molecular weight, and can be used to detect single base changes and genetic diversity, as well as polymorphism of PCR amplified DNA fragments. The principle of DGGE technology to detect nucleic acid sequences is that the DNA fragments of different sequences are denatured at their respective denaturant concentrations and eventually stagnate at their denaturant gradient position. Comparing PCR-DGGE dyed bands can determine the number and diversity of microorganisms in the soil samples (Muyzer and Smalla, 1998; Ma et al., 2003). Compared with other research methods of microbial diversity, this technology has some advantages. For example, PCR-DGGE can detect the whole microbial community (Zheng et al., 2013; Ling et al., 2020). Compared to modern molecular biology techniques, PCR-DGGE can analyze other microorganisms that coexist in the environment. By combining PCR-DGGE with other molecular biology techniques, we can get a more comprehensive analysis of microbial diversity.

Table 1. The Background information of three types of vegetation in Maolan reserve.

Vegetation Types	Slope	Bedrock Exposed Rate (%)	Vegetation Coverage (%)	Vegetation Characteristics
Primeval Forest	30-40	60-90	90-100	<p>The hierarchical structure is relatively complete, and the differentiation of plants between the tree layer, shrub layer, and herb layer is clear. The coverage of the tree layer is more than 80 % and the height is 10-20 m; the height of the shrub layer is 3-8 m and the coverage is 5-10 %.</p> <p>The dominant species are mainly round fruit incense, calyx haitong, small fruit Runan, green sandalwood, light leaf haitong, Rhizophora chinensis, ten major merits, celestial fruit and so on. The surface layer is covered with lichen and moss. In addition, understory is covered with 3-5 cm litter layer.</p>
Secondary Forest	30-40	50-80	90-100	<p>The hierarchical structure of the stand is clearly differentiated. The tree layer and shrub layer are relatively developed. The tree layer is 5-12 m high, while the coverage rate is over 80 %. The shrub layer is 2-3 m high, while the coverage is about 10 %.</p> <p>The dominant species mainly include Caragana yungui, Quercus glauca, Castanopsis fargesii, Pinus massoniana, Haitong, gerbera, etc. There are also a small number of vine thorns, ferns, lichens and other mosses. The thickness of the litter layer under the forest is 1-2 cm.</p>
Shrubbery Forest	20-30	70-80	80-100	<p>The vertical structure of the stand is simple, with few trees. It is mainly dominated by shrub layers, with a height of 2.5-3 m, a coverage rate of over 80 %, and a large degree of canopy closure.</p> <p>The dominant species are: Nandina domestica, Huaxiang, Gerbera, tiger thorn, Libo hornbeam, multi-veined Cyclobalanopsis glauca, rose hip etc. The litter cover under the forest is about 1-2 cm.</p>

The whole PCR-DGGE processes were divided into sample DNA extraction, gene amplification, separation, and strip recovery sequencing. Total Soil DNA was extracted using the Power Soil DNA Isolation Kit (MO BIO) Kit. All the



Figure 1. Different karst microhabitats in Maolan National Nature Reserve: A = Soil surface, B = Stone seam, and C = Stone ditch.

kit processes were strictly followed. For bacterial diversity analysis, the extracted DNA was used as templates for PCR. The amplification of bacterial DNA was performed using the universal 16S rDNA primers F338GC (5'-CGCCCGCCGCGCGC-GGCGGGCGGGGCGGG-GGCACGGGGGGCCTAC-GGAGGCAGCAG-3') and R518 (5'-ATTACCGCG-GCTGCTGG-3') (Shanghai Shenggong Biological Engineering Technology Service Company). The pre-denaturation condition was 94 °C for 5 min using the Model 475 Gradient Delivery System (Bio-Rad Laboratories Company). The first 20 cycles were 94 °C for 1 min, 65-55 °C for 1 min, and 72 °C for 3

min (the annealing temperature of each cycle decreased by 0.5 °C), and the last 10 cycles were 94 °C for 1 min, 55 °C for 1 min and 72 °C for 3 min, and finally, at 72 °C for 7 min. After electrophoresis in 1.5 % agarose gel, the products of the PCR reaction were stored at -20 °C degrees and analyzed by denaturing gradient gel electrophoresis. The denaturation gradient was from 30 % to 60 %. The concentration of polyacrylamide gel was 8 % in 1XTAE. Electrophoresis was conducted at 200 V and 75 V for 10 min and 10 h, respectively. After electrophoresis, the gel was dyed with silver dye (Bassam et al., 1991). The dyed gel was analyzed by BioRAD Gel doc-2000 Gel image analysis system, and all the electrophoresis bands were photographed.

PCR-DGGE Analysis of Fungal Diversity

The total DNA of soil samples was extracted and purified using the Mo BIO kit according to the manufacture's instruction, and the quality of extracted DNA was evaluated by 1 % agarose gel electrophoresis. The product was stored at -80 °C. The purified genomic DNA was used as a template for polymerase chain reaction (PCR). The PCR amplification was performed on the Mastercycler PCR machine. The primers of the fungi were U1: 5'-GTGAA ATTGTTGAAA GGGAA-3', U2-GC:5'-CGCCCCGCCGCGCGGGCGGGGCGGGGGCACGGGGGGGACTC CTTGGTCCGT-GTT-3'. All the primers used in this study were provided by Shanghai ShengGong Bioengineering Technology Service Company. PCR reaction conditions of the fungi were as follows: the pre-denaturation conditions were 94 °C for 3 min, and then 35 cycles were performed at 94 °C for 30 s, 53 °C for 30 s, 72 °C for 1 min and finally at 72 °C for 10 min. All subsequent treatments were the same as for bacteria.

Biolog Ecoplates Functional Diversity

The fresh soil samples were weighed to 10 g of dry soil and placed in 100 mL sterile water, then oscillated for 20 min at 220 rpm. After dilution to 10⁻³ with sterile water, 125 µL of diluted suspension was added to each well of Biolog ECO micropore plate (Biology, Hayward, CA, USA) using an 8-channel sample filler. After 168 hours of cultivation, Microlog Rel 4.2 software was used to read the absorbance value at 590nm wavelength on the BIOLOG EmaxTM automatic plate reader (BIOLOG, Hayward, CA, USA) every 24 hours (Scuhutter and Dick, 2001). We have listed the carbon sources in Table 2.

Statistical Analysis

DGGE profiles were analyzed by Bio - Rad QUANTITY ONE 4.4.0 software. Comparisons of banding profiles were established by the dice coefficient (C_s) that was drawn by the unweighted pair group method with arithmetic mean (UPGMA) plot

$$C_s = \frac{2j}{(a + b)}, \quad (1)$$

where j is the band common to samples A and B and a and b are the respective number of bands in samples A and B.

Shannon's index (H), richness (S), Simpson index (D), McIntosh index (U) and evenness (E) were used to characterize microbial diversity using the equations of Agryzkov et al., (2018). Average well color development (AWCD) could be used to access the microbial community's overall ability to exploit carbon sources.

Table 2. Correlation coefficients between main source of carbon and PC1 or PC2.

Carbon Source Type (PC1)	Carbon Source	Load Value	Carbon Source Type (PC2)	Carbon Source	Load Value
Carbohydrate	D-galactonic acid-γ-lactone	0.750	Carbohydrate	β-methyl-D-glucoside	0.614
Amino acids	L-Arginine	0.719	Sugar	D-galactonic acid γ-lactone	0.553
Carboxylic acids	D-galacturonic acid	0.454	Amino acids	L-Arginine	0.383
Amino acids	L-asparagine	0.448	Polymer	Tween 40	0.404
Polymer	Tween 40	0.566	Sugar	N-acetyl-D glucosamine	0.648
Carbohydrate	i-erythritol	0.435	Sugar	D-cellobiose	0.443
Amino acids	L-phenylalanine	0.776	Sugar	α-D-lactose	0.476
Polymer	Tween 80	0.649	Sugar	D,L-α-glycerol phosphate	0.626
Carbohydrate	D-mannitol	0.523	Carboxylic acids	D-malic acid	0.502
Parent compound	4-hydroxybenzoic acid	0.596
Amino acids	L-serine	0.598
Polymer	Glycogen	0.441
Carboxylic acid	D-glucosamine	0.490
Amino acids	Glycyl-L-glutamic acid	0.698
Amine	phenethylamine	0.507
Sugar	α-D-lactose	0.441
Amine	Putrescine	0.688

$$AWCD = \frac{\sum(C - R)}{n}, \quad (2)$$

where C is the optical density value of each well with culture medium, R is the optical density value of the control well, n is the data of the culture medium, and the n value of the ECO plate is 31 (Guo et al., 2015; Miao et al., 2019).

Analysis of Variance (ANOVA) was performed on microorganisms and carbon sources uptake data using SPSS 16. The correlation matrix method is used to compress the data to obtain the different principal components and the distance between samples. The principal component values obtained after PCA analysis were used to analyze the differences between the inspection groups and correlate with environmental factors.

RESULTS

Genetic Diversity Characteristics of Bacteria in Karst Microhabitats

The bacterial communities of different soil samples were observed by DGGE (Fig. 2A). All nine lanes had a large number of bands, which show that each microhabitat was rich in bacterial diversity (Fig. 2B). At the same time, every lane had specific bands, which could illustrate that the diversity of bacteria among different microhabitats was quite different. From the DGGE profile, the shrubby forest (lane 4, 5, and 6: line 34, 38, and 37 bands out of 78, respectively) exhibited the most abundant bands, while the abundance of secondary and primeval forest were similar. Lane 1 from the shrubby forest had the lowest number of bands; 24 bands out of 72. The secondary forest stone ditch (lane 8) and the secondary forest stone seam (lane 9) had relatively fewer bands (28 and 30 bands out of 72, respectively). The bacterial abundance from the soil surface, stone ditch, and stone seam may be very similar.

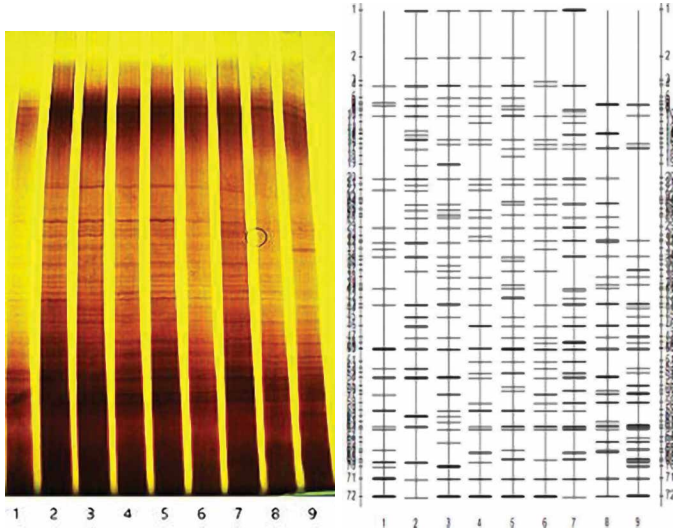


Figure 2. DGGE results of bacterial communities in different karst microhabitats samples: A = DGGE profile of amplified of bacterial communities in different karst microhabitats samples, and B = DGGE sketch map of bacterial communities in different karst microhabitats samples. Numbering is: 1. Primeval forest surface; 2. Primeval forest stone ditch; 3. Primeval forest stone seam; 4. Shrubby soil surface; 5. Shrubby stone ditch; 6. Shrubby stone seam; 7. Secondary soil surface; 8. Secondary forest stone ditch; and 9. Secondary forest stone seam.

stone ditch 5 (51.3 %) and the shrubby forest stone seam 6 (44.6 %), which could illustrate that the similarity among different microhabitats of the same vegetation may be higher.

Diversity and Richness Analysis

We then calculated the diversity index of soil bacterial communities in different karst microhabitats samples, by Shannon index (H), richness (S) and evenness (E) (Table 4). The Shannon index and richness of shrubby soil stone ditch were highest among all microhabitats, which were 3.65 and 39, respectively. The Shannon index and richness of primeval forest surface were only 3.13 and 24, which were the lowest. The mean value of bacterial Shannon index among different microhabitats was 3.46. In terms of evenness index, except for the primeval forest surface and secondary forest stone ditch, which were slightly lower, the others remained at 1.00. The trends of bacterial Shannon index and the richness of primeval forest microhabitats were: stone seam > stone ditch >

Similarity Analysis of Bacterial Communities in Different Karst Microhabitats

Based on the similarity of bacterial communities in different microhabitat samples, cluster analysis results were shown by a dendrogram, along with the similarity index between lanes (Fig. 3, Table 3). The dendrogram gave rise to two main branches of clusters and shared a similarity of 0.39. One branch cluster contains the secondary forest stone seam, soil surface and stone ditch, with the similarity of 0.47. The bacterial communities between primary forest soil surface and stone seam stayed closer with a similarity of 0.51. From the similarity index, the primary forest soil surface 1 had related with the primary forest stone ditch 2 (20.2 %) and the primary forest stone seam 3 (29.4 %). The shrubby forest soil surface 4 had high correlation with the shrubby forest

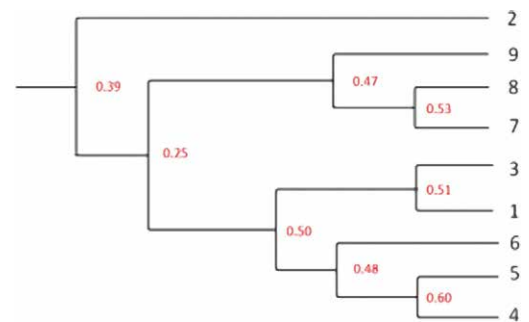


Figure 3. Similarity cluster of microbial communities among different karst microhabitats samples. Numbering is: 1. Primeval forest surface; 2. Primeval forest stone ditch; 3. Primeval forest stone seam; 4. Shrubby soil surface; 5. Shrubby stone ditch; 6. Shrubby stone seam; 7. Secondary soil surface; 8. Secondary forest stone ditch; and 9. Secondary forest stone seam.

Table 3. The similarity index between different microhabitat samples lanes of microbial communities (%).

Lane	1	2	3	4	5	6	7	8	9
1	100.0	20.2	29.4	33.5	22.1	35.9	24.2	25.6	22.2
2	20.2	100.0	48.3	40.5	48.5	43.1	47.0	25.1	30.7
3	29.4	48.3	100.0	58.4	45.1	44.1	42.5	29.5	34.7
4	33.5	40.5	58.4	100.0	51.3	44.6	39.6	35.7	33.5
5	22.1	48.5	45.1	51.3	100.0	52.1	39.6	26.7	39.9
6	35.9	43.1	44.1	44.6	52.1	100.0	40.1	34.1	29.4
7	24.2	47.0	42.5	39.6	39.6	40.1	100.0	25.0	37.9
8	25.6	25.1	29.5	35.7	26.7	34.1	25.0	100.0	25.0
9	22.2	30.7	34.7	33.5	39.9	29.4	37.9	25.0	100.0

Note: 1. Primeval forest surface; 2. Primeval forest stone ditch; 3. Primeval forest stone seam; 4. Shrubbery soil surface 5. Shrubbery stone ditch; 6. Shrubbery soil stone seam; 7. Secondary forest surface; 8. Secondary forest stone ditch; and 9. Secondary forest stone seam.

Table 4. Shannon Index, richness and evenness of bacterial communities in different microhabitats samples.

Microhabitat Samples	Shannon Index (H)	Richness (S)	Evenness (E)
Primeval forest soil surface	3.13	24	0.99
Primeval forest stone ditch	3.48	33	1.00
Primeval forest stone seam	3.54	35	1.00
Shrubbery forest soil surface	3.51	34	1.00
Shrubbery forest stone ditch	3.65	39	1.00
Shrubbery forest stone seam	3.48	33	1.00
Secondary forest soil surface	3.57	36	1.00
Secondary forest stone ditch	3.38	30	0.99
Secondary forest stone seam	3.42	31	1.00
Mean value	3.46	32	0.99

surface, and the order of fungal Shannon index and richness of secondary forest microhabitats and shrubbery were: soil surface > stone seam > stone ditch and stone ditch > soil surface > stone seam, respectively. However, the diversity index and abundance of different microhabitats did not show the same trend.

Genetic Diversity Characteristics of Fungi in Karst Microhabitats

DGGE Analysis of Soil Fungal Communities

The fungal communities of different soil samples were observed by DGGE (Fig. 4A). Similar to bacteria, all the lanes had a large number of bands that showed each karst microhabitat was rich in fungal diversity (Fig. 4B). There were both the conserved and specific bands among all lanes, indicating that there were both similar and specific fungal populations in the soil in different types of microhabitats in karst. It was obvious that there were more fungal bands than bacterial bands, which suggested different abundance and diversity of fungal and bacterial species in karst microhabitats. From the DGGE profile, the shrubbery forest (lane 4, 5, and 6; 52, 64, and 46 bands out of 129, respectively) exhibited the most abundant bands, and the abundance of secondary and primeval forest was similar, which was also similar to bacteria (line 34, 38, and 37 bands out of 78, respectively). Lane 8 from the primeval forest had the lowest quantity of bands (42 bands out of 129). The average fungal bands in stone seam were higher than those in stone ditch and soil surfaces (52 bands,

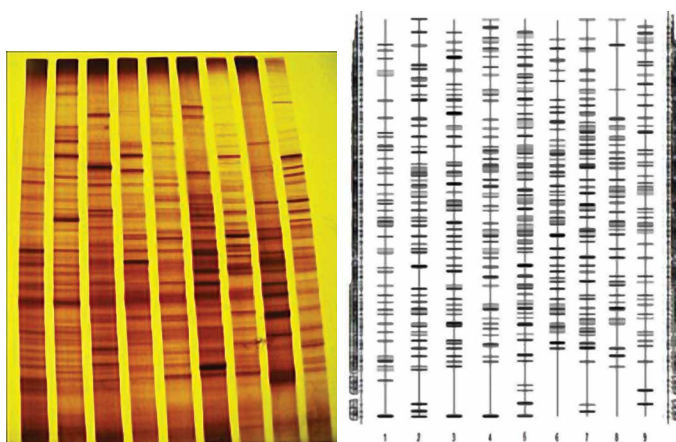


Figure 4. DGGE results of fungal communities in different karst microhabitats samples: A = DGGE profile of amplified of fungal communities in different karst microbial samples, and B = DGGE sketch map of fungal communities in different karst microhabitats samples. Numbering is: 1. Secondary forest stone seam; 2. Secondary forest stone ditch; 3. Secondary forest soil surface; 4. Shrubbery stone seam; 5. Shrubbery stone ditch; 6. Shrubbery soil surface; 7. Primeval forest stone seam; 8. Primeval forest stone ditch; and 9. Primeval forest soil surface.

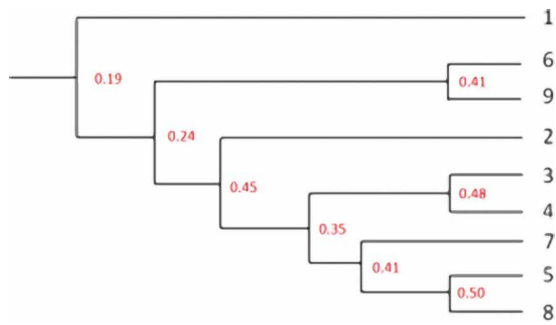


Figure 5. Similarity cluster of fungal communities among different microhabitats samples. Numbering is: 1. Secondary forest stone seam; 2. Secondary forest stone ditch; 3. Secondary forest soil surface; 4. Shrubbery stone seam; 5. Shrubbery stone ditch; 6. Shrubbery soil surface; 7. Primeval forest stone seam; 8. Primeval forest stone ditch; and 9. Primeval forest soil surface.

45 bands, and 49 bands, all out of 127), but the bacterial bands in the three microhabitats were similar.

Similarity Analysis of Fungal Communities in Different Microhabitats

As shown in Figure 5, the dendrogram gave rise to two main branches of clusters and shared a similarity of 0.19 (Fig. 5, Table 5). The fungal communities between secondary forest stone ditch and shrubbery stone ditch stayed closer with a high similarity of 0.50. The similar indexes of the stone ditch of three microhabitats were similar. The primeval forest surface 9 had correlation with secondary forest surface 3 (16.9 %) and shrubbery soil surface 6 (19.0 %), which were a little low but very close. In general, the similarity index of community structure among different microhabitats was very low, indicating that there were differences in fungal community structure among different karst microhabitats.

Table 5. The similarity index of different microhabitats sample lanes of microbial communities (%).

Lane	1	2	3	4	5	6	7	8	9
1	100.0	29.0	26.3	41.2	35.5	18.0	17.5	21.8	17.9
2	29.0	100.0	39.0	21.6	49.9	28.8	30.4	33.6	19.1
3	26.3	39.0	100.0	26.8	43.9	42.4	31.5	25.8	16.9
4	41.2	21.6	26.8	100.0	32.7	19.3	22.6	27.2	18.5
5	35.5	49.9	43.9	32.7	100.0	34.7	34.4	38.2	33.7
6	18.0	28.8	42.4	19.3	34.7	100.0	48.2	33.2	19.0
7	17.5	30.4	31.5	22.6	34.4	48.2	100.0	34.7	30.1
8	21.8	33.6	25.8	27.2	38.2	33.2	34.7	100.0	16.5
9	17.9	19.1	16.9	18.5	33.7	19.0	30.1	16.5	100.0

Note: 1. Secondary forest stone seam; 2. Secondary forest stone ditch; 3. Secondary forest surface; 4. Shrubbery soil stone seam; 5. Shrubbery stone ditch; 6. Shrubbery soil surface; 7. Primeval forest stone seam; 8. Primeval forest stone ditch; 9. Primeval forest surface.

Fungal Diversity and Richness Analysis

We then calculated the diversity index of soil fungal communities in different karst microhabitats samples by Shannon index (H), richness (S) and evenness (E) (Table 6). The highest diversity index of karst microhabitats fungi was primeval forest stone seam (4.11 and 62), shrubbery forest stone ditch (4.32 and 76) and stone seam (4.10 and 61). The lowest diversity index of all the microhabitats were primeval forest stone ditch (3.75 and 43) and secondary forest stone seam (3.78 and 44). The mean value in fungal Shannon index among different microhabitats was 3.99. There was no difference among the evenness from the nine types of microhabitats. The trend of fungal Shannon index and the richness of primeval forest microhabitats was: stone seam > stone ditch > surface, and the trends of fungal Shannon index

Table 6. Shannon index, richness and evenness of fungal communities in different karst microhabitats samples.

Microhabitat samples	Shannon index (H)	Richness (S)	Evenness (E)
Primeval forest surface	3.90	50	1.00
Primeval forest stone ditch	3.75	43	1.00
Primeval forest stone seam	4.11	62	1.00
Shrubbery forest surface	3.96	53	1.00
Shrubbery forest stone ditch	4.32	76	1.00
Shrubbery forest stone seam	4.10	61	1.00
Secondary forest surface	3.98	54	1.00
Secondary forest stone ditch	4.00	55	1.00
Secondary forest stone seam	3.78	44	1.00
Mean value	3.99	55	1.00

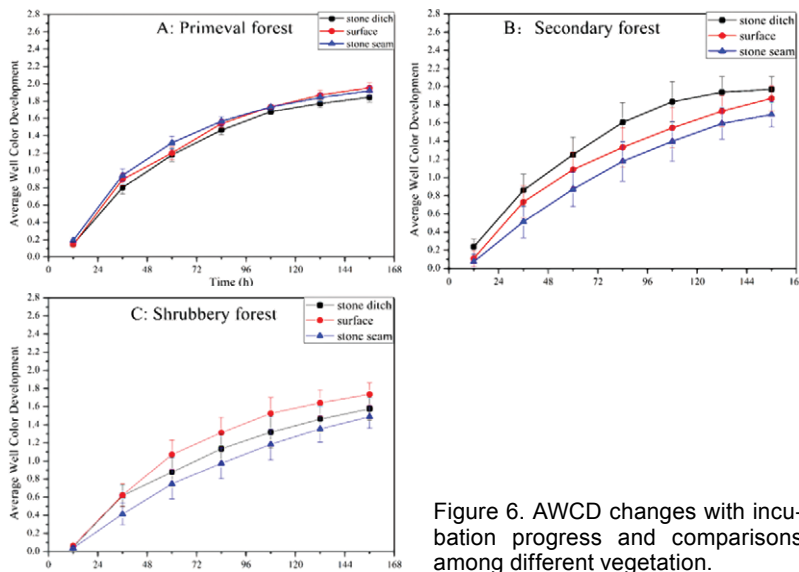


Figure 6. AWCD changes with incubation progress and comparisons among different vegetation.

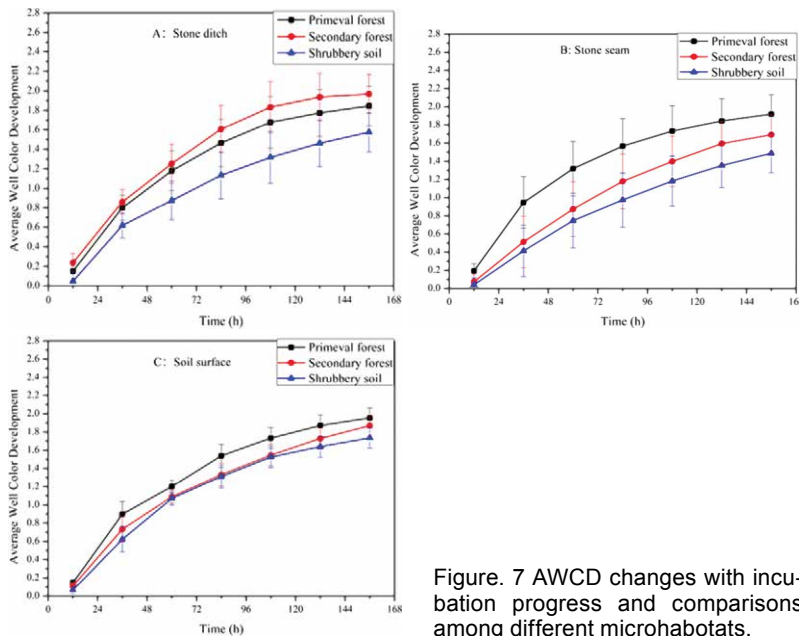


Figure 7 AWCD changes with incubation progress and comparisons among different microhabitats.

and richness of secondary forest microhabitats and shrubbery were: stone ditch > surface > stone seam and stone ditch > stone seam > surface, respectively.

AWCD Analysis of Microbial Diversity in Karst Microhabitats

Average Well Color Development (AWCD) using Biolog EcoPlates is used to indicate the activity of soil microorganisms and the ability of soil microorganisms to use single carbon sources, and it could reflect soil microbial activity and microbial community physiological functional diversity (Miao et al., 2019). The density and activity of bacteria increased with the AWCD. Conversely, the lower the AWCD value would indicate lower bacterial density and lower activity. We accessed the different microhabitats of the same sample plot (Fig. 6). The AWCD values of the primeval forest including stone ditch, stone seam, and soil surface did not show differences, which indicated that the activity values were basically the same (Fig. 6A). The AWCD values and microbial activity of the secondary forest were obviously different during the growth period and the trend of three microhabitats was: soil surface > stone ditch > stone seam (Fig. 6B). The study accessed the same microhabitats of different sample vegetation (Fig. 7A–C). The AWCD values of three different types of vegetation in the stone ditch were different and the trend was: secondary forest > primeval forest > shrubbery forest (Fig. 7A). The three AWCD curves of the stone seam and soil surface were clearly different and the trend of microbial activity was the same: primeval forest > secondary forest > shrubbery forest (Fig. 7E–F).

Diversity Index of Soil Microbial Community Metabolism Function

Shannon's diversity index indicates functional diversity, which means that the number of carbon sources used by soil microbial communities of all the ecosystems when the color change rate is consistent. For example, the bigger the Shannon index is the higher is the soil microbial community functional diversity. McIntosh index includes the number of species (richness) and the evenness of individual distribution in species. The diversity will become higher as the number of microbial types increases. Similarly, an increase in the evenness of individual distribution among species will also increase the functional diversity. The Simpson index is always used to access the dominant species (Ma, 2019). Table 7 shows the diversity index based on 96 hours of data. In the primeval forest, the Shannon's diversity indexes of three kinds of microhabitats were: stone ditch > soil surface > stone seam (Table 7). As for secondary and shrubbery forest, the trends of Shannon's diversity index were stone ditch > soil surface > stone seam and soil surface > stone ditch > stone seam, respectively. On the whole, the highest Shannon's diversity index was the secondary forest stone ditch (3.29), while the lowest was the secondary stone seam (3.15). The Simpson indexes of all investigated karst microhabitats were between 0.95–0.96, which were not different. The McIntosh indexes of karst microhabitats in primeval forest were different. The trend was: stone seam > soil surface > stone ditch. In the secondary forest microhabitats, the McIntosh index of stone ditch > soil surface > stone seam. The trend of McIntosh index of shrubbery forest was: soil surface > stone ditch > stone seam, which was also different among primeval and secondary forest. Overall, the highest and lowest evenness index was the primeval stone seam (10.28) and shrubbery stone seam (6.79).

Table 7. Shannon's diversity index, Simpson index and McIntosh index of nine karst microhabitats.

Sample	Shannon Index	Simpson Index	McIntosh Index
Primeval forest soil surface	3.25 ± 0.05	0.958 ± 0.002	10.19 ± 0.61
primeval forest stone ditch	3.26 ± 0.01	0.959 ± 0.000	9.62 ± 0.90
Primeval forest stone seam	3.19 ± 0.04	0.955 ± 0.002	10.65 ± 0.71
Secondary forest soil surface	3.20 ± 0.04	0.955 ± 0.002	9.15 ± 0.46
Secondary forest stone ditch	3.29 ± 0.04	0.960 ± 0.002	10.28 ± 1.14
Secondary forest stone seam	3.13 ± 0.04	0.951 ± 0.002	8.39 ± 0.60
Shrubbery soil surface	3.21 ± 0.02	0.956 ± 0.001	8.79 ± 0.56
Shrubbery stone ditch	3.18 ± 0.05	0.955 ± 0.003	7.78 ± 0.94
Shrubbery stone seam	3.15 ± 0.06	0.952 ± 0.004	6.79 ± 0.86

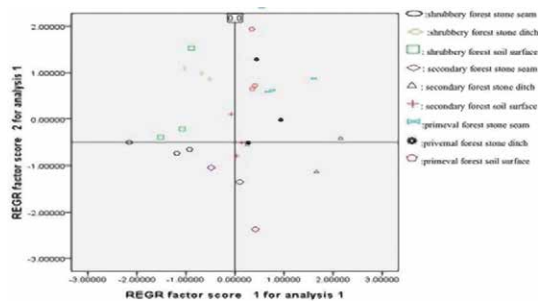


Figure 8. PCA of soil microbial carbon source utilization diversity of different karst microhabitats.

Principal Component Analysis (PCA) of Soil Microbial Carbon Source Utilization

Different microhabitats showed differences on PC1 and PC2, indicating that their soil microorganisms do use different carbon sources (Fig. 8, Tables 2 and 8). The significance value less than 0.05 have been marked in red. The significant value is less than 0.05, indicating that the two objects have significant differences. Further variance analysis of the scoring coefficients of the principal components of carbon sources in different microhabitat habitats showed that on PC1, the soil microbial metabolism patterns in three types of microhabitats (stone seam, stone ditch, and soil surfaces of shrubbery forest) were not significantly different. In the secondary forest plots, there were significant

differences in the metabolic patterns between the stone seam and stone ditch, and between the stone ditch and the soil surface, but there was no significant difference in the metabolic patterns between the stone seam and the soil surface. On PC2, there were significant differences between the stone seam and the soil surface of the shrub forest, and there were no significant differences between the stone seam and the ditch, and between the stone ditch and the soil surface. There was no significant difference in the soil surface, stone seam, and stone ditch in the primeval forest. As for carbon resources analysis, there were five kinds of amino acids, four kinds of carbohydrates, three kinds of polymers, two kinds of carboxylic acids and amines, and one kind of amphiphilic compound showing significant relation to PC1, which indicated that the main carbon resources influenced PC1 were amino acids, carbohydrates, and polymers. Similarly, among the carbon sources that were significantly related to PC2, the carbon source affecting PC2 was mainly the carbohydrates because of six carbohydrates of PC2. In summary, the carbon sources that differentiated the microhabitat soil microbial metabolism patterns were mainly carbohydrates, amino acids, and polymers.

DISCUSSION

Karst microhabitats are special and unique environmental units and have different effects on ecological environments in karst regions. Soil microorganisms are very important to the ecological restoration in karst regions. At different stages of desertification, the number and distribution of microorganisms are also different. Therefore, the soil microbiome can be a good indicator of soil quality and soil health in the karst rocky desertification regions (Tang et al., 2019). In fact, soil microorganisms in different microhabitats have different distributions and structural features that may indicate the role of soil microorganisms, such as bacteria and fungi, would also be different. The relationship between genetic and functional diversity in different microhabitats and soil microbial diversity is more direct. Some existing studies have ignored the various characteristics and roles of soil microorganisms in the microhabitats (Yu et al., 2004; Wei et al., 2008). Our experiments made up for this shortcoming to some degree and more comprehensively considered and studied the genetic and functional diversity of bacteria and fungi in different karst microhabitats, which may provide new insights into ecological restoration and rocky desertification management in karst regions.

There many ways to study microbial diversity in different microhabitats. Our study showed that the diversity of bacteria and fungi in microhabitats of the karst could be detected by PCR-DGGE. Wu et al. (2019) used phospholipid fatty acid (PLFA) technology to study the bacterial and fungal diversity in Maolan Natural Nature Reserve. The trends of diversity were: the stone trough > the stone ditch > the soil surface > the stone cave > the stone seam, which were similar to our result. Liao et al. (2013b) used substrate-induced respiration to access the amount of the soil microbial biomass in karst regions in Huajiang dry hot valley watershed in Guizhou Province. The results showed that the substrate-induced respiration of soil from their stone ditch was relatively high in all microhabitats investigated.

Table 8. The Principle Component scores for different microhabitats.

Dependent Variable	(I) VAvR00001	(J) VAR00001	Mean Difference (I-J)	Std. Error	Significance	95% Confidence Interval	
						Lower Bound	Upper Bound
REGR factor score 1 for analysis 1	1	2	0.46562679	0.40115217	0.261	-0.3771627	1.3084162
		3	0.64492381	0.40115217	0.125	-0.1978656	1.4877133
	2	1	-0.46562679	0.40115217	0.261	-1.3084162	0.3771627
		3	0.17929703	0.40115217	0.660	-0.6634924	1.0220865
	3	1	-0.64492381	0.40115217	0.125	-1.4877133	0.1978656
		2	-0.17929703	0.40115217	0.660	-1.0220865	0.6634924
	4	5	-1.34571883 ^a	0.40115217	0.004 ^a	-2.1885083	-0.5029294
		6	-0.02245966	0.40115217	0.956	-0.8652491	0.8203298
	5	4	1.34571883 ^a	0.40115217	0.004 ^a	0.5029294	2.9387222
		6	1.32325917 ^a	0.40115217	0.004 ^a	0.4804697	2.1885083
	6	4	0.02245966	0.40115217	0.956	-0.8203298	0.8652491
		5	-1.32325917 ^a	0.40115217	0.004 ^a	-2.1660486	-0.4804697
	7	8	-0.26144823	0.40115217	0.523	-1.1042377	0.5813412
		9	-0.68163703	0.40115217	0.106	-1.5244265	0.1611524
	8	7	0.26144823	0.40115217	0.523	-0.5813412	1.1042377
		9	-0.42018880	0.40115217	0.309	-1.2629782	0.4226006
	9	7	0.68163703	0.40115217	0.106	-0.1611524	1.5244265
		8	0.42018880	0.40115217	0.309	-0.4226006	1.2629782
REGR factor score for analysis 1	1	2	0.43734062	0.50234562	0.395	-0.6180484	1.4927296
		3	-0.41109415	0.50234562	0.424	-1.4664831	1.6442948
	2	1	-0.43734062	0.50234562	0.395	-1.4927296	0.6180484
		3	-0.84843477	0.50234562	0.108	-1.9038238	0.2069542
	3	1	0.41109415	0.50234562	0.424	-0.6442948	1.4664831
		2	0.84843477	0.50234562	0.108	-0.2069542	1.9038238
	4	5	-0.88944052	0.50234562	0.094	-1.9448295	0.1659485
		6	-1.19088983	0.50234562	0.029 ^a	-2.2462788	-0.1355009
	5	4	0.88944052	0.50234562	0.094	-0.1659485	1.9448295
		6	-0.30144931	0.50234562	0.556	-1.3568383	0.7539397
	6	4	1.19088983 ^a	0.50234562	0.029 ^a	0.1355009	2.2462788
		5	0.30144931	0.50234562	0.556	-0.7539397	1.3568383
	7	8	-0.93958746	0.50234562	0.078	-1.9949764	0.1158015
		9	-1.61499360 ^a	0.50234562	0.005 ^a	-2.6703826	-0.5596046
	8	7	0.93958746	0.50234562	0.078	-0.1158015	1.9949764
		9	-0.67540615	0.50234562	0.195	-1.7307951	0.3799828
	9	7	1.61499360 ^a	0.50234562	0.005 ^a	0.5596046	2.6703826
		8	0.67540615	0.50234562	0.195	-0.3799828	1.7307951

^a The mean difference is significant at the 0.05 level.

Note: 1. Primeval forest stone seam; 2. Primeval stone ditch; 3. Primeval soil surface; 4. Secondary forest stone seam; 5. Secondary forest stone ditch; 6. Secondary soil surface; 7. Shrubbery stone seam; 8. Shrubbery stone ditch; 9. Shrubbery soil surface;

Effects of Karst Microhabitats on Soil Microbial Genetic Diversity

In our study, the karst microhabitats investigated had abundant bacterial and fungal communities and functional diversity. The bacterial communities among nine research sites do have differences. Cluster analysis (Fig. 3) indicated that the bacterial community structure of different microhabitats under the same vegetation type was more similar than that of similar microhabitats under different vegetation types. The vegetation, rather than microhabitats, was more important to the distribution of bacteria in karst. In previous studies, we could demonstrate that the differences in the karst microhabitats soil heterogeneity were manifested by changes in clay particles, micro-aggregates, and effective nutrient quantities (Zhou and Lei, 2007; Wakerlin et al., 2008; Zhang et al., 2015). All the factors could influence the bacterial diversity on a high level, which was also the reason why the bacterial community structure was different among all kinds of microhabitats. Vegetation is an important source of soil nutrients. Microorganism distribute by the types and amount of plant litter and the rate of water loss from the soil surface. Under the same vegetation, the structure and kind of soil carbon and nitrogen resources are basically consistent, while other factors including soil water content, temperature, pH, aeration, physical structure, and the organic content could be different (Murugan et al., 2014; Ren et al., 2018). Therefore, our study shows that the bacterial community structure was mainly controlled by the composition of carbon source at the micro-geomorphic scale of microhabitats.

The distribution of fungi was sensitive to changes in environmental factors that may lead to changes in diversity. The heterogeneity of different microhabitats is high in water content, heat, light, and soil fungal diversity. The heterogeneity may be the reason why the fungal diversity may be lower than bacterial diversity in different microhabitats. According to the phylogenetic tree (Fig. 5) for fungi, similar microhabitats in different vegetation types were more similar than those in the same vegetation type. The impact of microhabitats on its diversity and community structure was greater than the impact of vegetation types on its diversity, which was opposite to bacterial diversity. Our research indicated that the spatial heterogeneity had different influences on the bacteria and fungi. Many studies had illustrated that the soil organic content could significantly influence the soil fungal community structure (Fan et al., 2012; Chen et al., 2016; 2017).

Hu et al. (2016) employed site comparisons of Chinese toona reforestation to study the relationship among soil microbial biomass carbon (MBC), microbial biomass nitrogen, and other organic matter and soil microbial community structure and diversity. Their results showed that the microbial biomass and activity of reforested soil were higher, which meant that the vegetation could increase the microbial diversity by increasing the content of soil organic matter. The complexity of vegetation carbon sources, the organic matter imported, and the spatial and temporal differences of carbon sources in the same system are three important factors influencing soil fungal functional diversity. The spatial and temporal differential may have a closer connection with the fungal community functional diversity in karst regions because the fungal community structure and abundance of different microhabitats of the same vegetation type were both different. In fact, the dominant species of fungi among different microhabitats were very different, which indicated that for a single karst vegetation type or ecosystem, the microhabitats within it could play all kinds of roles on the whole material cycle by changing microbial structure and dominant species. In the future, when carrying out karst ecosystem protection and rocky desertification restoration, it is necessary not only to pay attention to the role of the microhabitat, but also to take into account differences in the ecological effectiveness of the microhabitat in different restoration stages.

Effects of Karst Microhabitats on Soil Microbial Functional Diversity

Among the three vegetation types, the metabolic activities of the three types of microhabitat in each plot were different. The differences were not obvious in the primary forest, but reached a significant level in the secondary and shrub forest. On the whole, the karst microhabitats had a significant impact on the soil microbial activity. The trend of microbial activity of three types of microhabitats was: stone ditch > soil surface > stone seam, possibly due to structural differences among the karst microhabitats. The stone seam is relatively closed with small openings and weak material accumulation, leading to lower microbial activity than other microhabitats. The stone ditch and soil surface are relatively open to the environment with a large area and a large amount of litter accumulation. Litter could provide rich carbon sources during the decomposition process (Zhu et al., 2012) that is beneficial to the microbial growth and material cycle (Liao et al., 2012; 2013a). The changing trends of AWCD of three samples were basically maintained in primary forest >> secondary forest > shrubbery forest, indicating that the vegetation degradation or reverse succession would decrease soil microbial activity of all microhabitats, even the whole ecosystem microbial activity consistent with the study by Zhu et al. (2012). The microbial metabolism patterns of the three types of microhabitats under the same vegetation type showed basically no significant differences, while the microbial metabolism patterns of the same vegetation type under the same microhabitats showed significant differences. According to the results of AWCD, for samples of the same vegetation type, the heterogeneity brought by different microhabitats was mainly reflected in the number of single populations of microorganisms rather than microbial community structure, so the metabolic pattern did not change. However, the change of vegetation types would affect the community structure and the number of single populations of microorganisms simultaneously, which made the metabolic patterns different from each other. In conclusion, the vegetation may be the main factor influencing soil microbial metabolic patterns in karst regions.

ACKNOWLEDGMENTS

This work was supported by the Special Project of Technology Development and Research of Scientific Research Institute of Ministry of Science and Technology (No.2014EG166135); National Natural Science Foundation of China (No. 41977294).

REFERENCES

- Agryzkov, T., Tortosa, L., and Vicent, J.F., 2018, An algorithm to compute data diversity index in spatial networks: Applied Mathematics and Computation, v. 337, p. 63–75. <https://doi.org/10.1016/j.amc.2018.04.068>
- Bai, X.Y., Wang, S.J., and Xiong, K.N., 2013, assessing spatial-temporal evolution processes of karst rocky desertification land: indications for restoration strategies: Land Degradation & Development, v. 24, no. 1, p. 47–56. <https://doi.org/10.1002/ldr.1102>
- Bai, Y.X., and Zhou, Y.C., 2020, The main factors controlling spatial variability of soil organic carbon in a small karst watershed, Guizhou Province, China: Geoderma, v. 357. <https://doi.org/10.1016/j.geoderma.2019.113938>
- Bassam, B.J., Caetano-Anollks, G., and Gresshoff, P.M., 1991, Fast and sensitive silver staining of DNA in Polyacrylamide Gels: Analytical Biochemistry v. 196, p. 80–83. [https://doi.org/10.1016/0003-2697\(91\)90120-I](https://doi.org/10.1016/0003-2697(91)90120-I)

- Chen, D.M., Duan, Y.Q., Yang, Y.H., Jin, Y., and Yuan, L., 2016, Influence of crop rotation on enzyme activities and fungal communities in flue-cured tobacco soil: *Acta Ecologica Sinica*, v. 36, p. 2373–2381. <https://doi.org/10.5846/stxb201411052183>
- Chen, H., Li, D., Mao, Q., Xiao, K., and Wang, K., 2019, Resource limitation of soil microbes in karst ecosystems: *Science of the Total Environment*, v. 650, no. Pt 1, p. 241–248. <https://doi.org/10.1016/j.scitotenv.2018.09.036>
- Chen, Z.H., Liang, X., Li, Y.C., Li, Y.F., Xu, Q.F., Wu, Q.F., Li, S.H., and Shen, Z.M., 2017, Effects of different fertilization regimes on soil fungal communities under *Phyllostachys violascens* stand: *Chinese Journal of Applied Ecology*, v. 28, p. 1168–1176. <https://doi.org/10.13287/j.1001-9332.201704.002>
- Dassen, S., Cortois, R., Martens, H., de Hollander, M., Kowalchuk, G.A., Van der Putten, W.H., and De Deyn, G.B., 2017, Differential responses of Soil Bacteria, Fungi, Archaea and Protists to plant species richness and plant functional group identity: *Molecular Ecology*, v. 26, no. 15, p. 4085–4098. <https://doi.org/10.1111/mec.14175>
- Deng, Y., Wang, S., Bai, X., Luo, G., Wu, L., Chen, F., Wang, J., Li, Q., Li, C., Yang, Y., Hu, Z., and Tian, S., 2020, Spatiotemporal dynamics of soil moisture in the karst areas of China based on reanalysis and observations data: *Journal of Hydrology*, v. 585. <https://doi.org/10.1016/j.jhydrol.2020.124744>
- Du, X.L., and Wang, S.J., 2010, Micro-habitat characteristics in the karst desertification area: a case study of the Wangjiazhai Catchment in Guizhou Province: *Earth and Environment*, v. 38, p. 255–261. <https://doi.org/10.14050/j.cnki.1672-9250.2010.03.009>
- Fan, F., Li, Z., Wakelin, S.A., Yu, W., and Liang, Y., 2012, Mineral fertilizer alters cellulolytic community structure and suppresses soil cello-biohydrolase activity in a long-term fertilization experiment: *Soil Biology and Biochemistry*, v. 55, p. 70–77. <https://doi.org/10.1016/j.soilbio.2012.06.008>
- Gregorutti, V.C., and Caviglia, O.P., 2019, Impact of crop aerial and root biomass inputs on soil nitrifiers and cellulolytic microorganisms: *Soil and Tillage Research*, v. 191, p. 85–97. <https://doi.org/10.1016/j.still.2019.03.018>
- Guo, P., Zhu, L., Wang, J., Wang, J., and Liu, T., 2015, Effects of alkyl-imidazolium ionic liquid [Omim]Cl on the functional diversity of soil microbial communities: *Environmental Science and Pollution Research International*, v. 22, no. 12, p. 9059–9066. <https://doi.org/10.1007/s11356-014-4052-8>
- Han, G., Tang, Y., and Tan, Q., 2008, Geochemical composition of rainwater in karst forest: Case study of Maolan Nature Reserve, Guizhou Province: *Bulletin of Mineralogy, Petrology and Geochemistry*, v. 27, p. 363–368 <https://doi.org/CNKI:SUN:KYDH.0.2008-04-009>
- Hu, N., Li, H., Tang, Z., Li, Z., Li, G., Jiang, Y., Hu, X., and Lou, Y., 2016, Community size, activity and C:N stoichiometry of soil microorganisms following reforestation in a karst region: *European Journal of Soil Biology*, v. 73, p. 77–83. <https://doi.org/10.1016/j.ejsobi.2016.01.007>
- Hui, N., Sun, N., Du, H., Umair, M., Kang, H., Liu, X., Romantschuk, M., Liu, C., 2019, Karst rocky desertification does not erode ectomycorrhizal fungal species richness but alters microbial community structure: *Plant and Soil*, v. 445, no. 1-2, p. 383–396. <https://doi.org/10.1007/s1104-019-04319-z>
- Jin, Z.L., Liu, G.P., Zhou, M.T., and Xu, W.-N., 2019, Indicative function of soil microbial community on soil nutrients in karst mountain grassland: *Southwest China Journal of Agricultural Sciences*, v. 32, p. 2638–2645. <https://doi.org/10.16213/j.cnki.scjas.2019.11>
- Liang, X., Ren, H.D., Li, S., Leng, X.H., and Yao, X.H., 2017, Soil bacterial community structure and co-occurrence pattern during vegetation restoration in karst rocky desertification area: *Frontiers in Microbiology*, v. 8, p. 2377. <https://doi.org/10.3389/fmicb.2017.02377>
- Liao, H.K., Jiang, L., Li, J., Yang, J.J., and Feng, Y.Q., 2012, Distribution characteristics of soil carbon and nitrogen under different vegetation types in micro-habitats of karst dry-hot valley region of south western China: *Soils*, v. 44, p. 421–428.
- Liao, H.K., Li, J., and Long, J., 2013a, Effect of vegetation type and micro-habitat on soil active organic carbon and basal respiration in karst dry and hot valley region of Guizhou Province, China: *Chinese Journal of Soil Science*, v. 44, p. 580–586. <https://doi.org/10.19336/j.cnki.trtb.2013.03.012>
- Liao, H.K., Li, J., Long, J., Zhang, W.J., and Liu, L.F., 2013b, Soil characteristics of different microhabitats of Chinese prickly ash in karst mountain areas of Guizhou Province: *Journal of Agro-Environment Science*, v. 32, p. 2429–2435. <https://doi.org/10.11654/jaes.2013.12.016>
- Ling, Y., Li, W., Tong, T., Li, Z., Li, Q., Bai, Z., Wang, G., Chen, J., and Wang, Y., 2020, Assessing the microbial communities in four different Daqus by using PCR-DGGE, PLFA, and Biolog Analyses: *Polish Journal of Microbiology*, no. 69, p. 27–37. <https://doi.org/10.33073/pjm-2020-004>
- Liu, Y., Li, L.L., Zhao, K., Wang, L.L., and Rao, Y., 2004, Analysis on physical feature of karst mountains desertification soil under different land use: *Journal of Soil and Water Conservation*, v. 18, p. 142–145. <https://doi.org/10.13870/j.cnki.stbcxb.2004.05.035>
- Ma, J., 2019, Generalised grey target decision method for mixed attributes based on the improved Gini–Simpson Index: *Soft Computing*, v. 23, no. 24, p. 13449–13458. <https://doi.org/10.1007/s00500-019-03883-x>
- Ma Y., Holmström, C., Webb, J., and Leberg, S.F.K., 2003, Application of Denaturing Gradient Gel Electrophoresis (DGGE) in microbial ecology: *Acta Ecologica Sinica*, v. 23, p. 1561–1569.
- Miao, L., Guo, S., Liu, Z., Liu, S., You, G., Qu, H., and Hou, J., 2019, Effects of nanoplastics on freshwater biofilm microbial metabolic functions as determined by BIOLOG ECO Microplates: *International Journal of Environmental Research and Public Health*, v. 16, no. 23. <https://doi.org/10.3390/ijerph16234639>
- Murugan, R., Beggi, F., and Kumar, S., 2014, Belowground carbon allocation by trees, understory vegetation and soil type alter microbial community composition and nutrient cycling in tropical Eucalyptus plantations: *Soil Biology and Biochemistry*, v. 76, p. 257–267. <https://doi.org/10.1016/j.soilbio.2014.05.022>
- Muyzer, G., and Smalla, K., 1998, Application of Denaturing Gradient Gel Electrophoresis (DGGE) and Temperature Gradient Gel Electrophoresis (TGGE) in microbial ecology: *Antonie van Leeuwenhoek International Journal of General and Molecular Microbiology*, v. 73, p. 127–141. <https://doi.org/10.1023/A:1000669317571>
- Ren, C., Zhang, W., Zhong, Z., Han, X., Yang, G., Feng, Y., and Ren, G., 2018, Differential responses of soil microbial biomass, diversity, and compositions to altitudinal gradients depend on plant and soil characteristics: *Science of the Total Environment*, v. 610–611, p. 750–758. <https://doi.org/10.1016/j.scitotenv.2017.08.110>
- Schutter, M., and Dick, R., 2001, Shifts in substrate utilization potential and structure of soil microbial communities in response to carbon substrates: *Soil Biology & Biochemistry*, v. 33, p. 1481–1491. [https://doi.org/10.1016/s0038-0717\(01\)00057-8](https://doi.org/10.1016/s0038-0717(01)00057-8)
- Tang, J., Tang, X., Qin, Y., He, Q., Yi, Y., and Ji, Z., 2019, Karst rocky desertification progress: soil calcium as a possible driving force: *Science of the Total Environment*, v. 649, p. 1250–1259. <https://doi.org/10.1016/j.scitotenv.2018.08.242>
- Tian, Y., Wang, S., Bai, X., Luo, G., and Xu, Y., 2016, Trade-offs among ecosystem services in a typical karst watershed, SW China: *Science of the Total Environment*, p. 566–567, p. 1297–1308. <https://doi.org/10.1016/j.scitotenv.2016.05.190>
- Wakelin, S.A., Macdonald, L.M., Rogers, S.L., Gregg, A.L., Bolger, T.P., and Baldock, J.A., 2008, Habitat selective factors influencing the structural composition and functional capacity of microbial communities in agricultural soils: *Soil Biology and Biochemistry*, v. 40, no. 3, p. 803–813. <https://doi.org/10.1016/j.soilbio.2007.10.015>

- Wang, S.J., 2002, Concept deduction and its connotation of karst rocky desertification: *Carsologica Sinica*, v. 21, p. 101–105.
- Wang, Z.J., Li, S.L., Yue, F.J., Qin, C.Q., Buckerfield, S., and Zeng, J., 2020, Rainfall driven nitrate transport in agricultural karst surface river system: Insight from high-resolution hydrochemistry and nitrate isotopes: *Agriculture, Ecosystems & Environment*, v. 291, 106787. <https://doi.org/10.1016/j.agee.2019.106787>
- Wei, Y., Yu, L.F., Zhang, J.C., Yu, Y.C., and Deangelis, D.L., 2011, Relationship between vegetation restoration and soil microbial characteristics in degraded karst regions: a Case Study: *Pedosphere*, v. 21, no. 1, p. 132–138. [https://doi.org/10.1016/s1002-0160\(10\)60088-4](https://doi.org/10.1016/s1002-0160(10)60088-4)
- Wu, Q.S., Long, J., Li, J., Liao, H.K., Liu, L.F., Wu, J.N., and Xiao, X., 2019, Effects of different microhabitat types on soil microbial community composition in the Maolan Karst Forest in Southwest China: *Acta Ecologica Sinica*, v. 39, p. 1009–1018. <https://doi.org/10.5846/stxb201801110084>
- Yan, Y.J., Dai, Q.H., Hu, G., Jiao, Q., Mei, L.N., and Fu, W.B., 2020, Effects of vegetation type on the microbial characteristics of the fissure soil-plant systems in karst rocky desertification regions of SW China: *Science of the Total Environment*, v. 712, p. 136543. <https://doi.org/10.1016/j.scitotenv.2020.136543>
- Yang, F., Wu, J., Zhang, D., Chen, Q., Zhang, Q., and Cheng, X., 2018, Soil bacterial community composition and diversity in relation to edaphic properties and plant traits in grasslands of southern China: *Applied Soil Ecology*, v. 128, p. 43–53. <https://doi.org/10.1016/j.apsoil.2018.04.001>
- Zeng, F., Jiang, Z., Shen, L., Chen, W., Yang, Q., and Zhang, C., 2018, Assessment of multiple and interacting modes of soil loss in the Karst Critical Zone, southwest China (SWC): *Geomorphology*, v. 322, p. 97–106. <https://doi.org/10.1016/j.geomorph.2018.08.043>
- Zhan, W., Liu, S.J., Ye, Y.Y., Chen, H.S., Wang, K.L., and Wang, G.F., 2013, Spatial variability of soil nutrients and its influencing factors in typical karst virgin forest: *Transactions of the Chinese Society of Agricultural Engineering*, v. 29, p. 93–101. <https://doi.org/10.3969/j.issn.1002-6819.2013.01.013>
- Zhang, W., Chen, H.S., Wang, K.L., Zhang, J.G., and Hou, Y., 2008, Spatial variability of soil nutrients on hillslope in typical karst peak-cluster depression areas: *Transactions of the Chinese Society of Agricultural Engineering*, v. 24, p. 67–73.
- Zhang, W., Zhao, J., Pan, F., Li, D., Chen, H., and Wang, K., 2015, Changes in nitrogen and phosphorus limitation during secondary succession in a karst region in southwest China: *Plant and Soil*, v. 391, no. 1-2, p. 77–91. <https://doi.org/10.1007/s11104-015-2406-8>
- Zhao, L., Gai, S.S., Zheng, S.M., Hu, Y.J., Liu, H.Y., and He, X.Y., 2019, Effects of season and microhabitat on soil arbuscular mycorrhizal fungi communities in a karst shrubland: *Research of Agricultural Modernization*, v. 40, p. 870–877. <https://doi.org/10.13872/j.1000-0275.2019.0083>
- Zheng, J., Liang, R., Zhang, L., Wu, C., Zhou, R., and Liao, X., 2013, Characterization of microbial communities in strong aromatic liquor fermentation pit muds of different ages assessed by combined DGGE and PLFA analyses: *Food Research International*, v. 54, no. 1, p. 660–666. <https://doi.org/10.1016/j.foodres.2013.07.058>
- Zhou, J., and Lei, T., 2007, Review and prospects on methodology and affecting factors of soil microbial diversity: *Biodiversity Science*, v. 15, p. 306–311. <https://doi.org/10.1360/biodiv.070069>
- Zhou, L., Wang, X., Wang, Z., Zhang, X., Chen, C., and Liu, H., 2020, The challenge of soil loss control and vegetation restoration in the karst area of southwestern China: *International Soil and Water Conservation Research*, v. 8, no. 1, p. 26–34. <https://doi.org/10.1016/j.iswcr.2019.12.001>
- Zhou Zhengxian , 1987, *Scientific Survey of the Maolan Karst Forest*, Guizhou Renmin Chubanshe, Guiyang: Guizhou People's Press, (in Chinese)
- Zhu, H., He, X., Wang, K., Su, Y., and Wu, J., 2012, Interactions of vegetation succession, soil bio-chemical properties and microbial communities in a karst ecosystem: *European Journal of Soil Biology*, v. 51, p. 1–7. <https://doi.org/10.1016/j.ejsobi.2012.03.003>

AN INTERPRETATION OF CUEVA DE LA HUACHIZCA, SANTA CLARA DEL COBRE, MICHOACÁN, MÉXICO

Cinthia Marlene Campos^{1,C}, José Luis Punzo-Díaz², Veronica Lopez Delgado³, Avto Goguitchaichvili³, and Juan Morales³

ABSTRACT

Cueva de la Huachizca is located in the humid forests of the Municipio of Santa Clara del Cobre, Michoacán. During the Postclassic period (1300–1520 AD), Santa Clara del Cobre was a part of the Tarascan *Señorio*. Ethnographic accounts describe the use of Cueva de la Huachizca as a place of refuge during the Cristero Rebellion (1921–1926). Recent investigations suggest a long history of use including graffiti and inscriptions from the 1800s–1900s and a rock art panel. The panel consists of pecked petroglyphs depicting a man facing an eagle, above a spiral motif. Stylistic analysis of the panel suggests that the rock art was created during pre-Hispanic times, likely by the Postclassic Tarascans. As observed in several regions of Mesoamerica, for the Tarascans, caves were also liminal spaces and had an important role in Postclassic Tarascan cosmology. A ceramic *resinera*, a pine resin pot, an eagle's feather, and charcoal were also recovered. The *resinera* age was estimated by researchers at Archaeomagnetic Services, Geophysics Institute at the National Autonomous University of México-Campus Morelia, Michoacán to between 1921 and 1980. Ethnographic and ethnohistoric accounts describe caves as houses of fertility and rain deities, an idea that while slightly transformed, has survived over 500 years of colonization, and remains in the communities' social memories. These findings demonstrate the cave's significance among the descendent communities and Cueva de la Huachizca as an important sacred site.

INTRODUCTION

Cueva de la Huachizca is located in the humid forests of the *municipio*, Santa Clara del Cobre near the archaeological sites Itziparatzico and Pátzcuaro. During the Postclassic period (1300–1520 AD), Itziparatzico was part of the Tarascan *Señorio*. The *Señorio* was divided into three capitals, Ihuatzio, Pátzcuaro, and Tzintzuntzan. At the time of contact, Tzintzuntzan was the main politico-religious center, from which the *Calzonci*, or supreme ruler, controlled a multi-ethnic empire spanning over 75,000 square kilometers including Itziparatzico (Alcalá, 2013; Pollard, 2008; Punzo-Díaz, 2014) (Fig. 1). The *Señorio* consisted of a series of tributary city-states united by the *Uacúsecha* or Eagle's Men lineage, (Alcalá, 2013; Pollard, 2008). Santa Clara del Cobre belonged to Itziparatzico, one of the largest and most important metalsmithing towns (Alcalá, 2013; Maldonado and Rehen, 2009; Punzo-Díaz, 2014).

The name “Cueva de la Huachizca” comes from the word *huaches*, or Indian, which suggests that the cave was primarily utilized by the Indigenous population (Warren, 1990). According to informants from Santa Clara del Cobre, the cave has been known for centuries and remains a part of the communities' social memory. According to informants, the cave served as a refuge during the Mexican Revolution and Cristero Rebellion (1921–1926). The cave was first scientifically recorded in 2014 by *Proyecto Arqueología y Paisaje del Area Centro-Sur de Michoacán* (PAPACSUM), directed by José Luis Punzo-Díaz (Punzo-Díaz et al., 2015). Their report (Punzo-Díaz et al., 2015) suggests that the cave is small, composed of a single chamber. The cave was visited again in 2016 by Cinthia M. Campos and Alejandro Valdes-Herrera as part of the *Tarascan Caves Reconnaissance*, a sub-project of PAPACSUM 2016-2017 (Campos, 2018). This survey found

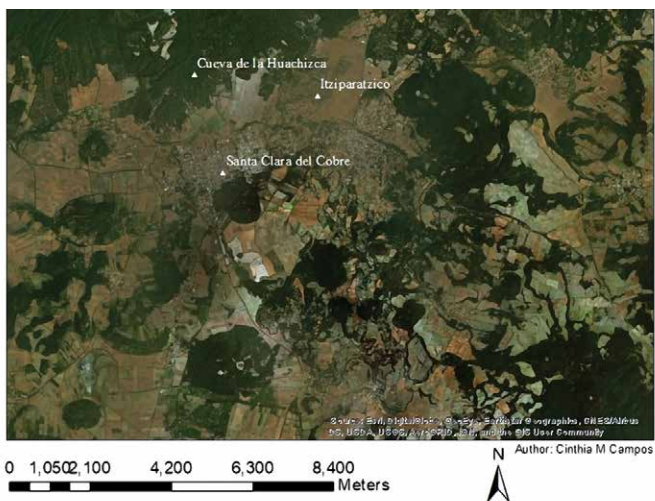


Figure 1. Cueva de la Huachizca, located in the forests of Salvador Escalante, Michoacán, México. The map shows the cave in relation to the Postclassic Tarascan site of Itziparatzico and the colonial town of Santa Clara del Cobre.

¹ Anthropology, Binghamton University, State University of New York, 4400 Vestal Parkway East Binghamton, NY 13902-6000 United States

² Arqueología, Instituto Nacional de Antropología e Historia- Morelia, Francisco I. Madero Oriente 799 Col. Centro C.P. 58000 Morelia, Michoacán, México

³ Servicio Arqueomagnético Nacional, Instituto de Geofísica- Universidad Nacional Autónoma de México- Morelia, Michoacán

^C Corresponding Author: cmcampos13@outlook.com

a passage heading northward from the known chamber that eventually led to a second, partially blocked entrance. In total, 109 m of passage were mapped, making this one of the longest caves in the area.

CUEVA DE LA HUACHIZCA

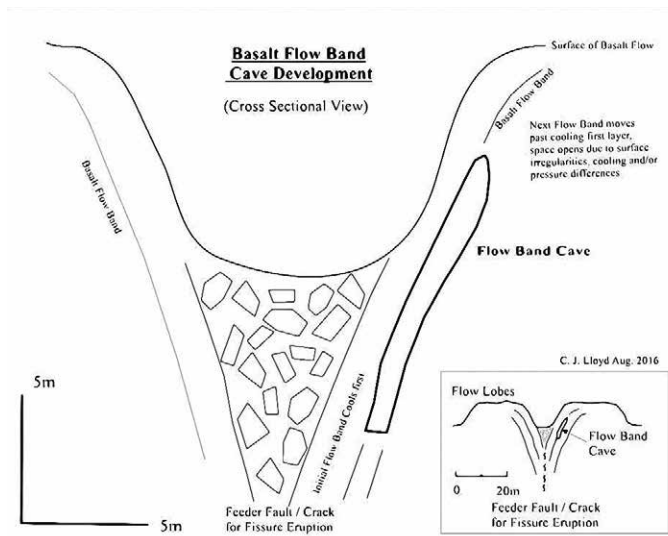


Figure 2. A cross section view of the formation of the cave. (Lloyd, 2016).

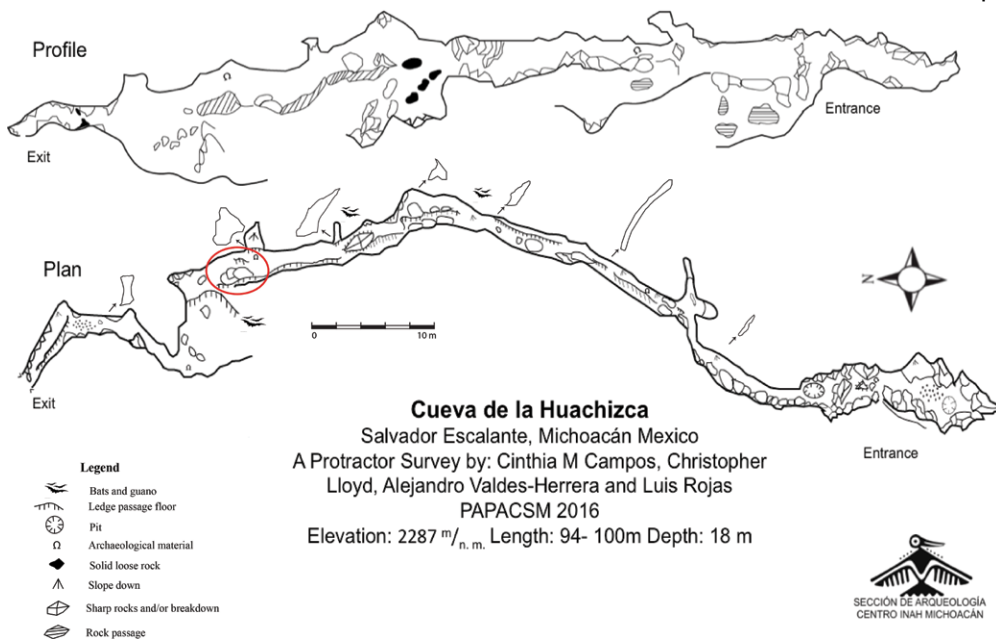


Figure 3. The plan view and profile maps of Cueva de la Huachizca showing the dimensions and complexity of the cave. The location of the rock art panel and the feather is circled in the plan view map.

test to the cave's historical use. The eastern and western walls of the southern entrance contain multiple etchings of names and dates of individuals who visited the cave during the late 1800s and early 1900s. A Spanish-style cross measuring 10 cm in height by 6 cm in width is incised in the basalt on the north-facing wall. Carved onto that same panel, just below the cross, is the year 1996. The eastern and western walls of the southern entrance contain multiple etchings of names and visiting dates of cave visitors during the late 1800s and early 1900s. Less graffiti is found at the north entrance and completely absent beyond 50 m north of the south entrance

South of the main entrance is a spacious chamber measuring 9.5 m long by 3.5 m wide and 3 m at its highest point. Inside the southern chamber, the walls consist of basalt breakdown through which little to no light enters. A looter's pit

This area of Michoacán is part of the Trans-Mexican Volcanic Belt, and therefore, non-karstic. Geologist Christopher Lloyd (2016) proposes that Cueva de la Huachizca is a flow-band basalt cave (Fig. 2). Flow bands can occur during laminar lava flows if there are differing viscosities in the lava thus segregating the laminar lava flows. Lava draining from a lower flow band leaves an accretionary band above with an open space between the bands as lava drains when the flow ceases from the eruption.

Cueva de la Huachizca (Fig. 3) consists of a single long rift passage oriented north-south that drops some 18 m over its length. The southern or main cave entrance is obscured by large breakdown and measures 3.5 m in width by 2 m in height. Just inside the southern entrance, the cave becomes multi-leveled with a lower passage paralleling the upper passage. The lower passage was deemed unsafe and was not further explored.

In June 2016, the cave was surveyed and mapped. This cave was particularly difficult to map because it is filled with loose sharp basalt breakdown and requires some climbing skills. Due to the complexity of the cave, two experienced cavers from Guadalajara assisted, Christopher Lloyd and Luis Rojas. Despite its relatively small size, it took three days to survey and map the cave. The first survey was conducted with a tandem SUUNTO compass and clinometer. The strong magnetic force inside the cave interfered greatly with azimuth readings, forcing us to restart the survey using a protractor and two small handheld laser pointers. As part of the surface survey, artifacts were photographed, recorded, and collected for further lab analysis. A third visit was dedicated to recording, photographing, and tracing the rock art panel.

The presence of graffiti at-

was found in the southeastern corner of the chamber, seven meters south of the entrance. The looter's pit is circular in shape and measures 75 cm in diameter and ranges between 5 cm and 10 cm in depth. The pit contained an accumulation of soil and breakdown at its base suggesting that it was dug in antiquity. No artifacts were found in the pit nor in the southern part of the cave.

As the cave lacks skylights, all artifacts documented in the cave were found in the dark zone. At 17 meters north of the south entrance, the first artifact was identified, a partially broken ceramic *resinera*, a pine resin pot, which functioned as a resin lamp when ignited. *Resineras* were used from colonial times into the historic period. The *resinera* measures 17 cm in height, 20 cm in diameter, and 2–3 cm in thickness. It was lodged between two basalt slabs approximately three meters below the walking passage. The *resinera* was found upright, in a section where the sloping basalt walls narrow sharply. Had the *resinera* been smaller in diameter, it would have slipped down into the lower passage which is physically inaccessible. The *resinera* was filled with charred pine resin and small organic fibers possibly used as kindling. The cave's conditions and location of the ceramic lamp allowed for the excellent preservation of the lamp and its contents.

THE ROCK ART PANEL AND ASSOCIATED ARTIFACTS



Figure 4. The rock art panel at Cueva de la Huachizca depicting a man facing an eagle above an inward spiral motif and an arrow pointing in the southern direction.

At 63.52 m north of the southern entrance, a rock art panel was incised on the east wall (Fig. 4). The panel is etched on a flat section of basalt, clear of lava stalactites. It is noteworthy because the passage opens to a height of 3.5 m, with a full meter of walking surface, as opposed to the narrow sloping 0.5 m wide passages found in much of the rest of the cave. At its highest point, the rock art panel is located 1.60 m above the floor, at eye level for an individual of short to medium stature.

The panel, 2.15 m in length and 1 m in height, consists of four motifs. A clearly defined spiral motif is located in the lower north-west quadrant of the panel; the motif is similar to those recorded at Tzintzuntzan (Gómez-Mussenth, 2010; Olmos, 2010). At the spiral glyph's level is a line and an arrow pointing south towards the entrance. Above and east of the spiral is an image of a man's head with clearly defined hair combed back and his mouth open. Two thin lines are

noted emerging out of the man's mouth. The man is facing southward and is at the same level as an eagle's head, which is significantly larger than the man. The eagle motif is facing in a northward direction, looking directly at the man. Tracing of the rock art panel revealed a crown motif above the eagle's head that was not visible in photographs. The crown is not as deeply incised as the other images; it is very thin and faint compared to the man, spiral, and eagle that appeared to be traced over multiple times. This leads us to believe it may have been added later in time and perhaps using different tools.

On a ledge in the western wall 1.5 m above the floor and across from the rock art panel, a single feather was found. The feather, 27.5 cm long by 6 cm wide, is weathered yet maintains its size and color (Fig. 5). Biologist Dr. Jorge Schöndube, at the National Autonomous University of Mexico (UNAM)-Morelia, identified the feather as a primary feather. Its size, coloration, and features indicate that it may have belonged to an *Aquila chrysaetos*, widely known as a golden eagle (Schöndube, personal communication 2016). Magnified images of the feather show that its calamus, or the hollow point, is intact, suggesting that the feather was not brought in by an animal. The feather's integrity and context suggest that it was deliberately placed in front of the rock art panel, perhaps as an offering. The feather was found in association with three small pieces of charcoal further confirming human activity. The passage floor below the rock art panel was littered with burnt wood and charcoal. More evidence of burning was found approaching the north entrance, including black soot on the roof of the cave and small fragments of burned wood.



Figure 5. The feather found on a ledge across the rock art panel (right) and its calamus (left). Despite some weathering along the hollow shaft and barbs, the feather is free of sediment, rodent, and bill marks.

RESULTS OF ARCHAEOMAGNETIC DATING

The *resinera* was analyzed using archaeomagnetic techniques at the facilities of the National Archaeomagnetic Service at UNAM- Morelia. Absolute archaeointensity measurements were performed using the Thellier double heating

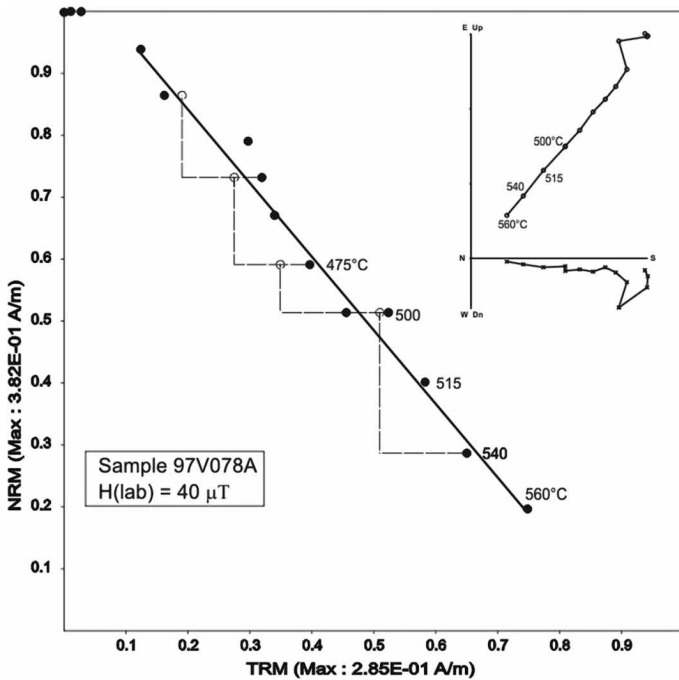


Figure 6. Representative Natural Remanent Magnetization (NRM)—Thermomagnetic Remanent Magnetization (TRM) plots, also known as Arai-Nagata plot and associated Zijderveld demagnetization diagrams for the representative samples.

method (Thellier and Thellier 1959) as modified by Coe et al. (1978). An ASC TD-48 single chamber demagnetizer equipped with the coils to produce magnetic fields and an AGICO JR6-A spinner magnetometer were used for the analysis. A fragment of the *resinera* was broken into 6 samples and pressed into salt pellets to facilitate their treatment as standard paleomagnetic samples. Intensity determination (Fig. 6) was carried out in 14 temperature steps, between room temperature and 560 °C. Temperature reproducibility between two heatings to the same temperature was less than 2 °C and laboratory field intensity was set to 40 μT and held with a precision better than 0.1 μT . During the experiment, several control heatings, so-called pTRM-checks, were carried out. The cooling rate dependence of TRM (Thermoremanent Magnetization) was investigated following a modified procedure described by Chauvin et al. (2000). At the end of experiments, all specimens were heated three more times at 560 °C, to create three consecutive TRMs under the same laboratory field. The three consecutive TRMs were performed at different laboratory assisted speeds, fast, slow, fast. To minimize the anisotropy effect of TRM, each fragment was divided into at least six specimens and embedded in salt pellets in six positions ($\pm X$, $\pm Y$, $\pm Z$) relative to *a priori* selected direction of the sample. The magnetic field was then applied along the +Z direction. In this way, anisotropy effects were canceled out or at least minimized as showed by Morales et al. (2015).

All six analyzed specimens yielded technically acceptable determinations (Table 1). For these samples, the NRM fraction f used for determination ranges between 0.69 and 0.75, while the quality factor q ranges from 5.7 to 17.5 (Table 1). The individual archaeointensity values obtained in this study range from 39.14 μT to 49.45 μT with a fragment mean value of 44.78 μT . The results of archaeomagnetic dating (Fig. 7) using the last model SHADIF14K of Pavón-Carrasco et al. (2011, 2014) combined with data retrieved from the Teoloyacan geomagnetic observatory (Hernández-Quintero et

Table 1. Archaeointensity results obtained from the *resinera* specimens.

Sample	Lab Code	n	T _{min} - T _{max} (°C)	f	g	q	B (μT)	
							Corrected	σB (μT)
SCC1a	97V073A	11	200 - 560	0.81	0.89	17.5	45.59	1.4
SCC1b	97V074A	10	250 - 560	0.81	0.88	12.8	46.57	1.2
SCC1c	97V075A	9	250 - 540	0.75	0.79	5.7	39.14	1.6
SCC1d	97V076A	10	250 - 560	0.77	0.82	13.6	42.39	1.1
SCC1e	97V077A	9	250 - 540	0.79	0.78	6.6	49.44	2.1
SCC1f	97V078A	11	200 - 560	0.78	0.87	18.1	45.54	1.2

T_{min} - T_{max} = the temperature interval involved for intensity determination.
 n = the number of heating steps used for the intensity determination.
 f = the fraction of NRM used for intensity determination.
 g = the gap factor.
 q = the quality factor as defined by Coe et al. (1978).
 B_{corr} = archeointensity value corrected for cooling rate effect.

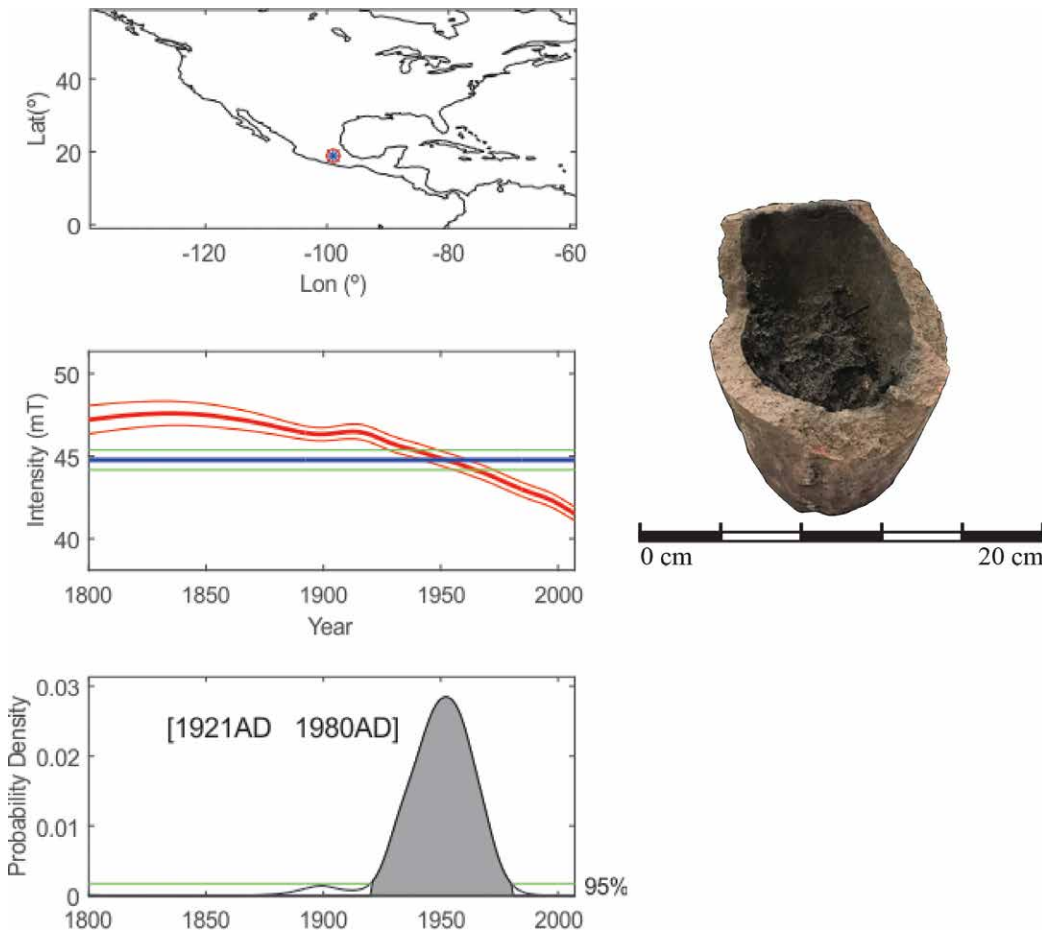


Figure 7. Archaeomagnetic dating of the *resinera* samples using a MATLAB tools provided by Pavón-Carrasco et al. (2011, 2014) using SHA14Kdif model combined with observatory data for the last 100 years.

site for the ancient Tarascans.

Today, the cave is protected as part of the Ejido Salvador Escalante and remains under the protection of the local Indigenous community. According to local Purépecha speakers, to them “any opening into the earth” is considered a cave (Warren, 1990). The association of caves as sacred spaces is further supported by Carrasco’s (1952) ethnographic studies among the Purépecha communities and Punzo-Díaz’s (2018) interpretation of the *Relación sobre la Resistencia de Michoacán (Pátzcuaro)* (Ramírez, 1959). Therefore, in a non-karst volcanic region, where caves seldomly form, a cave of this size is certainly noteworthy.

al., 2018) yielded a time interval between 1921 and 1980 as the best estimate of the *resinera* recovered at Cueva de la Huachizca.

DISCUSSION

As mentioned, the cave is located in Santa Clara del Cobre, which in pre-Hispanic times was part of the ancient town of Itziparátzico. This archaeological site consists of differentiated habitation areas, a wide variety of ceramic and lithic artifacts, 30 small mounds, and a large *yacata* (Punzo-Díaz, 2014) confirming Tarascan presence. In pre-Hispanic times Itziparátzico was an important site as it connected the copper mines in the Tierra Caliente region to the Lake Pátzcuaro Basin, where the socio-political leaders of the Tarascans resided. Metals played a significant role in agency and power in pre-Colombian times and their use was limited to the politico-religious elite. According to *Relación de Michoacán*, metals were considered to be the excrement of the gods. Silver was associated with Xaratanga, the Tarascan water and moon goddess, while gold and copper were associated with Curicaueri, the Tarascan fire and solar deity (Alcalá, 2013; Pollard, 1993, 2008; Roskamp, 2005, 2010a). Therefore, as a copper manufacturing site, Itziparátzico was an important socio-political

The feather is significant as it suggests that locals continue to visit the cave. As described in the *Relación de Michoacan*, both wood and feathers, particularly those of predatory birds, were often presented as ceremonial offerings to the solar deity, Curicaueri (Alcalá, 2013). Interestingly, results from radiocarbon analysis conducted on the charcoal remains recovered at the base of the rock art panel indicated that the samples were post-1950, suggesting continued visits through the 19th and 20th centuries. The archaeomagnetic analysis suggest that the *resinera* was likely dropped between 1921 and 1980 which is contemporaneous to the Cristero Rebellion (1921-1926) confirming the community's ethnographic and historical accounts. As a result, we cannot ascertain whether the feather and charcoal were introduced at the same time or by the same individuals. However, it is clear that the artifacts found are not all contemporaneous. This is significant as it links to the pre-Hispanic and colonial past until modern-day, suggesting that the cave remains an important and sacred site to the community.

The rock art found within the cave differs from rock art recorded elsewhere in Michoacán, which often consists of anthropomorphic creatures, geometric designs, handprints, and figures (Gómez-Mussent, 2010; Olmos, 2010). The rock art resembles images drawn by Indigenous informants in *Codice Plancarte*, *Codice de Huetamo*, and the *Lienzo de Jujucato* or *Jicalan* (Corona-Núñez, 1986, Roskamp 2005, 2010b) (Fig. 8). This would suggest that the rock art panel was carved during the Late Postclassic or the colonial period. The continuous occupation of Indigenous Purépecha in the region along with the particular iconographic symbols and stylistic form, suggest that the ancient Tarascans are the creators of the rock art panel. As noted, the manufacture of the petroglyphs was not uniform. The lines of the crown above the eagle are much thinner, finer, and shallower. The difference between these lines and the rest of the panel is so stark, suggesting the crown was added later and perhaps with different tools.



Figure 8. Contact period illustrations of Tarascan nobles, *Acús Thicátame* as depicted in the *Codice de Carapan*. *Curicaueri*, the Tarascan solar and fire deity, is represented as an eagle wearing a Spanish-style crown (Corona-Núñez, 1986).

a headdress in the form of an eagle. The identification of the sculpture as a throne was based on a painting at Oxtotitlan Cave in Guerrero that depicts a man seated on a throne with the same jaguar iconography as La Venta Altar 4. The man on the throne is shown wearing an eagle costume. Thus, the connection between caves, eagles, and rulership dates back to at least 1000 BC.

Anthropologists have emphasized an important class of rituals called “rites of passage” (Brady and Prufer, 2005; Heyden 1975, 2005). Van Gennep (1960) defined rites of passage as ceremonies that marked transitions in social status, age, and/or space or location. He noted that these rites of passage followed a common script in which the individual entered a liminal space where the ceremony was performed and then re-entered a normal space with his/her new status. Liminal space needs to be isolated and distinctively different from “normal” space, making caves ideal liminal spaces. All individuals experience several rites of passage throughout their lives, such as birth, puberty, marriage, and death. Doris Heyden (1975, 2005) stated that caves were frequently the settings for rites of passage, particularly involving the accession to rulership.

The rite of passage is well documented in the Aztec accession ritual. The *tlatoani* spent the night before taking office in the temple of Yopico praying and bloodletting. The temple was a symbolic cave with a hole in the floor called *oztoc*, “cave” (Townsend, 1987). A similar rite of passage is described in Fray Jeronimo de Alcalá's *Relación de Michoacán* (Alcalá, 2013). According to narratives, Tariacuri, the *Calzonci* renowned for uniting and forming the Tarascan *Señorio*, ordered his son and nephews, Hiquingaje, Hirípan and Tangaxoan, respectively, to perform auto-sacrifice in a cave (Alcalá, 2013). Lamina 16 (Alcalá, 2013) shows three young men sitting around a fire in a cave with their ears swollen and bleeding after performing auto-sacrifice (Fig. 9). Upon their return from the cave, Tariacuri made them *Señores* and assigned each a part of his estate, creating the three Tarascan capitals, Pátzcuaro, Ihuatzio, and Tzintzuntzan.



Figure 9. Lamina 16 in *La Relación de Michoacán* showing the three young men performing auto-sacrifice inside a cave across Lake Patzcuaro (Alcalá, 2013).

in the center of the body of a Golden Eagle and raised by *Haramé* and *Hireti Thicatame*, two *Uacúsecha* Señores descendants of Tariacuri. The illustration confirms narratives describing how authority was limited to *Uacúsecha* males and shows eagles and caves as symbols of power (Alcalá, 2013, González-Martínez, 2010, Roskamp, 2005, 2010a, 2010b). This is further supported by the contact period Tarascan *Codice de Carapan*, in which the eagle holding up the coat of arms is also depicted wearing a crown (see Fig. 8). Thus, it is not coincidental that the crown over the eagle at Cueva de la Huachizca would be etched at a later time. The artistic similarities between the *Codice de Carapan* and the images found on the basalt within Cueva de la Huachizca suggest that the Tarascan nobles from Itziparátzico carved the rock art panel. Drawing on Sandra Cruz Rivera's (2019) analysis of pre-Hispanic codices, the two thin lines coming out of the man's mouth suggest that the individual is emitting sounds or speech directed at the eagle. Thereby, suggesting that the panel depicts a ritual performed in the Cueva de la Huachizca that involved an act of communication between the man and the eagle (Cruz Rivera, 2019).

CONCLUSIONS

This article presents the results of an archaeological survey conducted by PAPACSUM of previously unpublished Cueva de la Huachizca. This study paid particular attention to the rock art panel that stylistically appears to date to the Postclassic Tarascans. The eagle motif and the cave are shown to be associated with rulership from the earliest Mesoamerican iconography. The crown above the eagle motif appears to be a post-conquest addition that confirms our interpretation. We suggest that the panel within the cave indicates that Cueva de la Huachizca may have been used as one part of rituals of passage in the accession of rulers of the nearby site of Itziparátzico. This would make sense since the cave is one of the longest in the area (Rissolo, 2001).

Our survey has documented a long history of the use of Cueva de la Huachizca with graffiti recording visitation during the late nineteenth and early twentieth centuries. The dates suggest cave utilization during or after the Mexican Revolution. Archaeomagnetic dating of the *resinera* to the twentieth century is significant because the range overlaps with the Cristero Rebellion, confirming the stories described by informants that the cave was a refuge for indigenous communities. Finally, it is important to note that Cueva de la Huachizca is a very important and sacred landscape marker for the community members of Santa Clara del Cobre.

ACKNOWLEDGMENTS

We would like to extend our gratitude to the community members of the *Huatápera* at Santa Clara del Cobre for welcoming us and providing access to the site. Thank you to Dr. Jasinto Robles, Alejandro Valdes-Herrera, and Lissandra Gonzalez-Gonzalez at the Instituto Nacional de Antropología e Historia in Morelia. We also wish to thank geologist Christopher Lloyd and speleologist Luis Rojas for their assistance during the cave survey. Thank you to biologist Jorge Schöndube and geophysicists Avto Gogichaistvili, Veronica Lopez Delgado, and Juan Morales from the National Autonomous University of Mexico (UNAM) of Morelia, Mexico for help with artifact analysis. Special thanks go to James E. Brady, Allan Cobb and several anonymous reviewers for their comments and suggestions which helped strengthen this manuscript. This research in sacred geography and the use of caves in Michoacán was supported by the Archaeological Institute of America and the National Speleological Society's Ralph W. Stone Graduate Fellowship.

REFERENCES

Alcalá, F.J., 2013, *Relación de las ceremonias y ritos y población y gobernación de los indios de la provincia de Michoacán (1539–1541)*, [Relación de Michoacán]: Zamora, Michoacán: Colegio de Michoacán, Gobierno del Estado de Michoacán.

- Brady, J.E., and Prufer, K., eds., 2005, *In the Maw of the Earth Monster: Mesoamerican Ritual Cave Use*: University of Texas Press, Austin. https://doi.org/10.1111/j.1467-9655.2006.00303_1.x
- Campos, C.M., 2018, *Exploring Ancient Tarascan Ritual Cave Use in Central-Southern Michoacán, Mexico*. [Master's thesis]: California State University, Los Angeles.
- Carrasco, P., 1952, *Tarascan Folk Religion: An Analysis of Economic, Social, and Religious Interactions*, Preprinted from Publication 17, Middle American Research Institute: The Tulane University of Louisiana, New Orleans, p. 1–64.
- Castañeda de la Paz, S., and Roskamp, H., eds., 2013, *Los escudos de armas indígenas: de la Colonia al México Independiente*. Instituto de Investigaciones Antropológicas, Universidad Nacional Autónoma de México, Ciudad de México y El Colegio de Michoacán: Zamora, Michoacán.
- Chauvin, A., Garcia, Y., Lanos, P., and Laubenheimer, F., 2000, Paleointensity of the geomagnetic field recovered on archaeomagnetic sites from France: *Physics of the Earth and Planetary Interiors*, v. 120, p. 111–136. [https://doi.org/10.1016/S0031-9201\(00\)00148-5](https://doi.org/10.1016/S0031-9201(00)00148-5)
- Coe, R.S., Grommé, S., and Mankinen, E.A., 1978, Geomagnetic paleointensities from radiocarbon-dated lava flows on Hawaii and the question of the Pacific nondipole low: *Journal of Geophysical Research*, v. 83, no. B4, p. 1740–1756. <https://doi.org/10.1029/JB083iB04p01740>
- Corona-Núñez, J., 1986, *Tres Codices Michoacanos*. Volumen preparado por el Centro de Estudios sobre la Cultura Nicolaita - Editado por la Universidad Michoacana San Nicolas Hidalgo - Morelia, Michoacán, México.
- Cruz Rivera, S., 2019, La imagen del sonido en códices prehispánicos del centro de México: una propuesta metodológica. *Pasado Abierto*, v. 4, no. 9, p. 60–90. <https://fh.mdp.edu.ar/revistas/index.php/pasadoabierto/article/view/3287/3491>
- De la Rea, A., and Escandón P., 1996, *Crónica de la Orden De N. Seráfico P.S. Francisco, Provincia de S. Pedro Y S. Pablo de Mechoacán en la Nueva España (1639)*, Zamora, Michoacán: El Colegio de Michoacán, Gobierno del Estado de Michoacán, México.
- Gómez-Mussenth, L.T., 2010, Análisis contextual para la interpretación de los petrograbados de las islas del Lago de Pátzcuaro. [Master's Thesis]: El Colegio de Michoacán A. C. Centro de Estudios Arqueológicos, Zamora, México.
- González-Martínez, R., 2010, Alianza religiosa y realiza sagrada en el antiguo Michoacán: *Revista Española de Antropología Americana*, v. 41, no. 1, p. 75–96. https://doi.org/10.5209/rev_REAA.2011.v41.n1.4
- Grove, D. C., 1973, Olmec Altars and Myth: *Archaeology*, v. 26, no. 2, p. 128–135.
- Hernández-Quintero, E., Goguitchaichvili, A., García-Ruiz, R., Cervantes-Solano, M., and Nava, G.C., 2018, Más de 100 años ininterrumpidos de registro geomagnético en México: implicaciones en la datación absoluta de algunos edificios históricos: *Arqueología Iberoamericana*, v. 39, p. 36–43. <https://doi.org/10.5281/zenodo.3475444>
- Heyden, D., 1975, Los ritos de paso en las cuevas: *Boletín del Instituto Nacional de Antropología e Historia*, v. 2, no. 19, p. 17–26.
- Heyden, D., 2005, Rites of passage and other ceremonial caves, *in*, Brady, J.E., and Prufer K.M., eds., *In The Maw of the Earth Monster: Mesoamerican Ritual Cave Use*, University of Texas Press, Austin, p. 21–34.
- Lloyd, C. (compiler), 2016, *Geologic formation of Cueva de la Huachizca, Michoacán, México*.
- Maldonado, B. and Rehren, T., 2009, Early copper smelting at Itziparátzico, Mexico: *Journal of Archaeological Science*, v. 36, no. 9, p. 1998–2006. <https://doi.org/10.1016/j.jas.2009.05.019>
- Morales, J., Goguitchaichvili, A., Olay, A., Carvallo, C., and Reyes, B.A., 2015, Archeointensity investigation on pottery vestiges of puertitas de rolón, capacha culture: in search for affinity with other Mesoamerican prehispanic cultures: *Studia Geophysica et Geodaetica*, v. 57, p. 605–626. <https://doi.org/10.1007/s11200-012-0878-z>
- Olmos, A.C., 2010, Los petrograbados de Tzintzuntzan, Michoacán: Un sistema de comunicación gráfica. [Master's tesis]: El Colegio de Michoacán A. C. Centro de Estudios Arqueológicos, Zamora, México.
- Pavón-Carrasco, F.J., Rodríguez-González, J., Osete, M.L., and Torta, J.M., 2011, A Matlab tool for archaeomagnetic dating: *Journal of Archaeological Science*, v. 38, p. 408–419. <https://doi.org/10.1016/j.jas.2010.09.021>
- Pavón-Carrasco, F.J., Osete, M.L., Torta, J.M., and De Santis, A., 2014, A geomagnetic field model for the Holocene based on archaeomagnetic and lava flow data: *Earth Planetary Science Letters*, v. 388C, p. 98–109. <https://doi.org/10.1016/j.epsl.2013.11.046>
- Pollard, H.P., 1993, *Tariacuri's Legacy: The Prehispanic Tarascan State*: University of Oklahoma.
- Pollard, H. P., 2008, A Model of the Emergence of the Tarascan State: *Ancient Mesoamerica*, v. 19, p. 217–230. <https://doi.org/10.1017/S0956536108000369>
- Punzo-Díaz, J.L., 2014, Los Antecedentes Pre-Hispánicos de Santa Clara del Cobre, *in* Santa Clara del Cobre, Zona de Monumentos Históricos: Instituto Nacional de Antropología e Historia, México, México D.F.
- Punzo-Díaz, J.L., Castañón M., and González-González, L., 2015, Proyecto Arqueología y Paisaje del Área Centro-Sur de Michoacán Informe Técnico 2014–2015, Parcial temporada 2015: Archivo técnico del Instituto Nacional de Antropología e Historia, México, México D.F.
- Punzo-Díaz, J.L., 2018, Paisaje y arquitectura en el mundo de los habitantes del Michoacán antiguo, *in* Sánchez-Nava, P., ed., *Un patrimonio universal: las pirámides de México: Cosmovisión, cultura y ciencia*, Instituto Nacional de Antropología e Historia, Gobierno del Estado de México.
- Ramírez, F., 1959, Relación sobre la Resistencia de Michoacán en Pátzcuaro, *in*, Zubillaga, F., ed., *Monumenta Mexicana, 1581–1585*, v. 2, p. 474–538, Rome: n.p. (Original document was written in 1585).
- Rissolo, D.A., 2001, *Ancient Maya Cave Use in the Yalahau Region, Northern Quintana Roo, Mexico*. [Ph.D. thesis]: University of California, Riverside. ProQuest Publishing. <http://search.proquest.com/docview/250788855/>
- Roskamp, H., 2005, La metalurgia prehispánica y colonial en Jicalán, Michoacán, México: una prospección arqueológica, A project report presented to the Foundation for the Advancement of Mesoamerican Studies, Project #02011. <http://www.famsi.org/reports/02011es/02011es-Roskamp01.pdf>
- Roskamp, H., 2010a, Gods of Metals: Tlatlahuqui Tezcatlipoca and the Sacred Symbolism of Metallurgy in Michoacán, West Mexico: *Ancient Mesoamerica*, v. 21, no. 1, p. 69–78. <https://doi.org/10.1017/S0956536110000118>
- Roskamp, H., 2010b, The Nahuas of Tzintzuntzan-Huitzitzilan, Michoacán: History, Myth and Legitimization of a Prehispanic Señorío: *Journal de la Société des Américanistes*, v. 96-1, p. 75–106. <https://doi.org/10.4000/jsa.11264>
- Thellier, E. and Thellier, O., 1959, Sur l'intensité du champ magnétique terrestre dans le passé historique et géologique: *Annals of Géophysics*, v. 15, p. 285–376.
- Townsend, R. F., 1987, Coronation at Tenochtitlan, *in*, Boone, E.H., ed., *The Aztec Templo Mayor*: Dumbarton Oaks Research Library and Collection, Washington, D.C., p. 373–410.
- Van Gennep, A., 1960, *Les Rites de passage (1909)*, Chicago: University of Chicago Press.
- Warren, J.B., 1990, *Vocabulario en lengua de Mechuacán, Facsimile, Fuentes de la Lengua Tarasca óPurépecha*, 2, Morelia: Filmax Publicistas, Morelia, Michoacán, Mexico. (Original document was written in 1559 by Maturino Gilberti.)

GUIDE TO AUTHORS

The *Journal of Cave and Karst Studies* is a multidisciplinary journal devoted to cave and karst research. The *Journal* is seeking original, unpublished manuscripts concerning the scientific study of caves or other karst features. Authors do not need to be members of the National Speleological Society, but preference is given to manuscripts of importance to North American speleology.

LANGUAGES: The *Journal of Cave and Karst Studies* uses American-style English as its standard language and spelling style, with the exception of allowing a second abstract in another language when room allows. In the case of proper names, the *Journal* tries to accommodate other spellings and punctuation styles. In cases where the Editor-in-Chief finds it appropriate to use non-English words outside of proper names (generally where no equivalent English word exist), the *Journal* italicizes them. However, the common abbreviations i.e., e.g., et al., and etc. should appear in roman text. Authors are encouraged to write for our combined professional and amateur readerships

CONTENT: Each paper will contain a title with the authors' names and addresses, an abstract, and the text of the paper, including a summary or conclusions section. Acknowledgments and references follow the text. Manuscripts should be limited to 6,000 words and no more than 10 figures and 5 tables. Larger manuscripts may be considered, but the *Journal* reserves the right to charge processing fees for larger submissions.

ABSTRACTS: An abstract stating the essential points and results must accompany all articles. An abstract is a summary, not a promise of what topics are covered in the paper.

STYLE: The *Journal* consults The Chicago Manual of Style on most general style issues.

REFERENCES: In the text, references to previously published work should be followed by the relevant author's name and date (and page number, when appropriate) in brackets. All cited references are alphabetical at the end of the manuscript with senior author's last name first, followed by date of publication, title, publisher, volume, and page numbers. Geological Society of America format should be used (see http://www.geosociety.org/documents/gsa/pubs/GSA_RefGuide_Examples.pdf). Please do not abbreviate periodical titles. Web references are acceptable when deemed appropriate. The references should follow the style of: Author (or publisher), year, Webpage title: Publisher (if a specific author is available), full URL (e.g., <http://www.usgs.gov/citguide.html>), and the date the website was accessed in brackets. If there are specific authors given, use their name and list the responsible organization as publisher. Because of the ephemeral nature of websites, please provide the specific date. Citations within the text should read: (Author, Year).

SUBMISSION: Manuscripts are to be submitted via the PeerTrack submission system at <http://www.edmgr.com/jcks/>. Instructions are provided at that address. At your first visit, you will be prompted to establish a login and password, after which you will enter information about your manuscript and upload your manuscript, tables, and figure files. Manuscript files can be uploaded as DOC, WPD, RTF, TXT, or LaTeX. Note: LaTeX files should not use any unusual style files; a LaTeX template and BiBTeX file may be obtained from the Editor-in-Chief. Table files can be uploaded as DOC, WPD, RTF, TXT, or LaTeX files and figure files can be uploaded as TIFF, AI, EPS, or CDR files. Extensive supporting data may be placed on the *Journal's* website as supplemental material at the discretion of the Editor-in-Chief. The data that are used within a paper must be made available upon request. Authors may be required to provide supporting data in a fundamental format, such as ASCII for text data or comma-delimited ASCII for tabular data.

DISCUSSIONS: Critical discussions of papers previously published in the *Journal* are welcome. Authors will be given an opportunity to reply. Discussions and replies must be limited to a maximum of 1000 words and discussions will be subject to review before publication. Discussions must be within 6 months after the original article appears.

MEASUREMENTS: All measurements will be in Systeme Internationale (metric) except when quoting historical references. Other units will be allowed where necessary if placed in parentheses and following the SI units.

FIGURES: Figures and lettering must be neat and legible. Figure captions should be on a separate sheet of paper and not within the figure. Figures should be numbered in sequence and referred to in the text by inserting (Fig. x). Most figures will be reduced, hence the lettering should be large. Photographs must be sharp and high contrast. Figures must have a minimum resolution of 300 dpi for acceptance. Please do not submit JPEG images.

TABLES: See <http://caves.org/pub/journal/PDF/Tables.pdf> to get guidelines for table layout.

COPYRIGHT AND AUTHOR'S RESPONSIBILITIES: It is the author's responsibility to clear any copyright or acknowledgement matters concerning text, tables, or figures used. Authors should also ensure adequate attention to sensitive or legal issues such as land owner and land manager concerns or policies and cave location disclosures.

PROCESS: All submitted manuscripts are sent out to at least two experts in the field. Reviewed manuscripts are then returned to the author for consideration of the referees' remarks and revision, where appropriate. Revised manuscripts are returned to the appropriate Associate Editor who then recommends acceptance or rejection. The Editor-in-Chief makes final decisions regarding publication. Upon acceptance, the senior author will be sent one set of PDF proofs for review. Examine the current issue for more information about the format used.

Journal of Cave and Karst Studies

Volume 83 Number 3 September 2021

CONTENTS

- Article** 93
Solute Transport And Solutional Denudation Rate Of Carbonate Karst In The Semi-Arid Zagros Region (Southwestern Iran)
Alireza Sepahvand, Mitja Prelovšek, Ali Akbar Nazari Samani, Robert James Wasson
- Article** 109
Physical and Analytical Modeling of Rhythmic Karst Springs
Xianxuan Xiao and Qiang Zhang
- Article** 120
Genetic And Functional Diversity Of Soil Bacteria And Fungi From Different Microhabitats In A Karst Region In Southern China
Xinru Li, Min Zhou, Yidong Mi, Haiyan Chen, Hailei Su, Yuan Wei, Fuhan Guo, Fanfan Wang
- Article** 133
An Interpretation Of Cueva De La Huachizca, Santa Clara Del Cobre, Michoacán, México
Cynthia Marlene Campos, José Luis Punzo-Díaz, Veronica Lopez Delgado, Avto Goguitchaichvili, and Juan Morales

Visit us at www.caves.org/pub/journal